UNIVERSITÀ DEL PIEMONTE ORIENTALE

UNIVERSITA' DEGLI STUDI DEL

PIEMONTE ORIENTALE

"AMEDEO AVOGADRO"

Dipartimento di Scienze e Innovazione Tecnologica

PhD thesis in chemical sciences (cycle XXVII)

"Microporous Polyaromatic Polymers Designed for Gas Storage Applications"

Candidate : Mina Errahali

Supervisor: Prof. Leonardo Marchese

Co-supervisors : Dr. Lorenzo Tei, Dr. Giorgio Gatti

Coordinator: Prof. Domenico Osella

Summary

Summary

Summary

GENERAL INTRODUCTION

The main subject of the present Ph.D. dissertation is the synthesis and characterization of novel microporous organic polymers and the determination of their gas (H_2, CH_4 and CO_2) storage capacity. Microporous materials (with pores of less than 2 nm in diameter) have recently attracted considerable attention due to the variety of applications in which they can be used, including heterogeneous catalysis, gas purification, gas separation and gas storage. This research work is part of an industrially driven project that aims at the synthesis and characterization of microporous aromatic polymers to be used for H_2 and CH_4 storage and CO_2 capture.

In Chapter 1, the systems mainly suitable for hydrogen, methane and carbon dioxide storage are described along with their textural properties. Gas storage applications mainly require materials with high surface area and high micropore volume. Different classes of materials having these characteristics such as porous carbons, MOFs (Metal Organic Frameworks) and a organic microporous polymers have been widely studied. The latter can be divided in different subclasses (PAFs, CMPs, HCPs and PIMs…etc), which have in common a structure formed by light elements (H, B, C, O and Si) linked by strong covalent bonds. They normally show high thermal and chemical stability, and can be synthesized with a plethora of organic reactions and building blocks, which provide flexibility for the material design to achieve desirable pore properties.

This PhD thesis has been focused on the synthesis and characterization of the porous aromatic framework (PAF) and hyper-crosslinked polymers (HCP), two classes of materials that can be obtained by different synthetic strategies: the Yamamoto homo-coupling reaction used to synthesize PAF materials and the Friedel-Crafts reaction suitable to obtain HCP polymers. These coupling reactions lead to the formation of new C-C bonds starting from precursors with specific functionalities. These materials and their syntheses will be discussed in Chapters 2 and 3.

In particular, in Chapter 2, an optimized synthesis of PAF polymers and their characterization with several physico-chemical techniques are described. The synthetic procedure was further optimized with the aim to reduce the cost of the synthesis. Besides the optimization of the experimental conditions to obtain reproducible high surface area materials with lower costs, particular attention was paid to improve the storage capacity, especially for CO_2 capture, by introducing amine groups in the material.

In Chapter 3, HCP polymers synthesized from different tetrahedral precursors and FDA as crosslinking agent are described. In the first part of the work, we evaluated how different precursor/FDA ratios change the textural porosity of the resulting polymers. Then, using the optimized conditions, we synthesized new HCP materials with different tetrahedral aromatic monomers. As for PAF, post-synthesis treatments were adopted for

improving the textural properties of the materials. The polymer with the highest surface area and microporous volume was further optimized, in terms of porosity and gas storage capacity, using two different methods: (I) thermal treatment under different conditions, and (II) functionalization with different amine groups.
PAF and HCP materials have been extensively characterized using the most common techniques to determine structure (FTIR, SS-NMR), chemical composition (elemental analysis), crystallinity (PXRD), thermal stability (TGA), surface area and pore distribution (N_2 physisorption at 77K).

In Chapter 4, the results of gas uptake on selected synthesized materials, at different temperatures and pressures are considered. High pressure storage (up to 200 bar) of methane and hydrogen was used to evaluate the maximum uptake capacity of PAF-302. Methane and carbon dioxide storage up to 10 bar were measured for some HCP materials, along with their heat of adsorption and CO_2/N_2 selectivity. For all materials CO_2 storage was evaluated using the Zero Length Column (ZLC) method, at 0.1 bar and 35 ºC which are the real conditions of a typical flue gas stream from post-combustion application. This allowed a rapid screening of materials because the analysis time of each sample is short.

List of abbreviations

Abbreviation	Meaning
ANG	Adsorbed Natural Gas
BET	Branauer, Emmet, Teller
CCS	Carbon Capture And Storage
CMP	Conjugated Microporous Polymer
CNG	Compressed Natural Gas
COD	1,5-cyclooctadiene
COF	Covalent -Organic Frameworks
DCE	Dichloroethane
DMF	N,N-Dimethylformamide
DMSO	Dimethyl Sulfoxide
EA	Elemental Analysis
FDA	Formaldehyde Dimethyl Acetal
FTIR	Fourier Transform Infrared Spectroscopy
HCP	Hyper-Crosslinked Polymer
LNG	Liquefied Natural Gas
MOF	Metal–Organic Frameworks
NLDFT	Non Local Density Functional Theory
PAF	Porous Aromatic Framework
PCFF	Polymer Consistent Force Field
PIM	Polymers Of Intrinsic Microporosity
PPN	Porous Polymer Network
PSD	Pore Size Distribution
PXRD	Powder X-Ray Diffraction
QSDFT	Quenched Solid Density Functional Theory
SEM	Scanning Electron Microscopy
SSA	Specific Surface Area
SS-NMR	Solid State Nuclear Magnetic Resonance
TBPM	Tetrakis(4-bromophenyl)methane
TETA	Triethylenetetramine
TGA	Thermal Gravimetric Analysis
THF	Tetrahydrofuran
TPA	Tetraphenyladamantane
TPE	Tetraphenylethene
TPEa	Tetraphenylethane
TPM	tetraphenylmethane
TPS	Tetraphenylsilane
TPT	Tetraphenyltin
ZLC	Zero Length Column

CHAPTER 1

Gas Storage in Porous Materials

1.1 Introduction

In recent years, porous materials have attracted tremendous interest, investments and efforts in scientific research and technological development around the world. They possess unique surface, structural, and bulk properties that make them relevant in various fields such as ion exchange [1, 2], adsorption (for separation) [3, 4], catalysis [5,6], and gas storage [7-10]. In this introduction chapter the main storage systems for hydrogen, methane and carbon dioxide, as well as their porosity and surface area, will be described in relation to the main classes of porous materials that have been proposed for gas storage.

1.2 Gas storage and capture

The growing world population and the increasing standard of living increase the concerns over the sustainability of oil reserves: the supply of economically usable hydrocarbon resources in the world is limited, and the demand for hydrocarbon fuels is increasing. In the current hydrocarbon economy, transportation is fuelled primarily by petroleum. The burning of hydrocarbon fuels has an adverse effect on the environment as it is responsible for the increase in the earth's atmosphere of CO_2 and other pollutants. A number of potential solutions for conservation and remediation of the environment due to CO_2 increment are cutting edge research topics. These include work in CO_2 capture and storage[11], as well as the use of cleaner fuels, such as natural gas (CH_4) [12] or hydrogen (H_2) [13,14].

1.2.1 Hydrogen Storage

Hydrogen is considered a potentially relevant fuel for the automobile industry because it is the most abundant element in the universe, it contains the highest energy density per unit mass, and it burns cleanly, producing only water. Unfortunately, molecular hydrogen that can be used as fuel does not occur naturally in convenient reservoirs. It needs to be produced by steam reforming of hydrocarbons, water electrolysis or by other methods [15,16].

Possible approaches for hydrogen storage include [17]:

- Physical storage of compressed hydrogen gas in high pressure tanks (up to 700 bar);

- Physical storage of cryogenic hydrogen (cooled to -253°C, at pressures of 6-350 bar) in insulated tanks;
- Storage in advanced materials — within the structure or on the surface of certain materials — as well as in chemical compounds that can undergo a chemical reaction to release hydrogen.

Hydrogen has a very high energy content by weight (about three times higher than gasoline), but it has a very low energy content by volume (liquid hydrogen is about four times lower than gasoline).

Currently, hydrogen is stored either in high pressure tanks or in liquid form in cryogenic tanks. These forms of storage are not suitable for widespread commercial application as the energy density of hydrogen even at about 700 bar or in liquid form is only 4.4 and 8.4 MJ/L, respectively, compared to the energy density of gasoline, namely, 31.6 MJ/L. In addition, there are significant energy costs in storing hydrogen in these forms, not to mention associated safety issues [18].

The alternative is the use of solid porous materials for hydrogen storage. The US department of Energy (DOE) has set quite stringent targets for hydrogen storage capacity for mobile applications that are yet to be met: the targets are 5.5 wt.% as gravimetric capacity (1.8 kWh/kg system), and 0.04 kg/L (1.3 kWh/L system) as volumetric capacity to be achieved by 2017. It should be noted that these are system requirements, and not just targets for the storage capacity of the material itself. In addition, the storage should be safe, durable (1500 operational cycle life), and cost-effective. No existing systems has met these conditions, yet [17].

As far as the interaction/adsorption of hydrogen with/on a material is concerned, there are mainly three different approaches [18]:

- Physisorption: hydrogen remains molecular and binds weakly on the surface of the most common porous materials with a binding energy in the meV range. Hence, it desorbs already at very low temperatures. Sorbent materials belonging to this category are carbon-based materials such as nanotubes, fullerenes, graphene, mesoporous silica, metal–organic frameworks (MOFs), covalent - organic frameworks (COFs), and clathrates [19-21].
- Chemisorption: H_2 molecule dissociates into individual atoms, migrates into the material, and binds chemically with a binding energy lying in the 2-4 eV range. As the bonding is strong, the desorption takes place at higher temperatures. Complex hydrides, which are light metal hydrides, are the main class of materials where hydrogen is held in strong covalent bonds [22-23].
- The third form of binding occurs when the bond between H atoms in a H_2 molecule is weakened but not broken. The strength of interaction is intermediate between physisorption and chemisorption

(binding energy in the 0.1-0.8 eV range). This type of adsorption concerns carbon-based nanostructured materials such as nanotubes, fullerenes and graphenes doped with metals and transition metals [24-26].

Figure 1 summarizes the different types of materials being studied for hydrogen storage along with the challenges that they have to face [18].

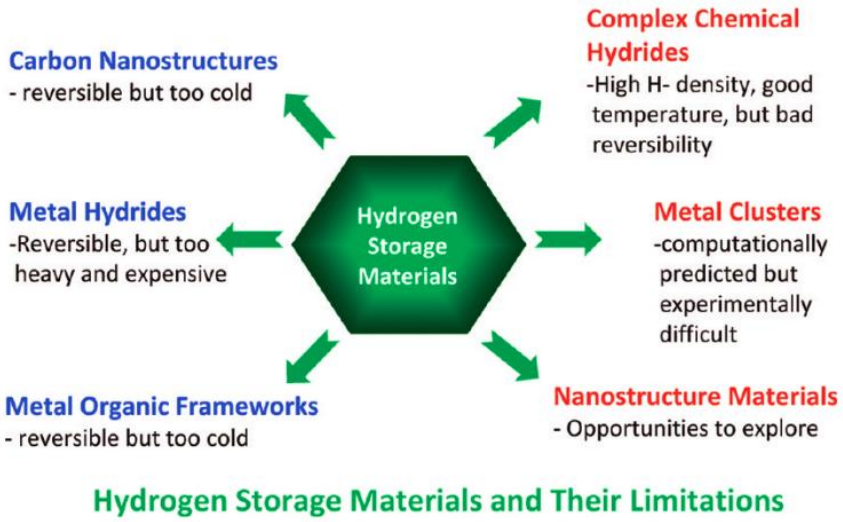

Figure 1. Summary of various hydrogen storage materials and their limitations (Figure adapted from ref. 18)

Metal hydrides are reversible under ambient conditions but are too heavy. Simple chemical hydrides are reversible but only at very high pressure and temperature. Complex chemical hydrides have high hydrogen density but suffer from poor reversibility. Nanostructured materials are very promising but are yet to emerge as practical materials. In fact they offer good reversibility but require very low temperatures of storage. The kinetic of hydrogen adsorption by microporous materials is very rapid, which is a practical advantage for hydrogen storage, but low temperatures are required to achieve significant capacities at useful storage pressures. In practice, low temperature storage requires cooling, which inevitably makes heavier the storage unit and is therefore a significant disadvantage. In order to achieve high volumetric capacities, adsorbed hydrogen must be stored at relatively high densities within the pores.

For these reasons, the hydrogen adsorption capacity of microporous materials at ambient temperature is currently too low for practical use [27]. The actual research in this field is to enhance the interaction of hydrogen with the materials to reach an adsorption capacity sufficiently high for real applications.

1.2.2 Methane Storage

Economical and environmental considerations have also boosted interest in Natural gas (NG) as a fuel for transportation, and especially as a replacement for petrol (gasoline).

In the generation of energy from methane, the major concern is the production of CO_2, though it is comparatively less than other fossil fuels (gasoline or diesel). Indeed, methane has a gravimetric heat of combustion (55.7 MJ kg^{-1}) comparable to that of gasoline (46.4 MJ kg^{-1}), but it boasts the smallest amount of CO_2 per unit of heat produced among fossil fuels, and it is naturally abundant. However, the lack of efficient storage methods has so far prevented the widespread use of NG in motor vehicles.

The two common methods of NG storage currently used are (1) liquefaction at low temperature (down to 120 K) and (2) compression to 200–300 bar at room temperature.

The volumetric energy density of Liquefied Natural Gas (LNG) is lower (22.2 MJ L^{-1}, 112 K) than that of gasoline (34.2 MJ L^{-1}) but requires the storage in expensive cryogenic vessels and it suffers from boil-off losses. On the other hand, Compressed Natural Gas (CNG) necessitates the use of heavy, thick-walled cylindrical storage tanks and multi-stage compressors to achieve a reasonable volumetric energy density, which is actually only 27% (9.2 MJ L^{-1}) with respect to gasoline [28]. Despite efforts to improve cylinders and compressors, the amount of NG stored in a CNG tank permits for only a short driving autonomy on light-duty passenger vehicles, and high pressure storage on vehicles has been associated to safety concerns [29].

In order to take advantage of the benefits that the use of NG in vehicles may offer, attractive alternatives to CNG and LNG are needed. It has been suggested that porous adsorbents represent a safer, simpler, and potentially more cost-effective method for storing NG at ambient temperature and reasonable pressures (around 35 bar) in the form of adsorbed NG (ANG) [30].

Similarly to hydrogen storage, also for CH_4 the adsorption can be physical (weak van der Waals forces) or chemical (significant covalent interactions) depending on the type and on the strength of the interaction between methane molecules and the material surface sites. From an application standpoint, the primary difference between physisorption and chemisorption is the significant disparity in binding energies. For reversible gas storage and delivery, moderate binding energies (measured as heat of adsorption) are required to maximize energy efficiency of the system. Therefore, physisorptive materials are best suited for this application, as chemisorptive materials would require a substantial amount of external heat to release the adsorbed gas.

To address the need for better technologies, in 1993, the U.S. Department of Energy (DOE) set the methane storage target as 150 cm^3 (STP)/ cm^3 at 298 K and 35 bar [31]. In 2000, this target was updated to 180 cm^3 (STP)/ cm^3 [32]. As a result of efforts by a number of researchers, some MOFs exhibited considerably high methane uptakes, which exceeded the above DOE target [33].

In 2012, the U.S. DOE initiated a "Methane Opportunities for Vehicular Energy (MOVE) Program", and re-set several targets to guide the research on adsorbent-based methane storage [34]. The major target is that the adsorbent-level volumetric energy density should exceed 12.5 MJ L^{-1} and 9.2 MJ L^{-1} after packing losses (25%), at room temperature and low pressure (less than 35 bar). This corresponds to a volumetric storage capacity of 0.25 g cm^{-3} or 350 cm^3 (STP)/ cm^3 for the adsorbent material. Even assuming no packing loss, the volumetric storage capacity still needs to be higher than 260 cm^3 (STP)/ cm^3 [35]. Clearly, this is an ambitious target, which none of the currently known adsorbent materials meet. In fact, even for the previously widely-referred, much lower target of 180 cm^3 (STP)/ cm^3, there are only few materials known to reach this value [33, 36, 37]. Additionally, DOE set a target concerning the gravimetric energy density, 0.5 g (methane) g^{-1} (adsorbent), or 700 cm^3 (STP) g^{-1}, which is equally challenging.

The ideal sorbent should also show resistance to impurities typically encountered in natural gas sources with a lifetime of at least 100 fill–release cycles, and it should be cost effective approaching, $10/kg sorbent, in addition to other system level targets such as desorption rates, tank abuse tests,…etc [29].

1.2.3 Carbon Dioxide Capture and Storage (CCS)

Beside the development of technologies for the use of methane [38] and hydrogen [39] as clean fuels, industrial technologies for carbon dioxide capture are vital in environmental safety. Due to growing levels of greenhouse gas emissions (Figure 2), separation of CO_2 from mixtures of gases such as the gas emitted from the combustion of fossil fuels is of great importance [40].

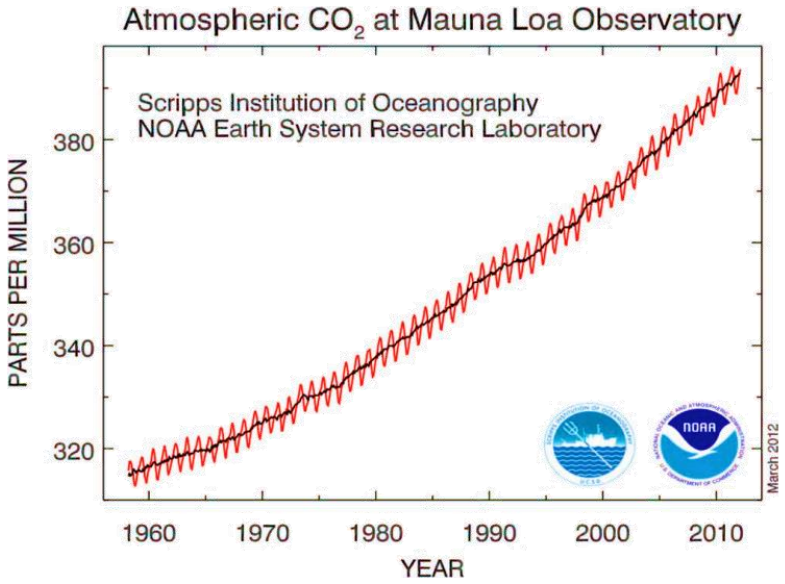

Figure 2. The increment of CO_2 concentration during the period 1958–2010 (at Mauna Loa Observatory), in the atmosphere. (Figure adapted from ref. 41)

Carbon capture and storage (CCS) is an efficient way to reduce CO_2 concentration in the atmosphere. It is a three-step process including separation of CO_2 from other gases before reaching the atmosphere, CO_2 transportation, and its permanent storage [41]. Among them, the CO_2 capture is the most challenging key step for which new adsorbent materials need to be developed. Conventional adsorbent materials rely on either chemisorption or physisorption to capture CO_2.

There are three major approaches for CCS: pre-combustion capture, oxy-fuel process and post-combustion capture [42]:

- In pre-combustion, the fossil fuel is partially oxidized in a gasifier. The resulting syngas (CO and H_2) is shifted into H_2 and CO_2, which can be captured from the stream.
- Oxy-combustion occurs when the fuel is burned in the presence of oxygen. The resulting flow gas consists mainly of pure CO_2 which can be transported to the sequestration site and stored.
- The post combustion capture is based on removing CO_2 from the flow gas after combustion. Instead of being released directly into the atmosphere, flue gas is passed through a particular equipment that separates/captures most of the CO_2.

Post-combustion capture offers some advantages since existing combustion technologies can still be employed without radical changes. This makes post-combustion capture easier to implement as a retrofit option compared to the other two approaches.

Various technologies such as membrane separation, cryogenic distillation and adsorption can be used for CO_2 capture. The adsorption is the ideal way to achieve efficient CCS. It is a separation technology, able to reduce both cost and energy of post-combustion capture compared to other technologies. Selective capture and subsequent storage of carbon dioxide in porous materials has been considered as a promising new approach [11].

The adsorbents used for CO_2 capture can be placed into two categories: physical and chemical adsorbents [43].

- Chemisorption is a sub-class of adsorption, driven by a chemical reaction occurring at the exposed surface. Chemical adsorbents are mostly metal compounds such as metal oxides and metal salts.
- Physisorption is a process in which the electronic structure of the atom or molecule is barely perturbed upon adsorption. The major physical adsorbents reported for CO_2 adsorption include activated carbons and inorganic porous materials such as zeolites.

However, the success of this approach is dependent on the development of adsorbents with high capacity and selectivity; Ideally, this has to be environmentally benign, renewable, safe, and cost-effective [41].
In summary, the goal remains in the development of low-cost and high-performance adsorbents for CO_2 sequestration, gas separation and energy storage applications.

1.3 Porosity and Surface area

Porous materials are most frequently characterized in terms of pore sizes derived from gas sorption data, and IUPAC (International Union of Pure and Applied Chemistry) conventions have been proposed for classifying pore sizes and gas sorption isotherms that reflect the relationship between porosity and sorption.

1.3.1 Adsorption isotherms

The adsorption of guest molecules onto a solid surface plays an essential role in determining the properties of porous compounds. Depending upon the strength of the interaction, all adsorption processes can be divided into chemical and physical adsorption categories. Chemical adsorption or chemisorption involves valence forces of the same type as those operating in the formation of chemical compounds, whereas physical adsorption or physisorption is a general phenomenon which occurs whenever a gas (the adsorbate) is brought into contact with the surface of a solid (the adsorbent), in this case the forces involved are intermolecular

forces (van der Waals) and always include the long-range London dispersion forces and the short-range intermolecular repulsion [44].

Adsorption is described through isotherms, which correlate the amount of gas adsorbed to the pressure in the system at a constant temperature. The adsorbed gas quantity is always normalized to the mass of adsorbent to allow the comparison with other materials.

The textural analysis of powders is usually performed by physisorption of nitrogen, argon and krypton at cryogenic temperatures (77.4 K and 87.3 K). From a proper isotherm, it is possible to extract information about surface area, pore size and porosity of a given material.

IUPAC proposed to classify pores by their internal pore width:

- Pores exceeding ~50 nm widths are called macropores;
- Pores between 2 and 50 nm widths are called mesopores;
- Pores not exceeding ~ 2 nm widths are called micropores, which are further divided into those < 0.7 nm (ultramicropores) and those in the 0.7 – 2 nm range (supermicropores).

The sorption behaviour in mesopores is distinct from the adsorption phenomena occurring in micropores. The mesopore adsorption is dominated by capillary condensation, which is responsible for a sharp adsorption enhancement around the mid relative-pressure region. Conversely the adsorption in a micropore should not be considered as that of molecules onto a solid surface but as the filling of molecules into a nanospace where a deep potential field is generated between the adsorbate molecules and the pore walls. In this case, the adsorption isotherm shows a steep rise at very low relative pressure and a plateau after saturation [45].

Based on IUPAC classification, there are six representative adsorption isotherms that reflect the relationship between porous structure and type of sorption (Figure 3a) [46].

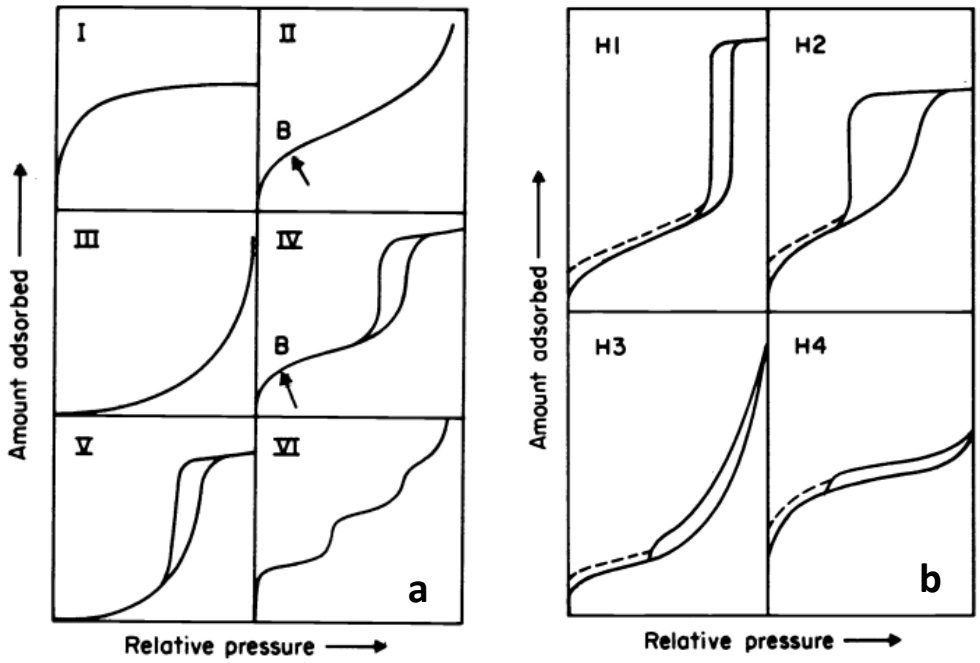

Figure 3. (a) Types of physisorption isotherms; (b) Types of hysteresis loops

These adsorption isotherms are characteristics of microporous (Type I), nonporous and macroporous (types II, III and VI), and mesoporous (type IV and V) adsorbents.

An empirical classification of hysteresis loops was given by IUPAC (Figure 3b), in which the shape of the hysteresis loops (types H1 – H4) is correlated to the adsorbent texture. According to this classification [46, 47]:

- Type H1 is often associated with porous materials exhibiting a narrow distribution of relatively uniform (cylindrical-like) pores.
- Materials that give rise to H2 hysteresis contain a more complex pore structure in which network effects such as pore blocking percolation and cavitation are relevant (Figure 4) [48-50]. In case of pore blocking (sometimes called ink-bottle) desorption from the pore body may occur only after emptying its neck. In other words, desorption from the neck triggers evaporation in the blocked pore. Thus, the vapour pressure of desorption from the pore body depends on neck size, network connectivity, and on the state of the neighbouring pores. While the mechanism of desorption involves cavitation phenomena (spontaneous nucleation and growth of gas bubbles in the metastable condensed fluid) when the neck diameter is smaller than a certain critical width (estimated to be ca. 6 nm for nitrogen at 77.4 K). In this case, the pore body empties while the pore neck remains filled.

- Isotherms with type H3 hysteresis do not exhibit any limiting adsorption at high P/P_0. This behaviour can be caused by the existence of non-rigid aggregates and in principle should not be expected to provide a reliable assessment of either the pore size distribution or the total pore volume.
- H4 hysteresis loops are generally observed with complex materials containing both micropores and mesopores.

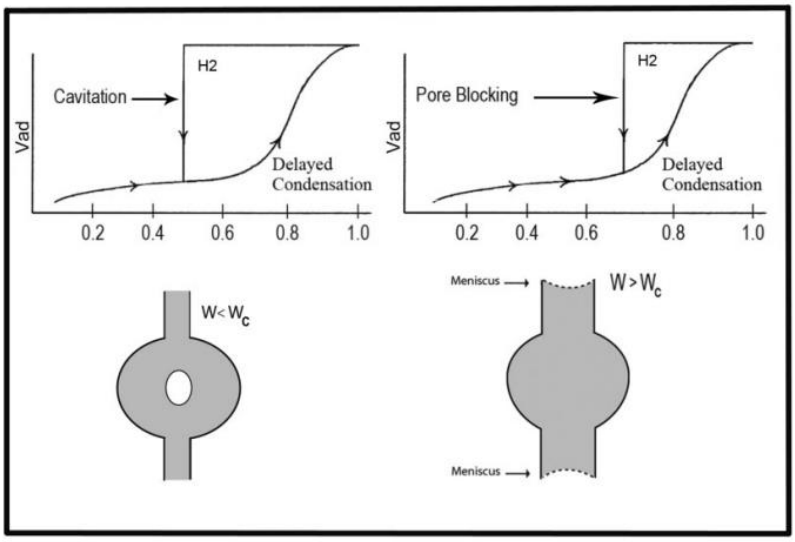

Figure 4. Schematic illustration of pore blocking and cavitation controlled evaporation. Adapted from ref. 46.

Great progress was achieved in the understanding of adsorption, capillary condensation, and desorption phenomena in highly ordered mesoporous materials with simple pore geometries, such as MCM and SBA-type mesoporous silica crystals [51]. However, there are still many open questions concerning adsorption - desorption mechanisms in more complex porous systems. Fluids adsorbed in hierarchically structured micro-mesoporous materials exhibit a great variety of hysteretic adsorption-desorption isotherms with multiple steps related to phase transformations in adsorbed phases. Adsorption -desorption processes involve a combination of physical mechanisms, such as delayed condensation, advanced condensation, cavitation-induced evaporation, pore blocking, and percolation, which are reflected in characteristic types of hysteresis loops formed by adsorption and desorption isotherms [52].

The hysteresis loops causes a considerable complication for the pore structure characterization; however, if interpreted correctly, hysteresis loops can provide important information on pore network morphology, which is crucial for discriminating the physical mechanisms of phase transformation [53].

1.3.2 Surface area measurements and pore size distribution

The specific surface area (SSA) is a relevant textural parameter of adsorbent materials. Conventionally, the Brunauer-Emmett-Teller (BET) gas adsorption method has become the most widely used standard procedure for the determination of the SSA, in spite of the over simplification of the theoretical model on which is based [44].

In particular, the BET model applied to the N_2 adsorption data at 77 K has been widely used to characterize the adsorbent material of interest. It assumes that once a monolayer becomes saturated, a further monolayer can form on top, and that the rates of adsorption and desorption are equal for each layer.

It is usual to apply the BET equation in the form:

$$V = \frac{V_m c P}{P_0 - P\left[1 + \frac{(c-1)P}{P_0}\right]}$$

Where: P = adsorption pressure, P_0 = saturation vapour pressure, c = the BET constant, V = volume of adsorbed gas, V_m = monolayer volume.

This can be rearranged to:

$$\frac{P}{V(P_0 - P)} = \frac{c-1}{cV_m}\left(\frac{P}{P_0}\right) + \frac{1}{cV_m}$$

Where $P/V(P_0-P)$ linearly correlates with P/P_0, and the values of V_m and c can be obtained from the slope $[(c-1)/V_m c]$ and intercept $[1/(V_m c)]$ of the straight line. Knowing the monolayer volume and the area occupied by one adsorbate molecule, the BET surface area (S) can be derived:

$$S = N_A V_m \sigma$$

Where: S = BET surface area, N_A = Avogadro's number, V_m = monolayer volume and σ = area occupied by one adsorbate molecule.

The range of linearity is restricted to a limited part of the isotherm — usually the 0.05—0.30 P/P_0 range. Therefore, the SSA of any material can be measured by knowing the amount of sample, the amount of gas adsorbed in the monolayer and the area occupied by a single adsorbed molecule. Nitrogen (area of 16.2 $Å^2$) is

the most commonly used gas for BET measurements: this method allows the calculation of SSA ranging from 0.01 to 6000 m^2/g.

For materials with a wide range of pore sizes including ultramicropores (pores smaller than 7 Å), the diffusion of nitrogen at 77K is very slow. This leads to time-consuming measurements of adsorption isotherms determined in non-equilibrium conditions. In order to overcome this inconvenience, Argon adsorption at its boiling temperature (87.3 K) has been proposed as an alternative gas for a more reliable determination of the textural properties (pore size and surface area analyses) of microporous solids [45]. While nitrogen is a diatomic molecule with a quadrupole moment which produces specific interactions at the gas–solid interface, argon is much less interacting: for example, argon has no dipole or quadrupole moment, allowing to provide a more accurate scenario of the porous structure for a given solid. Compared to nitrogen, argon adsorption reveals a much more straightforward correlation between the pressure where micropore filling occurs and the pore size. This assumption, together with the higher boiling temperature (87.3 K), shifts argon pore filling to higher relative pressures (as compared to nitrogen at 77.4 K), which helps to reduce some kinetic restrictions usually associated with nitrogen adsorption at 77.4 K.

Pore size distribution can also be calculated from the isotherm using specifically developed models based on size and shape. Several different approaches are used to characterize the pore size distributions. In order to achieve a more realistic description, microscopic theories describing the sorption and the behaviour of fluids in narrow pores on a molecular level are necessary. Since the development of the PSD (pore size distribution) calculation methods, the Non Local Density Functional Theory (NLDFT) method, has been widely used for the characterization of micro- and mesoporous materials [54].

Briefly, the evaluation of PSD is based on the theoretical isotherms calculated for individual pores of a given adsorbate–adsorbent system. These isotherms, which constitute the so-called kernel, are generated using the NLDFT method where the fundamental molecular parameters characterizing the gas–gas and gas–solid interactions of the adsorption system are employed. The mathematical procedure used to calculate PSD can be described as the fitting between theoretical and experimental isotherms: the obtained PSD represents volumetric contributions of pores with different sizes whose theoretical isotherms best fit the experimental data [55].

1.4 Adsorbent properties for best performance gas storage

The work of this thesis primarily concern with the study of physical adsorption in different porous materials. Each gas and its associated applications have criteria that should be met for any gas storage material to be of use in practice. In general, there are different sets of performance criteria for a good adsorbent as listed below [56]:

- High adsorption capacity. One of the most important parameters is the high specific surface area (SSA). However, simple considerations based on SSA are not enough to obtain an efficient material: also the sizes of the pores are of considerable importance, as adsorption predominantly occurs within the pores that are able to create a sufficiently high attractive potential. Such a situation is met as soon as the pore walls are so close to each other that their own potential fields overlap. This affects the bonding strength of the molecules to the adsorbent surface, which is related to the isosteric heat of adsorption [57].
- Thus, the most relevant properties that affect the gas adsorption capacity are SSA, surface chemical nature, and pore size. These parameters determine how much adsorbates can be accumulated per unit mass of adsorbents.
- High selectivity. For multicomponent mixtures, selectivity is highly desirable for gas separation. The selectivity of an adsorbent will depend on pore size, shape and pore size distribution as well as on the nature of the adsorbate components.
- Favorable adsorption kinetics. Adsorption kinetics is determined by the particle (crystallite) size, and by the macro-, meso and microporosity of the adsorbent. Sometimes, binder type and amount would also affect the interparticle transport and thus the global adsorption process kinetics. For a favourable kinetic, the adsorption rate should be high or controllable depending on the requirements of a particular application.
- Excellent mechanical properties. Adsorbents need to be mechanically strong and robust enough to stand attrition, erosion and crushing in adsorption columns or vessels. High bulk density and crushing strength, and attrition resistance are desirable.
- Good stability and durability in use. Adsorbents are often subject to harsh chemical environments or to high pressure and thermal conditions. A high stability in those environments/conditions is essential in ensuring long life or durable utilization.

Obviously, the practical challenges concern the preparation of high performance materials in a simple and cost effective manner and the materials should meet the above requirements/criteria as much as possible.

1.5 Porous materials for gas storage

In recent years, nanoporous materials have been a core focus of scientific and technological importance because of their ability to adsorb within their extended interior surface and pore space atoms, ions and molecules. The main classes of materials that show good performances for gas storage are [28, 58-62]:

1) Porous inorganic materials (e.g. zeolites)
2) Porous Carbons
3) Metal Organic Framework materials (MOFs, also known as Porous Coordination Polymers (PPCs))
4) Microporous organic polymers (PIMs, COFs, CMPs, HCPs, PAFs... etc)

1.5.1 Porous inorganic materials: zeolites

Zeolites are a family of microporous aluminosilicates formed from AlO_4 and SiO_4 tetrahedra. They are crystalline materials with well-defined structures and amongst the most widespread chemical materials used today. Their ordered crystalline nature gives them uniform cavities and channels with dimensions in the microporous regime (Figure 5). The framework structures are relatively rigid and, as with all microporous solids, they have high SSA and large pore volumes.

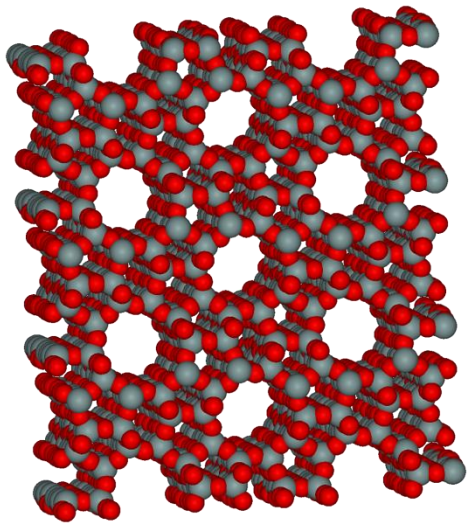

Figure 5. The microporous structure of a zeolite ZSM-5

Several types of zeolites are industrially produced and are widely used in different applications, which include purification of gases and liquids by removal of impurities [63, 64], catalysis in petrochemical industries [65], molecular sieves [66], gas sensors [67] and gas separation membranes [68].

Zeolites have a number of significant practical advantages over other microporous adsorbents in that, for example, they possess high thermal stability. However, it seems unlikely that zeolites could be useful as practical gas storage media as discussed by Felderhoff et al. [69]. The problems encountered when using zeolites as adsorbents for the storage of gas are the following [70]:

i) The presence of non-structural porosity given by aggregations of zeolite particles, which diminish the amount of material in the same volume and thus worsen the gas storage.

ii) Zeolites with hydrophilic character may preferentially adsorb traces of water found in gas mixtures, with a consequent reduction in storage capacity.

iii) Relatively low surface areas (<1000 m^2/g).

1.5.2 Microporous carbons

Several types of porous carbons such as activated carbons, carbon nanotubes and nanofibres and microporous templated carbons have attracted interest for gas storage [71]. From a practical point of view, porous carbons are already commercially produced in large quantities for a broad range of applications and are relatively inexpensive.

Among porous carbons, activated carbons are the most widely studied family. They are a family of synthetically modified carbon-based materials containing very small graphite crystallites and amorphous carbon (Figure 6). These materials generally are prepared from a carbonaceous starting materials (coal, wood, coconut husks …. etc) by a thermal treatment or chemical treatment, which can lead to polymeric systems with large surface areas, often well in excess of 1000 m^2g^{-1} and even up to >3000 m^2g^{-1} [72].

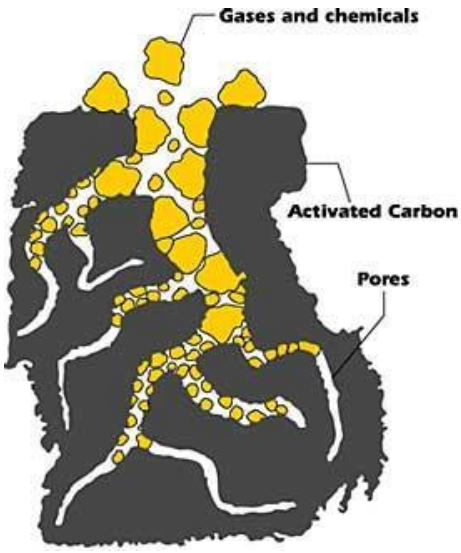

Figure 6. Representation of the pore structure of activated carbons

Carbon dioxide adsorption capabilities for activated carbons are typically 2-3 mmol/g at 25 °C and 1 atmosphere pressure, but recently an activated carbon prepared from sawdust, AC-2-600, showed an enhanced carbon dioxide adsorption capacity of 4.8 mmol/g under the same conditions [73, 74].

As for methane, one of the best activated carbons reported in the literature, Maxsorb® carbon (Kansai coke based) [75] with a surface area of 3100 $m^2 g^{-1}$, is characterized by a storage capacity of 211 mg g^{-1} at 298 K and 35 bar.

Unfortunately, due to their method of production, most activated carbons have a wide distribution of pores sizes ranging from microporous to macroporous. Additionally, the surface of activated carbons is chemically well defined with a mixture of oxygen and nitrogen functional groups. These two factors combine to give an excellent adsorbent material for a wide range of species, though it suffers from poor selectivity for specific molecules. Moreover, improvement of the storage capacity for porous carbons is currently limited by the difficulties in increasing the surface area above 3500 $m^2 g^{-1}$, being this parameter strongly correlated with the amount of gas that can be stored in the material.

1.5.3 Metal−Organic Frameworks (MOFs)

In recent years, a new family of materials, porous metal−organic frameworks (MOFs) or coordination polymers in a broader sense, have emerged as promising adsorbents for gas storage.

MOFs consist of metal ions or clusters coordinated to organic linkers (Figure 7) to form three-dimensional framework structures like “crystal sponges”. The large combination of metals joints and organic linkers, the large surface areas, and tunable pore sizes make MOF compounds highly attractive for storing gas [76-78].

The intense interest in these inorganic-organic hybrid solids [76] has resulted in a vast array of new compounds proposed in the recent literature for the hydrogen, methane or carbon dioxide storage [79, 11, 35].

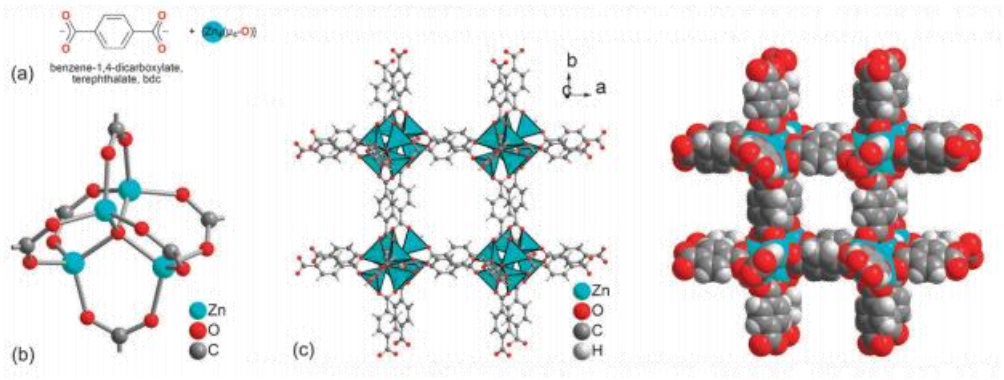

Figure 7. (a) Building blocks for MOF-5 (IRMOF-1), 3D-[Zn_4O $(bdc)_3$], (b) ball-and-stick representation of the tetrahedral {Zn_4O} secondary building unit with the carboxylate groups which span the edges of the {Zn_4O} tetrahedron in an octahedral fashion and (c) the crystal structure packing diagram as ball-and-stick, with polyhedral {Zn_4O}, and as space-filling representation. Adapted from ref. 80.

The most interesting feature of these materials is that they can be highly porous with internal surface areas that can reach the record value of 10 400 m^2 g^{-1} for MOF-210 [81]. For comparison this value is significantly higher than zeolites, which typically have surface areas of several hundred m^2g^{-1}. Additionally, this class of porous materials has unique features, such as structural flexibility and exposed metal sites, which give them more potential for future development.

The highest gravimetric adsorptions of CO_2 have been reported in frameworks with high surface areas and pore diameters lower than 15 Å. The framework [Zn4O$(btb)_2$] (MOF-177) with a surface area of 4500 m^2g^{-1}, for instance, exhibits the highest capacity for CO_2, taking up to 33.5 mmol g^{-1} at 32 bar [82].

MOFs with coordinatively unsaturated metal centres, such as PCN-14 [33], HKUST-1 [83] and MOF-74 [84], have been considered as the most promising MOFs for methane storage, with storage capacity that exceed 180 cm^3(STP)/ cm^3.

MOFs exhibiting particularly high hydrogen storage capacities include MOF-210 [81] and NU-100 [85]. These two materials have reported gravimetric hydrogen adsorption capacities of 176 mg g^{-1} and 164 mg g^{-1}, respectively.

However, these materials are generally less robust than zeolites and microporous carbons, because they exhibit lower thermal and chemical stability that hinder them from usage under extreme conditions.

Nevertheless, their commercialization is already under way, principally by BASF who market a series of framework materials under the trade name Basolite TM, and so the practical application and use of these materials on an industrial scale is clearly feasible.

1.5.4 Microporous organic polymers

Porous Organic Polymers is another class of microporous materials of great interest in literature. They can be divided in several subclasses of polymers, which have in common the following features [86]:

- The structure is formed by light elements (H, B, C, O and Si) that are linked by strong covalent bonds (B–O, C–O, C–C, B–C, and Si–C).
- A high thermal and chemical stability to air and atmospheric moisture since they are linked by strong covalent bonds.
- Normally, they do not have a long range order. Thus, their structure is amorphous due to irreversible bond formation governed by a kinetic control.
- They can be constructed using a plethora of organic reactions and building blocks, which provides flexibility for the material design to achieve desirable pore properties. In all the materials is possible to use a wide range of organic functionalities using different synthetic strategies and a great choice of monomers that makes it easy to introduce various functional groups in the pore walls [87].
- They show high specific surface area and microporosity, two properties of fundamental importance in gas storage. Actually, they are the reference point for the evaluation of the capacity of an adsorbent material.

The main classes of microporous organic polymer that are considered as potential candidates for gas storage are: Polymers of Intrinsic Microporosity (PIMs), Covalent Organic Frameworks (COFs), conjugated Microporous Polymers (CMPs), Hypercrosslinked Polymers (HCPs) and Porous Aromatic Frameworks (PAFs) [88].

1.5.4.1 Polymers of intrinsic microporosity (PIMs)

Polymers of intrinsic microporosity (PIMs) are a group of polymeric materials which do not require a network of covalent bonds in order to show microporosity; indeed intrinsic microporosity in polymers is defined as "a continuous network of interconnected intermolecular voids, which are formed as a direct consequence of the shape and rigidity of the component macromolecules" [89, 3].

PIMs are amorphous solids due to their random packing and lack of long-range order, but possess surface areas in the range of 400 – 1760 m^2/g [3, 90]. Usually they are formed by a double nucleophilic aromatic substitution reaction between a tetrahydroxylated monomer and a tetrafluorinated monomer, resulting in the formation of dioxane links between monomer units (Figure 8). It is essential for the production of a microporous PIM that one of the monomers has a highly rigid and contort structure.

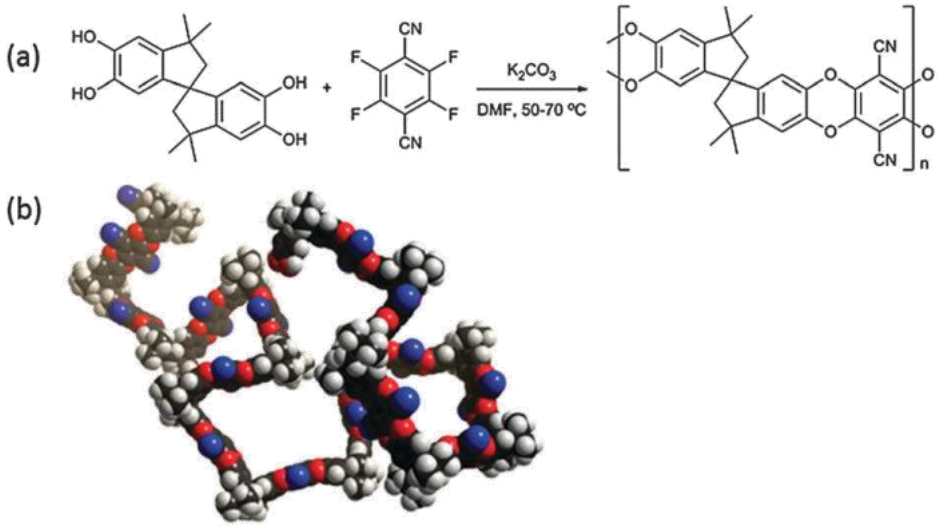

Figure 8. Typical synthesis of PIM polymer (a) and molecular model(b). Adapted from ref. 3

Hydrogen uptakes of up to 2.7 wt%, at 10 bar and 77 K, have been reported for a triptycene-based polymer (trip-PIM) [91].

1.5.4.2 Covalent organic frameworks (COFs)

Covalent organic frameworks (COFs) are a family of porous crystalline macromolecules made solely from light elements (C, H, N, B and O) organic building blocks, which are linked together by strong covalent bonds [92, 93].

COFs possess rigid structures, long-range order, high thermal stability (up to 600 °C) and permanent porosity with extremely high surface areas, up to 6450 m^2/g [94].

The synthetic routes for COFs may be different, and the most used are the self-condensation of aromatic boronic acids and the co-condensation between boronic acids and aromatic diols in which the covalent bonds are boronic esters (Figure 9); these synthetic routes are very economic since a simple dehydration process without the use of catalysts or other reagents are necessary.

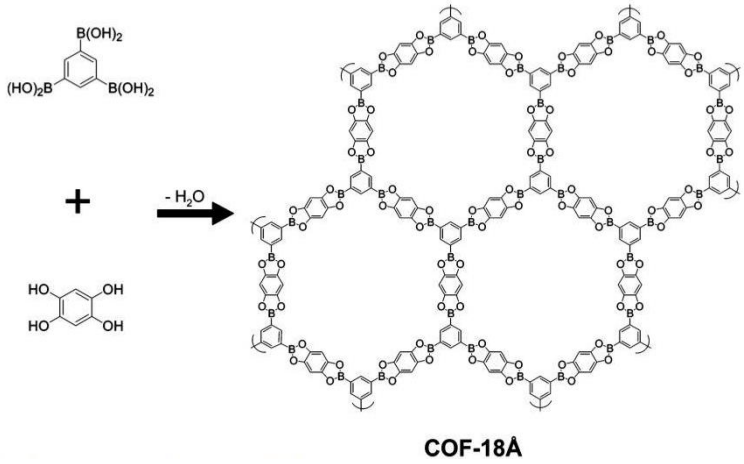

Figure 9. The building blocks and structure model for COF-18 Å [95].

Each connector/linker combination forms a specific 2D or 3D framework with topology based on the geometry and the type of reactive functional groups [96]. COFs are attractive materials because their organic nature allows total control over their structural parameters, including composition and porosity. Thus, they are ideal for gas storage applications. The storage capabilities of COFs for gases, such as hydrogen, methane, and carbon dioxide, have been widely investigated [7, 97, 98].

As for methane, the highest COF storage capacity was observed for COF-102, which had a value of 187 mg g^{-1}. COF-103 also demonstrated a high capacity of 175 mg g^{-1}. These values are comparable to values observed for MOFs (MOF-210; 220 mg g^{-1}) [81].

On the other hand, the largest hydrogen storage capacity is observed for 3D COF-102 (S_{BET}: 3620 m^2 g^{-1}) [7], which uptakes 72 mg per gram at 1 bar and 77 K. This capacity is comparable to those of MOF-177 (75 mg g^{-1}, S_{BET}: 4500 m^2 g^{-1}) and MOF-5 (76 mg g^{-1}, S_{BET}: 3800 m^2 g^{-1}).

As far as CO2 storage is concerned, Yaghi and co-workers have reported that the CO_2 uptake of COF-102 reaches 27 mmol g^{-1} at 298 K and 35 bar [7].
However, COFs suffer from poor gas selectivities, as the large pore size does not usually provide a preferential site of adsorption for one gas over another and, among the microporous organic polymers they tend not to be particularly stable to moist air, which is obviously a problem and limits their potential as useful materials [99].

1.5.4.3 Conjugated microporous polymers (CMPs)

Conjugated microporous polymers (CMPs) are a class of porous materials with amorphous three-dimensional organic framework made up of multiple carbon–carbon bonds and/or aromatic rings that form an extended conjugated network. CMPs were first reported in 2007 [100] and took advantage of Sonogashira–Hagihara palladium coupling to link aromatic halides to aromatic alkynes, thus forming poly(aryleneethynylene) (PAE) networks, with BET surface areas that exceed 1000 m^2/g in some cases [101, 102].
CMPs are formed under kinetic control and display no long-range order, but their pore sizes are well-defined and can be controlled by careful selection of the monomers [101]. Surface areas can also be controlled by changing the linker length, with the number of micropores decreasing with increasing linker length. This behavior can be explained by the extra flexibility granted to the framework by longer linkers, that allows a more efficient packing and decreases the available surface area.

Thanks to the study on PAEs it was discovered that: (i) similarly to the crystalline materials, such as MOFs and COF_S, the surface area and pore distribution can be modulated according to the type of organic linker that connects the monomers, and (ii) that the structural order is not a prerequisite for controlling of microporosity.

The gas sorption capacity of conjugated porous materials is effectively comparable with classical porous materials such as zeolites and active carbons. H_2 storage capacity of CMPs based on poly(aryleneethynylene) was studied by Cooper and coworkers who reported that the CMP with the largest BET surface area (1018 m^2 g^{-1}) shows a H_2 storage capacity of 1.4 wt% [103].

Ren et.al. reported CO_2 capture by CMP polymers [104]: The most successful of these materials is TNCMP-2, a polymer made from 2,4,6-triphenyl-1,3,5-triazine and tris(4- ethynylphenyl)amine. This polymer, with a high

surface area of 995 m^2/g, shows excellent CO_2 uptake (up to 2.62 mmol/g at 273K and 1 bar or 1.45 mmol/g at 298K and 1 bar) and high CO_2:N_2 selectivity (up to 25.2:1 at 298K and 1 bar).

The research performed on CMPs has focused on broadening the range of functional groups that can be incorporated into the frameworks, with the aim to tune the properties of the materials for different applications. CMPs are currently attracting considerable interest as materials that combine the mechanical stability of polymers with adjustable optoelectronic properties of organic molecules. In fact, species belonging to the family of conjugated polymers have already been exploited for some applications like optoelectronic (OLED (Organic Light Emission Diode) for photovoltaic cells and FET transistor [105, 106].

1.5.4.4 Hypercrosslinked polymers (HCPs)

HCPs represent a class of low cost porous materials, which can be prepared mainly by the Friedel Crafts alkylation reaction. The permanent porosity in HCPs is a result of extensive crosslinking reactions, which prevents the polymer chains from collapsing into a dense, nonporous state [107].

The crosslinking produces a highly rigid network structure with high thermal stability that is not commonly expected for organic polymers. Combined with their light weight properties, small pore size, micropore volume and high surface areas, HCPs can be considered as promising materials for H_2 and CO_2 storage applications [108, 109].

According to the synthetic method, HCPs can be produced by the following procedures [110]:

1. Intermolecular and intramolecular crosslinking of preformed polymer chains (either linear chains or lightly crosslinked gels). “Davankov-type” resins are the first type of hypercrosslinked materials, which have been well-studied and are prepared by post-crosslinking of linear polystyrene (PS), poly(vinylbenzyl chloride), or their pre-crosslinked copolymers with a divinylbenzene (DVB) moiety [107]. The hypercrosslinking process consists of two simple steps (Figure 10): first, the linear or lightly crosslinked polymer precursors are dissolved or swollen in a thermodynamically good solvent; this introduces space between the polymer chains. Then, the precursors are quickly cross-linked via a Friedel-Crafts alkylation reaction using a Lewis acid, such as iron (III) chloride, forming a HCP polymer chains locked in an expanded form.

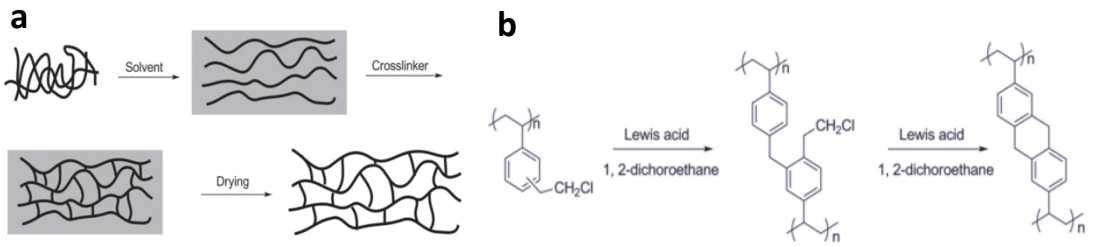

Figure 10. (a) Schematic representation of the Hypercrosslinking process; (b) Reaction scheme for the synthesis of a HCP polymer prepared from gel poly(divinylbenzene-co-vinylbenzyl chloride). Adapted from ref. 110

2. Direct step growth polycondensation of suitable monomers: this is an approach to microporous organic networks that uses bis(chloromethyl) aromatic monomers such as dichloroxylene (DCX), bis(chloromethyl)biphenyl (BCMBP), and bis(chloromethyl) anthracene (Figure 11) [102]. The HCP polymers obtained using these precursors are predominantly microporous and exhibit apparent BET surface areas of up to 1904 m^2 g^{-1} as measured by nitrogen adsorption at 77K [111]. Schwab and coworkers [112] have copolymerized BCMBP with a set of non-functionalized fluorene-based comonomers such as fluorine (FLUO), 9,9' -spirobi(fluorene) (sFLUO), dibenzofuran (DBF), and dibenzothiophene (DBT) resulting in copolymer networks, which exhibit BET surface areas up to 1800 m^2 g^{-1}.

Figure 11. Example of monomers used for the synthesis of the HCP networks. Adapted from ref. 111

3. Knitting aromatic compound polymers (KAPs) using an external crosslinking agent. This procedure has been recently developed and consists in the simple one-step Friedel-Crafts reaction between an aromatic monomer and formaldehyde dimethyl acetal (FDA): in the presence of $FeCl_3$ as catalyst various aromatic monomers can be directly crosslinked to form the highly porous networks (Figure 12) [113].

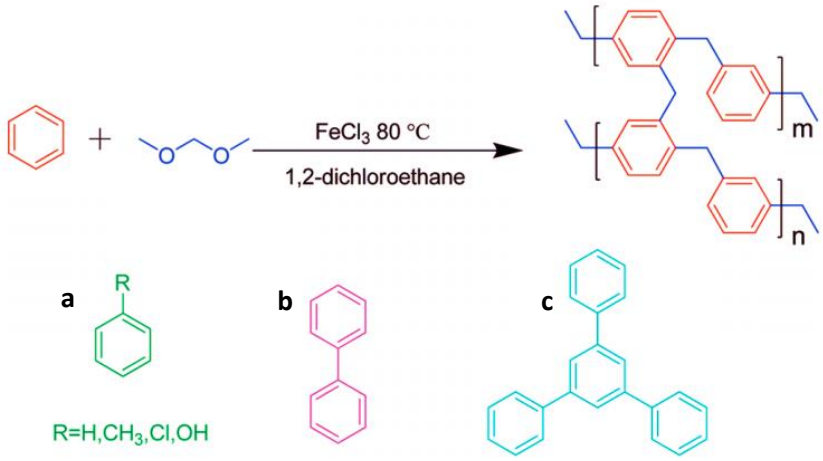

Figure 12. Scheme showing the synthetic pathway of HCP polymers using an external crosslinking agent. Structures a, b and c are example of building blocks for the network. Adapted from ref. 113

Buyi Li and coworkers have used this method to "knit" rigid aromatic building blocks, such as benzene, biphenyl, 1,3,5-triphenylbenzene, methylbenzene, chlorobenzene, and phenol obtaining surface areas up to 1391 m^2/g [113]. Also Cooper group demonstrated that this "knitting" approach can produce networks with surface area of up to 1470 $m^2\ g^{-1}$ when using the tetrahedral monomer, tetraphenylmethane [114].

This method avoids the need for monomers with specific polymerizable groups and also avoids the use of precious metal coupling catalysts. Various functional groups can also be easily introduced into the porous frameworks just by choosing the proper monomers [115, 113].

Based on the combination of large specific surface area and enhanced microporosity, HCPs show good potential for gas storage [110].

Networks based on BCMBP exhibit a H_2 storage capacity of 3.68 wt% at 15 bar and 77.3 K. The isosteric heat of sorption for H_2 on these materials is found to be in the range 6–7.5 kJ mol^{-1} [111].

The physisorption of CH_4 in organic porous materials has been less investigated than H_2 as CO_2 storage. Cooper and coworkers synthesized microporous HCPs based on poly(p-dichloroxylene), which show methane uptake up to 5.2 mmol g^{-1} (116 $cm^3\ g^{-1}$) at 20 bar and 298 K [9]. This value is comparable with many other microporous systems but falls short of materials with higher micropore volumes [116]. However, it is worth noting that these materials demonstrate a high isosteric heats of sorption for CH_4 (20.8 kJ mol^{-1}).

It was found that the CO_2 capture capacities were related to the textural properties of the HCPs [117]. The performance of these materials to adsorb CO_2 at atmospheric pressure was characterized by maximum CO_2 uptakes of 1.7 mmol g^{-1} (7.4 wt%) at 298 K. At higher pressures (30 bar), the polymers show CO_2 uptake up to

13.4 mmol g^{-1} (59 wt%), superior to zeolite-based materials [118] and commercial activated carbons [7]. In addition, these polymers showed low isosteric heats of CO_2 adsorption and good selectivity towards CO_2. These results confirmed that the HCPs have potential to be applied as CO_2 adsorbents in pre-combustion capture processes where high CO_2 partial pressures are involved.

The properties of HCPs can be fine-tuned for a specific purpose by post synthetic modification [119]. This is possible because the hypercross-linking reaction does not occur at each possible site, resulting in residual chloromethyl groups being present in the polymeric matrix. Thus, functional groups, such as amines or alcohols, can be transferred to the polymer matrix by replacing these residual chlorine atoms. This enables to improve the storage capacity of these materials and extends their application as adsorbents for toxic organic [120] and inorganic contaminants [4].

1.5.4.5 Porous aromatic frameworks (PAFs)

Porous aromatic frameworks (PAFs) are a family of microporous polyphenylic networks characterized by a three-dimensional, rigid and open-network structures. In 2009, Ben group [121, 122] developed a method to synthesize the first long range ordered porous aromatic framework (PAF) with diamond-like topology (PAF-1 or PAF-302), which had a record surface area (SBET = 5640 m^2 g^{-1}) at that time and exceptional physicochemical stability via a nickel(0)-catalyzed Yamamoto-type cross-coupling reaction.

The original idea for the synthesis of PAF-1 came from the structure and properties of diamond, in which each carbon atom is tetrahedrally connected to four neighboring atoms by covalent bonds. Breaking the C–C covalent bond of diamond and inserting rigid phenyl rings allow sufficient exposure of the faces and edges of phenyl rings with the expectation of increasing the internal surface areas.

For a long time it was thought that the low surface area of porous organic polymers was due to the amorphous structure, but thanks to PAF-1, it has been shown that even non-crystalline materials could reach very high surface areas. This exceptional surface area, according to Hong-Cai Zhou [123], is mainly due to three factors: (1) The highly efficient Yamamoto reaction helps to eliminate unreacted termini at the monomers and therefore highly connected frameworks are formed [124] (2) The default diamondoid framework topology, imposed by the tetrahedral monomers, provides widely open and interconnected pores to efficiently prevent the formation of “dead space”. (3) The prevailing robust covalent C -C bond connecting the whole framework leads to a material with exceptionally high thermal and chemical stability.

The Yamamoto coupling is an aryl–aryl coupling of aryl-halogenide compounds mediated mostly by stoichiometric amounts of bis(1,5-cyclooctadiene)nickel(0) ($Ni(COD)_2$ for short) (Figure 13).

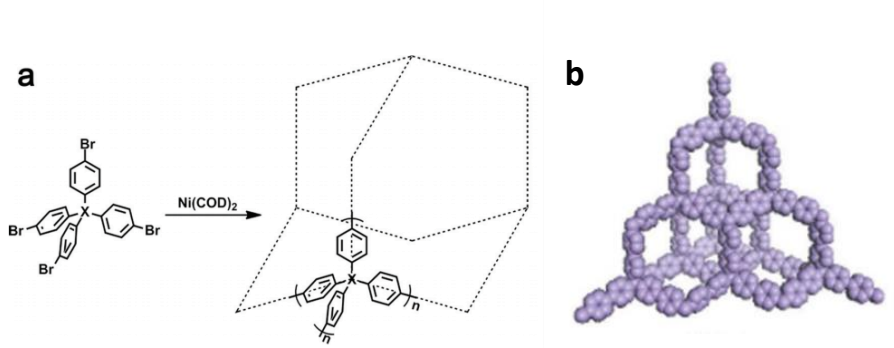

Figure 13. (a) Synthetic route for PAF-1 (x = C), PPN-4 (X = Si) and PPN-5 (X = Ge, (b) the default non interpenetrated diamond-like network of PAF-1.

The polymerization is advantageous as a self polycondensation with just a single, halogen-functionalized monomer can be used to form an organic framework.

Compared to other C–C coupling reactions, such as Sonogashira–Hagihara routes and Suzuki cross-coupling, Yamamoto coupling shows the unexpected halogen elimination ability of the ending group. This makes it unique to prepare ultrahigh porosity solids because heavy ending halogen atoms evidently decrease the surface area.

Several papers [10, 123, 125, 126] have been published on PAF-1 analogues obtained by replacing the central carbon with other quadricovalent building centers (adamantane, silicon, and germanium) (Figure 13) using the same method presented by Ben and co-workers [121], but with some variation on temperature, solvent and washing method.

Compared with other ultrahigh surface area solids such as porous carbons, porous silicas, zeolites, MOF and microporous polymers, PAFs show very high thermal (>450°C) and excellent physicochemical stabilities. They are also characterized by excellent adsorption abilities for CO_2, H_2 and CH_4 [10, 125, 126].

PAF-1 with surface area of 5640 m^2/g, demonstrates high adsorption capacity for hydrogen (10.7 wt% at 77K and 48 bar) , carbon dioxide (50 wt% at 298K and 40 bar) and methane (15 wt% at 298K and 35 bar) [121, 126], and a heat of adsorption (Qst) of 5.4 kJ mol^{-1}, 14.0 kJ mol^{-1} and 15.6 kJ mol^{-1} for H_2, CH_4 and CO_2, respectively [10].

Furthermore, PPN-4, PAF material obtained starting from quadrivalent tetraphenylsilane, has a BET surface area of 6461 $m^2\ g^{-1}$, which represents a world record BET surface area [125]. In relation to this impressive

surface area, PPN-4 can adsorb 2121 mg g^{-1} CO_2 (212 wt%) at 50 bar/295 K, 158 mg g^{-1} hydrogen at 77 K/80 bar and 389 mg g^{-1} methane at 298 K/55 bar.

To improve gas adsorption capacity in PAFs, post-synthesis treatments have also been proposed in literature:

1) KOH activation of PAF-1 at high-temperature [127]: The Carbonization was carried out by heating the PAF-1/KOH powder mixture under N_2 at 2 °C/min and a temperature ranging from 500 and 900 °C for 1 hour. After carbonization, the BET surface area of PAF-1 derivatives decreased to about 1000 m^2 g^{-1}, but showed a unique bimodal microporous structure located at 0.6 nm and 1.2 nm which revealed high Carbon dioxide, methane and hydrogen sorption in both low-pressure and high-pressure environments. In particular, K-PAF-1-750 is able to store 1320 mg g^{-1} of carbon dioxide (40 bar, RT), 207 mg g^{-1} of methane (35 bar, RT) and 71.6 mg g^{-1} of hydrogen (48 bar, 77 K). The carbon dioxide and methane high-pressure storage ability surpassed the original PAF-1.
2) Introduction of sulfonic groups onto the biphenyl frameworks. PAF-1 has been modified by reaction with chlorosulfonic acid to give sulfonate grafted acid (PPN-6-SO_3H) and lithium salt (PPN-6-SO_3Li) species. After sulfonation, the surface area of PPN-6-SO_3H and PPN-6-SO_3Li was reduced to 1254 m^2 g^{-1} and 1186 m^2 g^{-1} but the Qst increased to 30.4 and 35.7 kJ mol^{-1}. Strong interactions between the sulfonate-graft samples and carbon dioxide lead to a very high uptake capacity at 295K and 1 bar, with values of 13.1 and 13.5 wt% (equivalent to 3.6 and 3.7 mmol g^{-1}) for PPN-6- SO_3H and PPN-6-SO_3Li, respectively [128].

References:

[1] Dyer, A. An Introduction to Zeolite Molecular Sieves (Wiley, Chichester, **1988**).

[2] Hölderich, W., Hesse, M. and Näumann, F. *Angew. Chem. int.* **1988**, 27, 226−246.

[3] McKeown, N. B.; Budd, P. M. Polymers of intrinsic microporosity (PIMs): organic materials for membrane separations, heterogeneous catalysis and hydrogen storage. *Chem. Soc. Rev.* **2006**, 35, 675–683.

[4] Li, B.; Su, F.; Luo, H. K.; Liang, L.; Tan, B. Hypercrosslinked microporous polymer networks for effective removal of toxic metal ions from water. *Microporous and Mesoporous Mater.* **2011**, 138, 207–214.

[5] Du, X.; Sun, Y.; Tan, B.; Teng, Q.; Yao, X.; Su, C.; Wang, W. Tröger's base-functionalised organic nanoporous polymer for heterogeneous catalysis . *Chem. Commun.* **2010**, 46, 970–972.

[6] Dang, D.; Wu, P.; He, C.; Xie, Z.; Duan, C. Homochiral metal-organic frameworks for heterogeneous asymmetric catalysis. *J. Am. Chem. Soc.* **2010**, 132, 14321–14323.

[7] Furukawa, H.; Yaghi, O. M. Storage of Hydrogen, Methane, and Carbon Dioxide in Highly Porous Covalent Organic Frameworks for Clean Energy Applications. *J. Am. Chem. Soc.* **2009**, 131, 8875–8883.

[8] McKeown, N. B.; Gahnem, B.; Msayib, K. J.; Budd, P. M.; Tattershall, C. E.; Mahmood, K.; Tan, S.; Book, D.; Langmi, H. W. and Walton, A. Towards Polymer-Based Hydrogen Storage Materials: Engineering Ultramicroporous Cavities within Polymers of Intrinsic Microporosity. *Angew. Chem*. **2006**, 118, 1836–1839.

[9] Wood, C. D.; Tan, B., Trewin, A.; Su, F.; Rosseinsky, M. J.; Bradshaw, D.; Sun, Y.; Zhou, L. and Cooper, A. I. Microporous Organic Polymers for Methane Storage. *Adv. Mater.* **2008**, 20, 1916–1921.

[10] Ben. T.; Pei. C.; Zhang. D.; Xu. J.; Deng. F.; Jing. X.; Qiu. S. Gas Storage in Porous Aromatic Frameworks (PAFs). *Energy Environ. Sci.* **2011**, 4, 3991-3999.

[11] Deanna, M. D.; Berend, S.; Jeffrey R. L. *Angew. Chem. Int. Ed.* **2010**, 49, 6058–6082.

[12] Frota, W.M.; Sa, J.A.S.; Moraes, S.S.B.; Rocha, B.R.P.; Ismail, K.A.R. Natural gas: The option for a sustainable development and energy in the state of Amazonas. *Energy Policy.* **2010**, 38, 3830-3836.

[13] Jain, I.P. Hydrogen the fuel for 21st century. *Int. J. Hydrog. Energy.* **2009**, 34, 7368-7378.

[14] Kelly, N.A.; Gibson, T.L.; Cai, M.; Spearot, J.A.; Ouwerkerk, D.B. Development of a renewable hydrogen economy: optimization of existing technologies. *Int. J. Hydrog. Energy*. **2010**, 35, 892-899.

[15] Nath, K.; Das, D. Production and storage of hydrogen: Present scenario and future perspective. *J. Sci. Ind. Res.* **2007**, 66, 701-709.

[16] Pasculete, E.; Condrea, F.; Radulescu, C. Hydrogen and sustainable energy. Research for hydrogen production. *Environ. Eng. Manag. J.* **2007**, 6, 45-49.

[17] U.S. Department of Energy's Energy Efficiency and Renewable Energy Website. https://www1.eere.energy.gov/hydrogenandfuelcells/storage/current_technology.html(2010).

[18] Jena, P. Materials for Hydrogen Storage: Past, Present, and Future. *J. Phys. Chem. Lett.* **2011**, 2, 206–211.

[19] Mao, W. L.; Koh, C. A.; Sloan, E. D. Clathrate Hydrates under Pressure. *Phys. Today* **2007**,60, 42–47.

[20] Wang, L.; Yang, R. T. New Sorbents for Hydrogen Storage by Hydrogen Spillover: A Review. *Energy Environ. Sci.***2008**,1, 268–279.

[21] Lan, J.; Cao, D.; Wang, W.; Ben, T.; Zhu, G. High-Capacity Hydrogen Storage in Porous Aromatic Frameworks with Diamond-like Structure. *J. Phys. Chem. Lett.* **2010**,1, 978–981.

[22] Orimo, S.; Nakamori, Y.; Eliseo, J. R.; Zuttel, A.; Jensen, C. M. Complex Hydrides for Hydrogen Storage. *Chem. Rev.* **2007**, 107, 4111–4132.

[23] Gutowska, A.; Li, L.; Shin, Y.; Wang, C. M.; Li, X. S.; Linehan, J. C.; Smith, R. S.; Kay, B. D.; Schmid, B.; Shaw, W.; Gutowski, M.; Autrey, T. Nanoscaffold Mediates Hydrogen Release and the Reactivity of Ammonia Borane. *Angew. Chem., Int. Ed.* **2005**,44, 3578–3582.

[24] Zhao, Y.; Kim, Y.-H.; Dillon, A. C.; Heben, M. J.; Zhang, S. B. Hydrogen Storage in Novel Organometallic Buckyballs. *Phys. Rev. Lett.* **2005**,94, 155504.

[25] Sun, Q.; Wang, Q.; Jena, P.; Kawazoe, Y. Clustering of Ti on a C60 Surface and Its Effect on Hydrogen Storage. *J. Am. Chem. Soc.* **2005**,127, 14582–14583.

[26] Sun, Q.; Jena, P.; Wang, Q.; Marquez, M. First-Principles Study of Hydrogen Storage on Li12C60. *J. Am. Chem. Soc.* **2006**, 128, 9741 –9745.

[27] Thomas, K. M. *Adsorption and Desorption of Hydrogen on Metal-Organic Framework Materials for Storage Applications: Comparison with other Nanoporous Materials.* Dalton Trans, 2009, 1487–1505.

[28] Menon, V.C.; Komarneni, S. *Journal of Porous Materials* **1998**, 5, 43–58.

[29] Makal, T.A.; Li, J.-R.; Lu, w.; Zhou, H.-C. Methane storage in advanced porous materials. *Chem. Soc. Rev.* **2012**, 41, 7761–7779.

[30] Firas, N.R.; Mat, H.B.; Zakaria, Z. On-board adsorptive natural gas storage: hindrances for commercial applications. *Clean Technol. Transport.* **2001**, 179.

[31] Wegrzyn, J.; Gurevich, M. Adsorbent storage of natural gas. *Appl. Energy* **1996**, 55, 71−83.

[32] Burchell, T.; Rogers, M. Low pressure storage of natural gas for vehicular applications. *SAE Technol. Pap. Ser.* **2000**, 2001−2205.

[33] Ma, S. Q.; Sun, D. F.; Simmons, J. M.; Collier, C. D.; Yuan, D. Q.; Zhou, H. C. Metal-organic framework from an anthracene derivative containing nanoscopic cages exhibiting high methane uptake. *J. Am. Chem. Soc.* **2008**, 130, 1012−1016.

[34] DOE MOVE program at https://arpa-e-foa.energy.gov/.

[35] He, Y.; Zhou, W.; Yildirim, T.; Chen, B. A series of metal-organic frameworks with high methane uptake and an empirical equation for predicting methane storage capacity. *Energy Environ. Sci.* **2013**, 6, 2735–2744.

[36] Wu, H.; Zhou, W.; Yildirim, T. High-Capacity Methane Storage in Metal−Organic Frameworks M2(dhtp): The Important Role of Open Metal Sites. *J. Am. Chem. Soc.,* **2009**,131, 4995–5000.

[37] Guo, Z.; Wu, H.; Srinivas, G.; Zhou, Y.; Xiang, S.; Chen, Z.; Yang, Y.; Zhou, W.; O'Keeffe M.; Chen, B. A Metal–Organic Framework with Optimized Open Metal Sites and Pore Spaces for High Methane Storage at Room Temperature. *Angew. Chem., Int. Ed.* **2011**, 50, 3178–3181.

[38] Amini, H.R.; Reinhart, D.R. Regional prediction of long-term landfill gas to energy potential. *Waste Manage*. **2011**, 31, 2020-2026.

[39] Mandal, T.K.; Gregory, D.H.; Hydrogen: a future energy vector for sustainable development. *J. Eng. Mech. Eng. Sci.* **2010**, 224, 539-558.

[40] Boden, T.A.; Marland, G.; Andres, R.J. Global, Regional, and National Fossil-Fuel CO_2 Emissions., Carbon Dioxide Information Analysis Center, Oak Ridge National Laboratory, U.S. Department of Energy, Oak Ridge, Tenn., (USA).

[41] Liu, Y.; Wang, Z. U.; Zhou, H.-C. Recent advances in carbon dioxide capture with metal-organic frameworks. *Greenhouse Gas Sci Technol.* **2012**, 2, 239–259.

[42] Songolzadeh, M.; Ravanchi, M. T.; Soleimani, M. Carbon Dioxide Capture and Storage: A General Review on Adsorbents .*World Academy of Science, Engineering and Technology* 2012, 6, 10-24.

[43] Lu, C.; Bai, H.; Wu, B.; Su, F.; Hwang, J. F. Comparative study of CO_2 capture by carbon nanotubes, activated carbons, and zeolites. *Energy & Fuels* **2008**, 22, 3050-3056.

[44] Sing, K.S.W.; Everett, D.H.; Haul, R.A.W.; Moscou, L.; Pierotti, R.A.; Rouquerol, J.; Siemieniewska, T. Reporting physisorption data for gas/solid systems with special reference to the determination of surface area and porosity. Pure Appl. Chem. 1985, 57, 603–619.

[45] Lowell, S.; Shields, J.; Thomas, M.A.; Thommes, M. *Characterization of porous solids and powders: surface area, pore size and density.* 2004,The Netherlands: Springer.

[46] Thommes, M. Physical Adsorption Characterization of Nanoporous Materials. *Chemie Ingenieur Technik* **2010**, 82, No. 7.

[47] Thommes, M.; Cychosz, K. A. Physical Adsorption characterization of nanoporous materials: progress and challenges. *Adsorption* **2014**, 20, 233–250.

[48] McBain, J. W. *J. Am. Chem. Soc.* **1935**, 57(4), 699.

[49] Everett, D. H. *The Solid-Gas Interface.* ***1*967**, Dekker: New York.

[50] Christopher J. Rasmussen, Aleksey Vishnyakov, Matthias Thommes, Bernd M. Smarsly, Freddy Kleitz, and Alexander V. Neimark Langmuir 2010, 26(12), 10147–10157

[51] Thommes, M. *In Nanoporous Materials, Science & Engineering* (Lu, G. Q., Zhao, X. S., Eds.), Imperial College Press, **2004**, p 317.

[52] Ravikovitch, P. I.; Neimark, A. V. Experimental Confirmation of Different Mechanisms of Evaporation from Ink-Bottle Type Pores: Equilibrium, Pore Blocking, and Cavitation. *Langmuir* **2002**, 18, 9830–9837.

[53] Thommes, M.; Smarsly, B.; Groenewolt, M.; Ravikovitch, P. I.; Neimark, A. V. Adsorption Hysteresis of Nitrogen and Argon in Pore Networks and Characterization of Novel Micro- and Mesoporous Silicas. *Langmuir* **2006**, 22, 756–764.

[54] Olivier, J.P.; Conklin, W.B.; Szombathely, M. *Characterization of Porous Solids III.* Amsterdam: Elsevier **1994**, 81–9.

[55] Jagiello, J.; Tolles, D. *Fundamentals of Adsorption*. Amsterdam: Elsevier **1998**, 629–34.

[56] Lu, G. Q.; Zhao, X. S. Nanoporous Materials: Science and Engineering. *Imperial College Press* **2004**.

[57] Celzard, A.; Fierro, V. Preparing a Suitable Material Designed for Methane Storage: A Comprehensive Report. *Energy & Fuels* **2005**, 19, 573-583.

[58] Holst, J. R.; Cooper, A. I. Ultrahigh surface area in porous solids. Advanced *materials* **2010**, 22, 5212-6.

[59] Lozano-Castello, D.; Alcaniz-Monge, J.; Casa-Lillo, M. A.; Cazorla-Amoros, D.; Linares-Solano, A. Advances in the study of methane storage in porous carbonaceous materials. *Fuel* **2002**, 81, 1777-1803.

[60] Miyawaki, J.; Kanda, T.; Suzuki, T.; Okui, T.; Maeda, Y.; Kaneko, K. Macroscopic Evidence of Enhanced Formation of Methane Nanohydrates in Hydrophobic Nanospaces. *J. Phys. Chem. B* **1998**, 102 , 2187–2192.

[61] Davis, M. E. Ordered porous materials for emerging applications. *Nature* 2002, 417, 813-21.

[62] Chahine, R.; Bose, T.K.; Low-pressure adsorption storage of hydrogen. *Int J Hydrogen Energy* **1994**, 19, 161–164.

[63] Velu, S.; Ma, X.; Song, C. Selective adsorption for removing sulfur from jet fuel over zeolite-based adsorbents. *Industrial and Engineering Chemical Research* **2003**, 42, 5293-5304.

[64] Qiu, W.; Zheng, Y. Arsenate removal from water by an alumina-modified zeolite recovered from fly ash. *Journal of Hazardous Materials* **2007**, 148, 721-726.

[65] Corma, A.; Diaz-Cabanas, M. J.; Martinez-Triguero, J.; Rey, F.; Rius, J. A large-cavity zeolite with wide pore windows and potential as an oil refining catalyst. *Nature* **2002**, 418, 514-517.

[66] Van Der Waal, J. C.; Van Bekkum, H., Molecular Sieves, Multifunctional Microporous Materials in Organic Synthesis. *Journal of Porous Materials* **1998**, 5, 289-303.

[67] Zheng, Y.; Li, X.; Dutta, P. K. Exploitation of Unique Properties of Zeolites in the Development of Gas Sensors. *Sensors* **2012**, 12, 5170-5194.

[68] Hyun, S. H.; Song, J. K.; Kwak, B. I.; Kim, J. H.; Hong, S. A. Synthesis of ZSM-5 zeolite composite membranes for CO_2 separation. *Journal of Materials Science***1999**, 34, 3095.

[69] Felderhoff, M.; Weidenthaler, C.; von Helmolt, R.; Eberle, U. Hydrogen storage: the remaining scientific and technological challenges. *Phys Chem Chem Phys* **2007**, 9, 2643–2653.

[70] Lozano-Castello, D.; Cazorla-Amoros, D.; Linares-Solano,A.; Quinn, D.F. Influence of pore size distribution on methane storage at relatively low pressure: preparation of activated carbon with optimum pore size. *Carbon* **2002**, 40, 989-1002.

[71] Yürüm, Y.; Taralp, A.; Veziroglu, T. N. Storage of hydrogen in nanostructured carbon materials. *Int J Hydrogen Energy* **2009**, 34, 3784–3798.

[72] Ströbel, R.; Garche, J.; Moseley, P. T.; Jörissen, L.; Wolf, G. Hydrogen storage by carbon materials. *Journal of Power Sources* **2006**, 159, 781-801.

[73] Himeno, S.; Komatsu, T.; Fujita, S. High-Pressure Adsorption Equilibria of Methane and Carbon Dioxide on Several Activated Carbons. Journal of Chemical Engineering *Data* **2005**, 50, 369.

[74] Sevilla, M.; Fuertes, A. B. Sustainable porous carbons with a superior performance for CO_2 capture. *Energy & Environmental Science* **2011**, 4, 1765-1771.

[75] Wegrzyn, J.; Wisemann, H.; Lee, T. Low pressure storage of natural gas on activated carbon. *SAE Proc. of Annual Automotive Technology Development* **1992**, 1–11.

[76] Férey, G. Hybrid porous solids: past, present, future. *Chem Soc Rev* **2008**, 37, 191–214.

[77] Rosseinsky, M. J. Recent developments in metal-organic framework chemistry: design, discovery, permanent porosity and flexibility. *Microporous Mesoporous Mater.* **2004**, 73, 15–30 47.

[78] Rowsell, J. L. C.; Yaghi, O. M. Metal-organic frameworks: a new class of porous materials. *Microporous Mesoporous Mater*. **2004**, 73, 3–14.

[79] Murray, L. J.; Dincă, M.; Long, J. R. Hydrogen storage in metal-organic frameworks. *Chem Soc Rev* **2009**, 38, 1294-1314.

[80] Janiak, C.; Vieth, J. K. MOFs, MILs and more: concepts, properties and applications for porous coordination networks (PCNs). *New J. Chem*. **2010**, 34, 2366–2388.

[81] Furukawa, H.; Ko, N.; Go, Y. B.; Aratani, N.; Choi, S. B.; Choi, E.; Yazaydin, A. O.; Snurr, R. Q.; O'Keeffe, M.; Kim, J.; Yaghi, O. M. Ultrahigh porosity in metal-organic frameworks. *Science* **2010**, 329, 424–428.

[82] Millward, A. R.; Yaghi, O. M. Metal-organic frameworks with exceptionally high capacity for storage of carbon dioxide at room temperature. *J. Am. Chem. Soc*. **2005**, 127, 17998-17999.

[83] Chui, S. S. Y.; Lo, S. M. F.; Charmant, J. P. H.; Orpen, A. G.; Williams, I. D. A. Chemically Functionalizable Nanoporous Material [Cu- 3(TMA)(2)(H2O)(3)](n). *Science* **1999**, 283, 1148 −1150.

[84] Dietzel, P. D. C.; Panella, B.; Hirscher, M.; Blom, R.; Fjellvag, H. Hydrogen adsorption in a nickel based coordination polymer with open metal sites in the cylindrical cavities of the desolvated framework. *Chem. Commun.* **2006**, 959 −961.

[85] Farha, O.K.; Yazaydin, A.O.; Eryazici, I.; Malliakas, C.D.; Hauser, B.G.; Kanatzidis, M.G.; Nguyen, S.T.; Snurr, R.Q.; Hupp, J.T. De Novo synthesis of a metal-organic framework material featuring ultrahigh surface area and gas storage capacities. *Nature Chem.* **2010**, 2, 944-948.

[86] Germain, J.; Fréchet, J. M. J.; Svec, F. Nanoporous polymers for hydrogen storage. *Small* **2009**, 5, 1098–111.

[87] Jiang, J.-X.; Su, F.; Trewin, A.; Wood, C. D.; Niu, H.; Jones, J. T.; Khimyak, Y. Z., Synthetic control of the pore dimension and surface area in conjugated microporous polymer and copolymer networks. *Journal of the American Chemical Society* **2008**, 130, 7710-20.

[88] Makowski, P.; Thomas, A.; Kuhn, P.; Goettmann, F. Organic materials for hydrogen storage applications: from physisorption on organic solids to chemisorption in organic molecules. *Energy Environ Sci* **2009**, 2, 480–490.

[89] Ilinitch, O. M.; Fenelonov, V. B.; Lapkin, A. A.; Okkel, L. G.; Terskikh, V. V.; Zamaraev, K. I. Intrinsic microporosity and gas transport in polyphenylene oxide polymers. *Microporous and Mesoporous Materials*1999, 31, 97–110.

[90] Budd, P.M.; Butler, A.; Selbie, J.; Mahmood, K.; McKeown, N.B.; Ghanem, B.; Msayib, K.; Book, D.; Walton, A. The potential of organic polymer-based hydrogen storage materials. *Phys. Chem. Chem. Phys* **2007**, 9,1802–1808.

[91] McKeown, N. B.; Budd, P. M.; Book, D. Microporous polymers as potential hydrogen storage materials. *Macromol. Rapid Commun*. **2007**, 28, 995–1002.

[92] Côté, A. P.; El-Kaderi, H. M.; Furukawa, H.; Hunt, J. R.; Yaghi, O. M. Reticular synthesis of microporous and mesoporous 2D covalent organic frameworks. *Journal of the American Chemical Society* **2007**, 129, 12914-15.

[93] El-Kaderi, H. M.; Hunt, J. R.; Mendoza-Cortés, J. L.; Côté, A. P.; Taylor, R. E.; O'Keeffe, M., et al. Designed synthesis of 3D covalent organic frameworks. *Science* **2007**, 316, 268-72.

[94] Wang, L.; Wang, L.; Zhao, J.; Yan, T. Adsorption of selected gases on metal-organic frameworks and covalent organic frameworks: A comparative grand canonical Monte Carlo simulation. *Journal of Applied Physics,* **2012**, *111*, 112628.

[95] Tilford, R. W.; Mugavero, S. J.; Pellechia, P. J.; Lavigne, J. J. Tailoring microporosity in covalent organic frameworks. *Adv. Mater*. **2008**, 20, 2741–2746.

[96] Koo, B. T.; Dichtel, W. R.; Clancy, P. A classification scheme for the stacking of two-dimensional boronate ester-linked covalent organic frameworks. *Journal of Materials Chemistry* **2012**, 22, 17460-17469.

[97] Doonan, C. J.; Tranchemontagne, D. J.; Glover, T. G.; Hunt, J. R.; Yaghi, O. M. Exceptional ammonia uptake by a covalent organic framework. *Nature Chem.* **2010**, 2, 235-238.

[98] Assfour, B.; Seifert, G. Adsorption of hydrogen in covalent organic frameworks: comparison of simulations and experiments. *Microporous Mesoporous Mater.* **2010**, 133, 59-65.

[99] Li, Y.; Yang, R. T. Hydrogen Storage in Metal-Organic and Covalent-Organic Frameworks by Spillover. *Langmuir* **2008**, 54, 269-279.

[100] Chinchilla, R.; Najera, C. The Sonogashira reaction: a booming methodology in synthetic organic chemistry. *Chem Rev.* **2007**, 107, 874–922.

[101] Weder, C. Hole Control in Microporous Polymers. *Angew Chem.* **2008**, 47, 448–50.

[102] Jiang, J.X.; Su, F.; Trewin, A.; Wood, C. D.; Campbell, N. L.; Niu, H.; Dickinson, C.; Ganin, A. Y.; Rosseinsky, M. J.; Khimyak, Y. Z.; Cooper, A. I. Conjugated Microporous Poly(aryleneethynylene) Networks. *Angew Chem*. **2007**, 46, 8574–8.

[103] Hasell, T.; Wood, C. D.; Clowes, R.; Jones, J. T. A.; Khimyak, Y. Z.; Adams, D. J.; Cooper, A. I. Palladium nanoparticle incorporation in conjugated microporous polymers by supercritical fluid processing. *Chem. Mater.* **2009**, 22, 557–564.

[104] Ren, S.; Dawson, R.; Laybourn, A.; Jiang, J.-x.; Khimyak, Y.; Adams, D. J.; Cooper, A. I. Functional conjugated microporous polymers: from 1, 3, 5-benzene to 1, 3, 5-triazine. *Polymer Chemistry* **2012**, 3, 928-934.

[105] Grimsdale, A. C.; Leok Chan, K.; Martin, R. E.; Jokisz, P. G.; Holmes, A. B. Synthesis of light-emitting conjugated polymers for applications in electroluminescent devices. *Chemical reviews* **2009**, 109, 897-1091.

[106] Weder, C. Synthesis, processing and properties of conjugated polymer networks. *Chem. Commun*. **2005**, 43, 5378-5389.

[107] Tsyurupa, M. P.; Davankov, V. A. Porous Structure of Hypercrosslinked Polystyrene: State of the Art Mini-Review. *React. Funct. Polym.* **2006**, *66*, 768–779.

[108] Mason, C. R.; Maynard-Atem, L.; Al-Harbi, N. M.; Budd, P. M.; Bernardo, P.; Bazzarelli, F.; Clarizia, G.; Jansen, J. C. Polymer of intrinsic microporosity incorporating thioamide functionality: preparation and gas transport properties. *Macromolecules* **2011**, 44, 6471-6479.

[109] Dawson, R.; Stevens, L.; Drage, T. C.; Snape, C. E.; Smith, M. W.; Adams, D. J.; Cooper, A. I. Impact of water co-adsorption for carbon dioxide capture in microporous polymer sorbents. *J. Am. Chem. Soc.***2012**,134, 10741-10744.

[110] Xu, S.; Luo, Y.; Tan, B. Recent Development of Hypercrosslinked Microporous Organic Polymers. Macromol. *Rapid Commun.* **2013**, *34*, 471−484.

[111] Wood, C. D.; Tan, B.; Trewin, A.; Niu, H.; Bradshaw, D.; Rosseinsky, M. J.; Khimyak, Y. Z.; Campbell, N. L.; Kirk, R.; Stöckel, E.; Cooper, A. I. Hydrogen Storage in Microporous Hypercrosslinked Organic Polymer Networks. *Chem. Mater.* **2007**, *19*, 2034-2048.

[112] Schwab, M. G.; Lennert, A.; Pahnke, J.; Jonschker, G.; Koch, M.; Senkovska, I.; Rehahn, M.; Kaskel , S. Nanoporous copolymer networks through multiple Friedel–Crafts-alkylation—studies on hydrogen and methane storage. *J. Mater. Chem.* **2011**, 21, 2131-2135.

[113] Li , B.; Gong, R.; Wang, W.; Huang, X.; Zhang, W.; Li, H.; Hu, C.; Tan, B. A New Strategy to Microporous Polymers: Knitting Rigid Aromatic Building Blocks by External Cross-Linker. *Macromolecules* **2011**, *44*, 2410-2414.

[114] Dawson, R.; Stöckel, E.; Holst, J.R.; Adams, D. J.; Cooper, A. I. Microporous Organic Polymers for Carbon Dioxide Capture. *Energy Environ. Sci.* **2011**, *4*, 4239-4245.

[115] Luo, Y.; Li, B.; Wang, W.; Wu, K.; Tan, B. Hypercrosslinked Aromatic Heterocyclic Microporous Polymers: A New Class of Highly Selective CO_2 Capturing Materials. *Adv. Mater*. **2012**, 24, 5703–5707.

[116] Eddaoudi, M.; Kim, J.; Rosi, N.; Vodak, D.; Wachter, J.; O'Keeffe, M.; Yaghi, O. M. Systematic design of pore size and functionality in isoreticular MOFs and their application in methane storage. *Science* **2002** , 295, 469-472.

[117] Martìn, C. F.; Stöckel, E.; Clowes, R.; Adams, D. J.; Cooper, A. I.; Pis, J. J.; Rubiera, F.; Pevida, C. Hypercrosslinked Organic Polymer Networks as Potential Adsorbents for Pre-Combustion CO_2 Capture. *J. Mater. Chem*. **2011**, *21*, 5475–5483.

[118] Liewellyn, P. L.; Bourrelly, S.; Serre, C.; Vimont, A.; Daturi, M.; Hamon, L.; De Weireld, G.; Chang, J.-S. Hong, D.-Y.; Kyu Hwang, Y.; Hwa Jhung, S.; Hwa Jhung, G. F. High Uptakes of CO_2 and CH_4 in Mesoporous Metal Organic Frameworks MIL-100 and MIL-101. *Langmuir* **2008** , 24, 7245-7250.

[119] Pan, B. C.; Xiong, Y.; Li, A. M.; Chen, J. L.; Zhang, Q. X.; Jin, X. Y. Adsorption of aromatic acids on an aminated hypercrosslinked macroporous polymer. *Reactive & Functional Polymers* **2002**, 53, 63-72.

[120] Chang, C. F.; Chang, C. Y.; Hsu, K. E.; Lee, S. C.; Holl, W. Adsorptive removal of the pesticide methomyl using hypercrosslinked polymers. *Journal of Hazardous Materials* **2008**, 155, 295-304.

[121] Ben, T.; Ren, H.; Ma, S.; Cao, D.; Lan, J.; Jing, X.; Wang, W.; Xu, J.; Deng, F.; Simmons, J. M.; Qiu, S.; Zhu, G. Targeted Synthesis of a Porous Aromatic Framework With High Stability and Exceptionally High Surface Area. Angew. Chem., Int. Ed. 2009, 48, 9457-9460.

[122] S. Qiu, G. Zhu, T. Ben (2009) "Porous Polymer and synthetic method thereof". Patent: US 2010/0331436 A1

[123] Lu, W. G.; Yuan, D. Q.; Zhao , D.; Schilling, C. I.; Plietzsch, O.; Muller, T.; Brase, S.; Guenther, J.; Lumel, J.; Krishna, R. et al. Porous Polymer Networks: Synthesis, Porosity, and Applications in Gas Storage/Separation. Chem. Mat. 2010, 22, 5964-5972

[124] Trewin, A.; Cooper, A. I. Porous organic polymers: distinction from disorder?. Angew. Chem. 2010, 49, 1533–1535.

[125] Yuan, D.; Lu, W.; Zhao, D.; Zhou, H. C. Highly Stable Porous Polymer Networks With Exceptionally High Gas-Uptake Capacities. Adv. Mater. 2011, 23, 3723-3725.

[126] Holst, J. R.; Stockel, E.; Adams, D. J.; Cooper, A. I. High Surface Area Networks from Tetrahedral Monomers: Metal-Catalyzed Coupling, Thermal Polymerization, and "Click" Chemistry. Macromolecules 2010, 43, 8531-8538.

[127] Li, Y.; Ben, T.; Zhang, B.; Fu, Y.; Qiu, S. Ultrahigh Gas Storage both at Low and High Pressures in KOH-Activated Carbonized Porous Aromatic Frameworks. Scientific Reports, 2013, 3, 2420.

[128] Lu, W.; Yuan, D.; Sculley, J.; Zhao, D.; Krishna, R.; Zhou, H. Sulfonate-grafted porous polymer networks for preferential CO2 adsorption at low pressure. J. Am. Chem. Soc. 2011, 133, 18126-18129.

CHAPTER 2

Synthesis of 3D porous aromatic frameworks (PAFs) using Yamamoto homo-coupling

2.1 Introduction

In this chapter the synthesis and characterization of polyaromatic polymers belonging to the porous aromatic framework (PAF) family will be discussed and, in particular, the synthesis of PAF-302, also known as PAF-1, synthesized for the first time by the group of Ben in 2009 [1], will be treated.

PAF-302 is obtained by the polymerization of tetrakis(4-bromophenyl)methane (Figure 2.1) under an Ullmann type coupling (Yamamoto reaction) catalyzed by Ni(0) compounds.

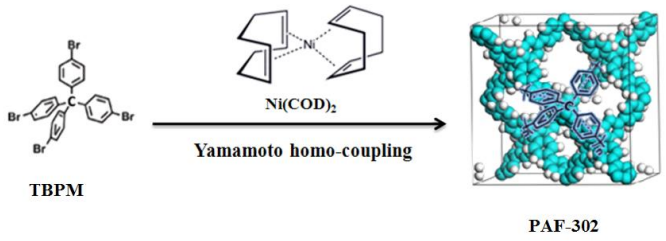

Figure 2.1. Representation of the synthesis of PAF-302 using $Ni(COD)_2$ as catalyst.

The Yamamoto coupling was initially studied by Semmelheck and co-workers [2]; this type of coupling can be applied to a wide range of aromatic compounds under various reaction conditions. In general, the Yamamoto coupling is an aryl–aryl coupling of aryl-halogenide compounds mediated mostly by stoichiometric amounts of bis(1,5-cyclooctadiene)nickel(0)[$Ni(COD)_2$].
The standard reaction conditions for coupling of aromatic halides, provide the use of the zero valent nickel complex $Ni(COD)_2$ as catalyst, the 2,2'-bipyridine (BYP) or triphenylphosphine (PPh_3) as auxiliary ligands at temperatures of about 50-80°C in polar solvents such as DMF [3].

Yamamoto and coworkers [3] studied the mechanism of the reaction of aromatic halides and in particular phenyl bromide, using the system $Ni(COD)_2$ – bipyridine. The mechanism of Yamamoto coupling is shown in Figure 2.2.

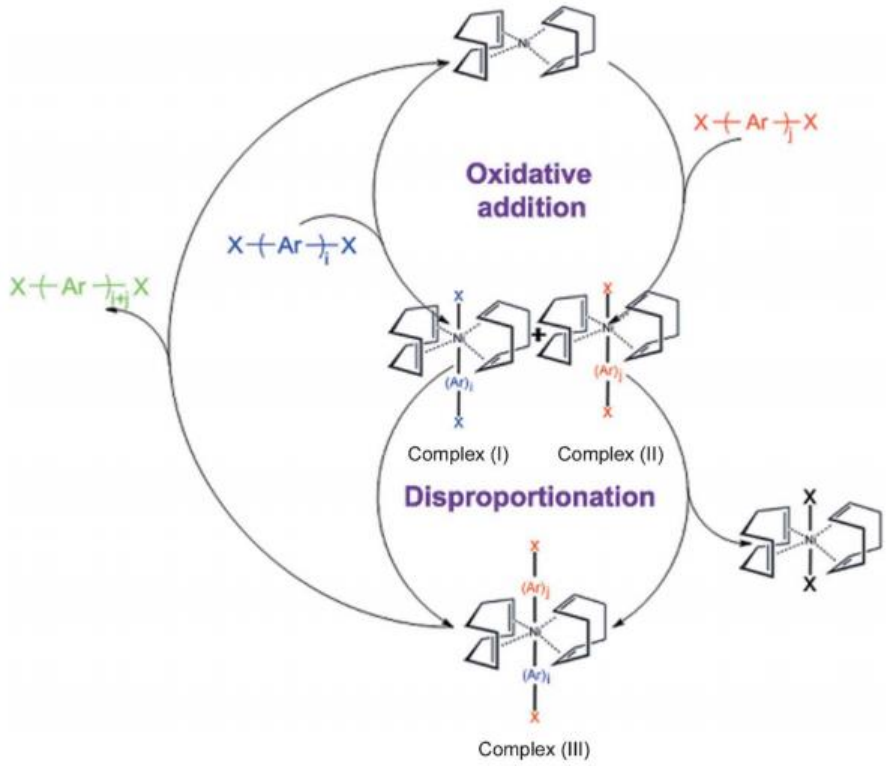

Figure 2.2. Mechanism of Yamamoto coupling, where X = halogen atom. Adapted from ref. 4

The basic steps in the polymerization reaction using Ni(0) are [3, 5]:

- The insertion of Ni (0) in the CX bond (oxidative addition);
- The disproportion between the adducts formed; and finally
- The reductive elimination of the Ni (II) compound.

Firstly, the oxidative addition occurs between Ni(0)Lm and the halogen-functionalized monomer. After the disproportionation of the two nickel complexes (I) and (II), reductive elimination of complex (III) lead to regeneration of Ni(0)Lm and an addition product. During the recycling period of the coupling reaction, stoichiometric Ni(0)Lm is consumed when an aryl–aryl bond is formed. This process is irreversible and sequesters Ni that is no longer available for the catalytic cycle: for this reason the $Ni(COD)_2$ has to be used in excess (1.2–2.8 equiv per aryl–aryl bond formed) to obtain the desired product in high yield [6].

Yamamoto reaction is advantageous as only one type of functionality is required and just a single, halogen-functionalized monomer can be used to form high molecular weight polyaromatics frameworks. Compared with other C–C coupling reactions such as Sonogashira–Hagihara route and Suzuki cross-coupling, Yamamoto

coupling shows the unexpected ability to eliminate terminal halogen atoms. This makes the reaction unique to prepare ultrahigh porous solids because heavy ending halogen atoms lead to solids with low surface area [7].

On the other hand, stoichiometric (or excess) quantities of the nickel complex are required because the catalyst is very sensitive. Moreover, this catalyst is very expensive and toxic. For these reasons, the *in situ* preparation of the catalyst has been evaluated in this work. Another type of optimization for the material PAF-302 has concerned the use of microwave irradiation as an alternative route to heat source. This technique generally has several advantages including the very fast and homogeneous heating that can result in the reduction of side reactions, cleaner products, and higher yields.

Besides the optimization of the experimental conditions for the synthesis of PAF-302 in order to obtain reproducible high surface area materials, as well as the reduction of the costs of the synthesis, particular attention has been paid to the improvement of the storage capacity, especially for CO_2 capture, by introducing amine groups in the material.

The experimental work in this chapter concerns:

- Starting from the synthesis reported in the literature, the synthetic strategy has been optimized in order to allow the preparation of PAF-302 with reproducible high surface areas.
- PAF-302 polymer was synthesized generating directly in situ the catalyst $Ni(COD)_2$, in order to minimize the costs of the synthesis.
- Synthesis of PAF-302 using the procedure reported in literature but assisted by microwave.
- Functionalization of PAF-302 with amine groups in order to improve gas storage adsorption and in particular CO_2 adsorption; two methods were used to introduce amines, the first starting from the monomer (4-Bromo-3-phtalimidomethyl)phenyl)tris(4-bromophenyl)methane), which was coupled using Yamamoto reaction, and the second was a post-synthesis treatment in which amine groups were introduced using a plasma technique.

A comparative investigation of the physico-chemical properties of the synthesized materials was carried out by a multidisciplinary approach using infrared (IR) and Solid State Nuclear Magnetic Resonance (SS-NMR) spectroscopy and powder X-ray diffraction (PXRD) to evaluate the structural characteristics of the materials. Thermal gravimetric analysis (TGA) was used to study the thermal stability of the polymers. However, the key parameters adopted to demonstrate the success of the synthesized materials are the pore diameter distribution, the pore volume and the surface area measured by N_2 physisorption at 77K. The capacity storage of CH_4, H_2 and CO_2 for best materials will be evaluated in chapter 4. Theoretical calculations concerning the FTIR spectra, pore distributions and capacity storage of gases were used to help the interpretation of both spectroscopic and adsorption isotherm results.

2.2 Experimental section: material syntheses

Particular attention was paid to the synthetic procedure since all the polymerization reactions described in this chapter are sensitive to moisture and air; All the glassware used was dried in a stove at 110°C for 18 h and the syntheses carried out under conditions of an Ar atmosphere. The solvents and reagents used in the syntheses were purchased from Sigma Aldrich and Alfa Aesar and were used without further purification except for the anhydrous DMF, which was degassed under a stream of nitrogen prior to its use and THF, which was anhydrified under sodium and benzophenone.

Synthesis of PAF-302. PAF-302 was synthesized following a procedure adapted from the literature [1]. 1,5-cyclooctadiene (COD, 1.05 mL, 8.56 mmol) was added to a solution of bis(1,5-cyclooctadiene)nickel(0) ([$Ni(cod)_2$, 2 g, 7.27 mmol) and 2,2'-bipyridyl (1.28 g, 8.19 mmol) in anhydrous THF:DMF (52:48 mL), and the mixture was kept at room temperature for 1 h. The resulting purple solution was cooled to -7°C and then Tetrakis(4-bromophenyl)methane [8] (1g, 1.57 mmol), dissolved in 20 mL of anhydrous THF, was added. The mixture was stirred overnight with temperature raising from -7°C to 20°C, to obtain a deep purple suspension. In the morning, 6M HCl (80mL) was added to the mixture that was stirred for an additional hour. After filtration, the residue was treated with 80 mL of HCl and DMF (1: 1) and stirred overnight. The solid was finally collected by filtration, washed with THF and water and dried in oven at 110°C overnight to afford PAF-302 as an off-white powder (473 mg, 95% yield). Elemental analysis found: C, 93.67 %, H, 5.23 %.

Synthesis of PAF-302 in situ. This methodology is characterized by the *in situ* formation of the active catalyst Ni(0) necessary for the Yamamoto polymerization reaction [9]. A 100 ml schlenk flask equipped with a magnetic stirring bar was charged with bis(acetylacetonate) nickel (II) (1.58 g; 6.15 mmol) and briefly dried under vacuum heating at about 80°C. After cooling and establishing an argon atmosphere, the solid was suspended in 10 mL of anhydrous THF and left under stirring for 15 min. Then 1,5-cyclooctadiene (3 mL; 24 mmol) was added and the suspension was kept under vigorous stirring for other 15 min and cooled to ca. - 80 ° C with liquid nitrogen/acetone bath. A 1.0 M solution of diisobutyl aluminum hydride in THF (15.3 mL; 85.85 mmol) was added dropwise over 1h, to give a dark reddish-brown solution. The mixture was allowed to warm to 0 °C over a 1h period. This is the key stage in the formation of the catalyst: the temperature should be raised gradually in order to precipitate enough catalyst for the polymerization reaction.

The solution is maintained at 0°C and diluted with anhydrous DMF (14 mL) and THF (26 mL). Then 2,2'-bipyridyl (0.68 g; 4.35 mmol) dissolved in anhydrous DMF (10 mL) and 1,5-cyclooctadiene (0.5 mL; 4.08 mmol) were added dropwise. After one hour the solution was cooled to -7 °C and Tetrakis(4-bromophenyl)methane (0.52 g; 0.82 mmol), dissolved in 10 mL of anhydrous THF, was added dropwise. The suspension was stirred at temperatures ranging between -7 and 20 °C overnight to obtain a black suspension.

After that, methanol (20 mL), water (5 mL) and 6M HCl (60 mL) were added to the mixture that was left under stirring for a 2h period. The residue was filtered and treated with HCl and DMF (1: 1) and stirred overnight. The solid was collected by filtration, washed with THF, ethanol and water and dried in oven at 110°C overnight to afford PAF-302 *in situ* as an off-white powder (213 mg, 82 % yield). Elemental analysis found: C, 92.42 %, H, 5.60 %.

Synthesis of microwave assisted PAF-302 (PAF-302-MW). 1,5-cyclooctadiene (COD, 0.55 mL, 4.48 mmol) was added to a solution of bis(1,5-cyclooctadiene)nickel(0) ([Ni(cod)$_2$, 1 g, 3.63 mmol) and 2,2'-bipyridyl (0.65 g, 4.16 mmol) in anhydrous DMF (60 mL), and the mixture was kept at room temperature for 1,5 h. The resulting purple catalytic solution was added to Tetrakis(4-bromophenyl)methane (0.5g, 0.79 mmol) into a glass microwave tube and heated by microwave irradiation at 80°C with stirring for 105 min at a power of 80 W. The solid was collected by filtration and washed as described in the synthesis of PAF-302 to obtain 228 mg of an off white powder (92 % yield). Elemental analysis found: C, 88.32 %, H, 4.73 %, N, 1.42 %. Elemental analysis results showed residual amount of nitrogen, probably deriving from 2,2'-bipyridyl trapped in the pores.

Synthesis of PAF-302-CH_2NH_2. PAF-302-CH_2NH_2 was synthesized following a modified literature procedure [10]. 1,5-cyclooctadiene (COD, 1.05 mL, 8.56 mmol) was added to a solution of bis(1,5-cyclooctadiene)nickel(0) ([Ni(cod)$_2$, 2 g, 7.27 mmol) and 2,2'-bipyridyl (1.28 g, 8.19 mmol) in anhydrous THF:DMF (52:48 mL), and the mixture was kept at room temperature for 1 h. (4-Bromo-3-phtalimidomethyl)phenyl)tris(4-bromophenyl)methane) [10] (1g, 1.31 mmol), dissolved in 20 mL of anhydrous THF, was added to the resulting purple solution, previously cooled to - 7 ° C using ice and salt. The mixture was stirred at temperatures ranging between -7 and 20 °C overnight. Then, 6M HCl (80 mL) was added to the mixture that was stirred for an additional hour. After filtration, the residue was treated with THF and stirred for other 2h. The solid was collected by filtration, washed with methanol and water and dried in oven at 110°C overnight to afford PAF-302-CH_2-phthalimide as an off-white powder (400 mg, 66,8 % yield).
To obtain PAF-302-CH_2NH_2, PAF-302-CH_2-phthalimide (400 mg), hydrazine monohydrate (4 mL, 82,4 mmol) and EtOH (36 mL) were combined in a flask and refluxed at 85 ºC for 48 h using an oil bath. The PAF-302-CH_2NH_2 was collected by filtration, washed with DMSO, DMF, and EtOH (100 mL each), and dried under vacuum to afford an off-white powder that was then Soxhlet extracted with EtOH for 18 h. 245 mg of product (yield = 84.2 %) were obtained after drying under vacuum. Elemental analysis found: C, 81.09 %, H, 5.24 %, N, 4.35 %.

The synthetic scheme for the synthesis of PAF-302-CH_2NH_2 is shown in figure 2.3.

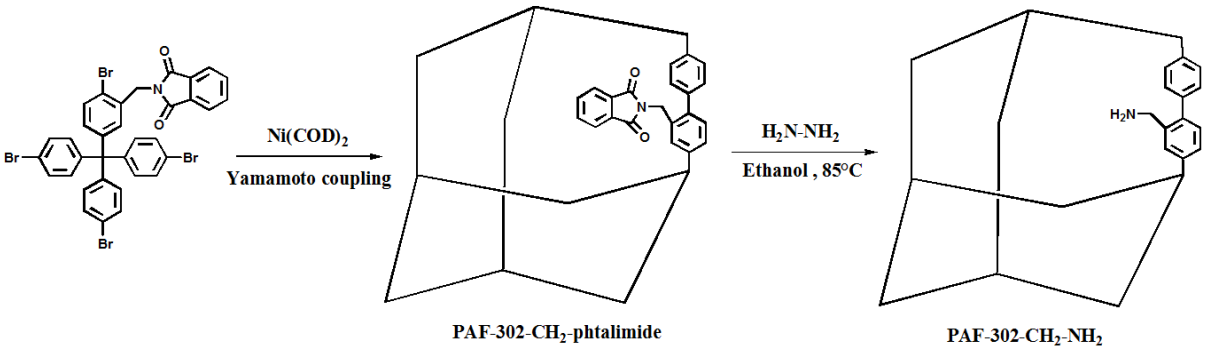

Figure 2.3. Schematic representation of the PAF-302-CH_2NH_2 synthesis.

Modification of PAF-302 surface with plasma treatment. The system employed for plasma coating was based on atmospheric plasma pressure dielectric barrier discharge (APP-DBD Platex 600-Grinp SrL) equipped with a stainless-steel parallel plate electrode of 800 mm x 230 mm x 35 mm size, providing self-plasma impedance adapting glow discharge (Grinp SrL patent). The maximum attainable process power is 2500 W. A rotary pump and a heating chamber were used to vaporize the precursor. The PAF-302 surface was modified by gas plasma at atmospheric pressure using 1,2-diaminopropane (DAP) as precursor to add amino groups. Helium gas was used as a carrier to introduce the precursor into the plasma region. The system is optimized so that the powder material is surrounded by a uniform plasma which activates throughout space reactions. Elemental analysis found: C, 77,94 %, H, 5.44 %, N, 6,81 %.

2.3 Results and discussion

2.3.1 Comparison of PAF-302 obtained with different methods

The synthesis of **PAF-302** is carried out with the Yamamoto reaction as reported by Ben et al. [1]. This synthesis is characterized by very critical conditions that influence the porosity of the final polymer. In our laboratory we have tried first to synthesize the material using the same procedure reported in the literature, but we systematically obtained materials with very low surface area. Several experimental conditions were tested by changing ligands and catalyst and we found that one of the most crucial parameter was the reaction temperature: instead of working at 80 ° C the reaction was in fact carried out between -7 ° C and 20 ° C. In this way it was possible to obtain a material with very high surface area, similar to those reported in the literature for PAF-302. However, the $Ni(COD)_2$ catalyst is very expensive and at the same time it does not ensure a good reproducibility due to an intrinsic instability of the catalyst itself.

The main objective of PAF-302 synthesis was to reduce the costs for the production of this material and to ensure that the reaction conditions are reproducible. Since the only efficient catalyst in this case is shown to be the $NiCOD_2$, our work was aimed at producing this catalyst directly in situ. The final reaction procedure is given in section 2.2, and provides for the formation of the catalyst in situ, and subsequently ligands, solvents and reagents needed for the polymerization reaction were added. In this way it was possible to obtain a material, named **PAF-302 *in situ***, with a surface area not as high as that obtained using the traditional synthesis but with better microporsity.

Another synthesis of PAF-302 treated in this thesis deals with the use of unconventional microwave assisted heating to get **PAF-302-MW**. It is well-known that the assisted-microwave polymerization leads to faster and cleaner polymerization procedures and can results in accelerated reactions and reduced side reactions. Our goal here is to evaluate if the porous properties of the material are modified in these conditions.

2.3.1.1 FTIR spectroscopy of PAF-302

At the beginning we report the assignment of the IR spectrum of the PAF-302 obtained by traditional synthesis, comparing it with the experimental and calculated spectra of tetrakis(4-bromophenyl) methane (TBPM), the precursor used in the synthesis of PAF-302. Later, we will show the comparison between the FTIR spectra of the polymers obtained by different synthetic methods.

IR spectrum of PAF-302 was interpreted by comparison with the spectrum of TBPM, whose vibrational frequencies were assigned with the help of theoretical calculations. Theoretical calculations were performed both at the DFT (Density Functional Theory) level and with the correlated MP2 (second order Moller-Plesset perturbation) method. The detailed computational method is described in ref. 11.

In Figure 2.4 we report the FTIR vibrational spectrum of PAF-302 polymer along with the spectrum of the precursor, TBPM.

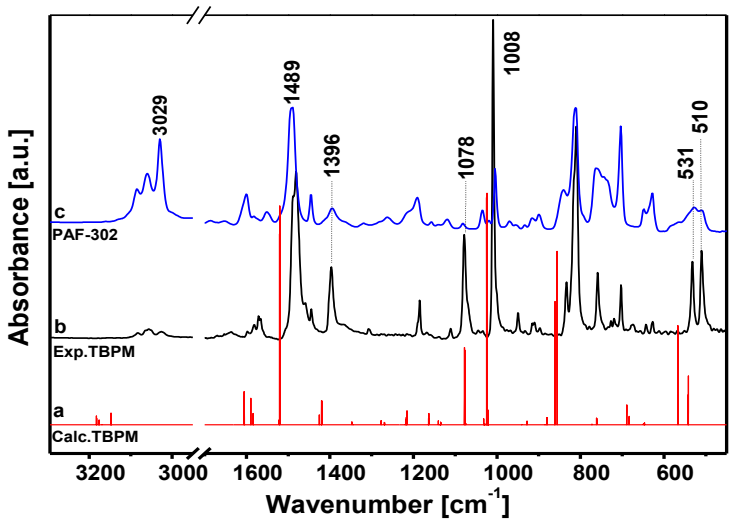

Figure 2.4. (a) DFT IR spectrum of TBPM; (b) and (c) experimental IR spectra of TBPM and PAF-302 in KBr pellet, respectively.

TBPM vibrational bands were assigned by comparison with a theoretical spectrum calculated at the B3LYP/6-311G(2d,2p) level: the main components are listed in Table 2.1. From the data reported in table 2.1 and figure 2.4, one can see that the theoretical (a) and experimental (b) TBPM spectra are in good agreement, presenting only a small shift due to the harmonic approximation adopted for the calculated spectrum.

Table 2.1: IR vibrational modes of the TBPM calculated spectrum compared to those of the TBPM and PAF-302 experimental spectra.

Vibrational mode	TBPM Calc. Freq. [cm^{-1}]	TBPM Exp. Freq [cm^{-1}]	PAF-302 Exp. Freq. [cm^{-1}]
Stretch aromatic C-H	3183, 3176, 3147	3083(vw), 3057(vw), 3026 (vw)	3085(w), 3059(m), 3029(s)
Ring quadrant stretch	1605-1583	1603-1555	1621-1531
Semicircle stretch pair	1520, 1420	1481(s), 1396 (m)	1489(s), 1394 (w)
In plane C-H bend	1215	1185	1190
C-Br stretch	1077	1078 (m)	1081 (vw)
Ring C-C bend + C-H bend + C-Br stretch	1024	1008 (vs)	1005 (m)
Ring and C-H out of plane bend	861, 761	810(s), 759	812(m), 761
In plane ring bend	689	702	703
Out of plane quadrant ring bend + C-Br bend	566, 541	531(m), 510(m)	557-497 (w)

vs= very strong, s=strong, m= medium, w=weak and vw= very weak

The FTIR spectrum of TBPM shows sharp bands because of the crystalline nature of the compound. Three very weak bands are found in the high frequency region at 3085, 3059 and 3029 cm^{-1}, which are assigned to the CH stretching vibrations of the aromatic rings on the basis of the calculated spectrum and in agreement with the literature [12, 13].

Likewise, in the low frequency region the bands falling at 1481 and 1396 cm^{-1} were assigned to "semicircle stretching pair" modes of the aromatic rings. The band at 1078 cm^{-1} is an almost pure C-Br stretching mode, whereas the intense and sharp band at 1008 cm^{-1} is assigned to the C-C bending of the aromatic rings coupled with C-H bending and C-Br stretching vibrations. At lower frequencies the bands with medium intensity at 531 and 510 cm^{-1} are assignable to the out of plane quadrant ring bending deformations somehow coupled with the C-Br deformation.

These results have allowed us to assign with more precision the IR bands of the PAF-302 polymer (Figure 2.4c). The comparison between PAF-302 and TBPM spectra shows that in general the bands of the polymer become broader, change in intensity, and slightly shift. Indeed, after polymerization reaction the high frequency bands intensity largely increases due to the change of the local dipole moment related to the aromatic ring asymmetric CH stretching. Furthermore, the bands at 1396, 1008, 531 and 510 cm^{-1} assigned to the aromatic ring stretching and bending (the last three being coupled to C-Br vibrations) undergo a drastic intensity reduction in the PAF-302 polymer: it can be thus inferred that the dipole moment of these modes is strongly influenced by the presence of bromine atoms in the TBPM precursor. The main fingerprint of the polymerization is, however, related to the band at 1078 cm^{-1} due to the C-Br vibration, which diminished to an undetected level in the PAF-302 spectrum, suggesting complete reaction of the starting TBPM.

The comparison of the FTIR spectra of the PAF-302 (curve a), PAF-302 in situ (curve b) and the PAF-302-MW (curve c) is shown in Figure 2.5.

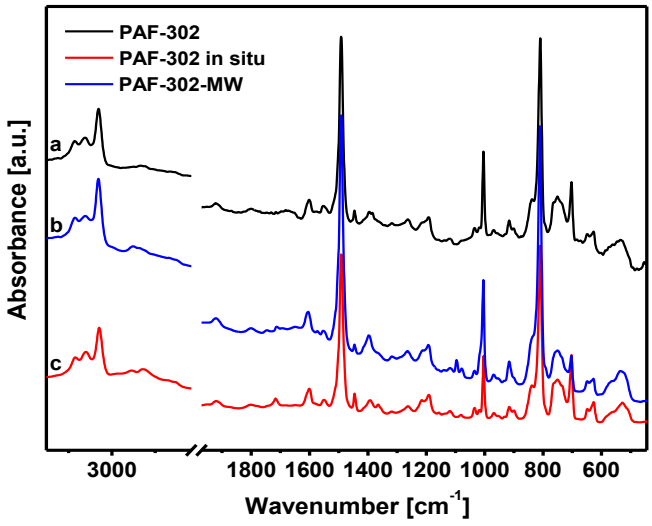

Figure 2.5. FTIR experimental spectra of: (a) PAF-302 (b) PAF-302 *in situ* and (c) PAF-302-MW in KBr pellet.

The three spectra are very similar, suggesting that the PAF-302 materials obtained by different methods have the same structure of PAF-302 obtained with traditional synthesis.

2.3.1.2 Solid-state ^{13}C MAS NMR

The samples were also characterized by solid state NMR spectroscopy in order to obtain information on the local structure. Figure 2.6 shows the comparison of the ^{13}C CP-MAS NMR spectra of PAF-302 (curve a), PAF-302 in situ (curve b) and PAF-302-MW (curve c).

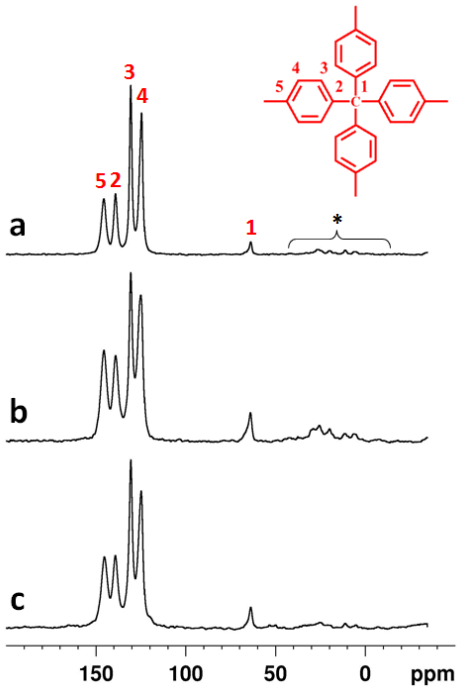

Figure 2.6. ^{13}C solid state CPMAS NMR spectra of: (a) PAF-302, (b) PAF-302 in situ and (c) PAF-302-MW. A cross polarization contact time of 5 ms and a MAS spin rate of 5 kHz were used in the experiment. * denotes spinning sidebands. The inset shows the local structure of the polymers.

Also in this case the three spectra are quite similar, showing five signals at 146, 138, 131, 125 and 64 ppm, that indicate the presence of five carbon atoms with different chemical environment.

The signal at 146 ppm is due to carbon 5 (inset of figure 2.6). The peak at 138 ppm is assigned to carbon 2, whereas the tetrahedral carbon 1 gives rise to the peak at 64 ppm. The remaining two signals at 131 and 125 ppm respectively are related to the carbon atoms in the positions 3 and 4.

The solid-state ^{13}C CP-MAS NMR spectra are consistent with that previously [1] reported for PAF-302 and suggest a regular short-range organization of biphenyl groups around tetrahedral carbon atoms.

2.3.1.3 PXRD measurements

Powder X-ray diffraction (PXRD) profiles for PAF-302 (curve a), PAF-302 in situ (curve b) and PAF-302-MW (curve c) are reported in the Figure 2.7.

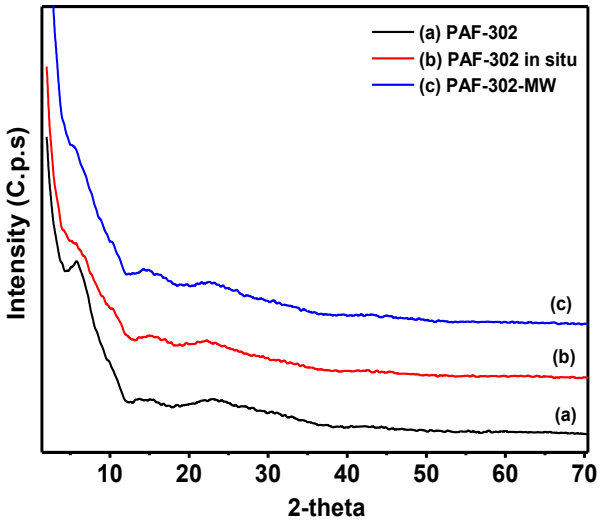

Figure 2.7. PXRD patterns of PAF-302 (a), PAF-302 in situ (b), PAF-302-MW (c) samples

The measured PXRD patterns are in good agreement with the pattern reported in literature [1]. These patterns indicate that the polymer lacks of long-range periodicity probably because the phenyl rings are not perfectly aligned each other in the particle.

2.3.1.4 Thermogravimetric analysis (TGA)

Thermogravimetric analysis (TGA) was used to investigate the thermal stability of PAF-302 , PAF-302 in situ and PAF-302-MW. Before analysis, to remove the adsorbed solvents the samples were treated at 250 ° C for 5 h. The curves related to the three materials are reported in figure 2.8.

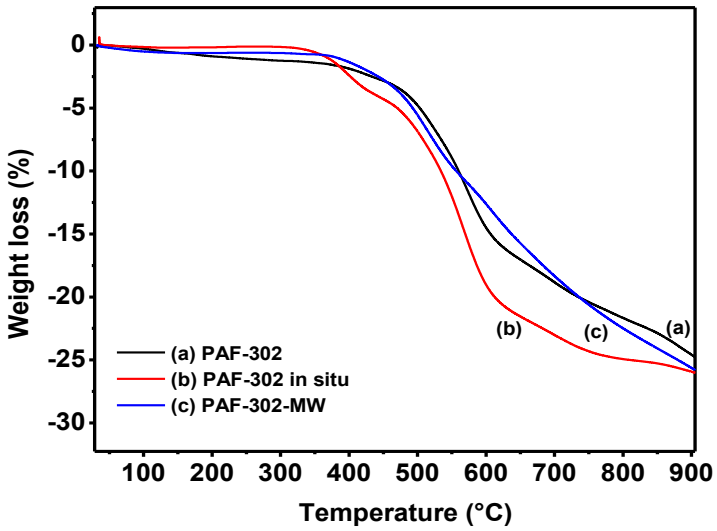

Figure 2.8. TGA plots of (a) PAF-302, (b) PAF-302 in situ and (c) PAF-302-MW samples, run at 2 °C/min under argon atmosphere up to a maximum temperature of 900 °C

TGA profiles confirmed the good thermal stability of all the polymers and their high decomposition temperature in argon atmosphere. The figure show a first 2.5 - 3% weight at 350-450 °C due to impurities trapped inside the porous systems. The decomposition of the polymers begins at approximately 450 °C and the weight loss of the networks are about 23 % at 900 °C.

2.3.1.5 Textural properties of PAF-302 samples

N_2 physisorption measurements were performed at 77K to investigate the porosity of PAF-302 samples. Before the analysis, the samples were outgassed at 250°C for 18 hours to remove adsorbed solvents.

The resulting physisorption isotherms (frame A) and pore size distribution (frame B) for PAF-302, PAF-302 in situ and PAF-302-MW samples are reported in Figure 2.9, showing again a very similar behavior for the three materials.

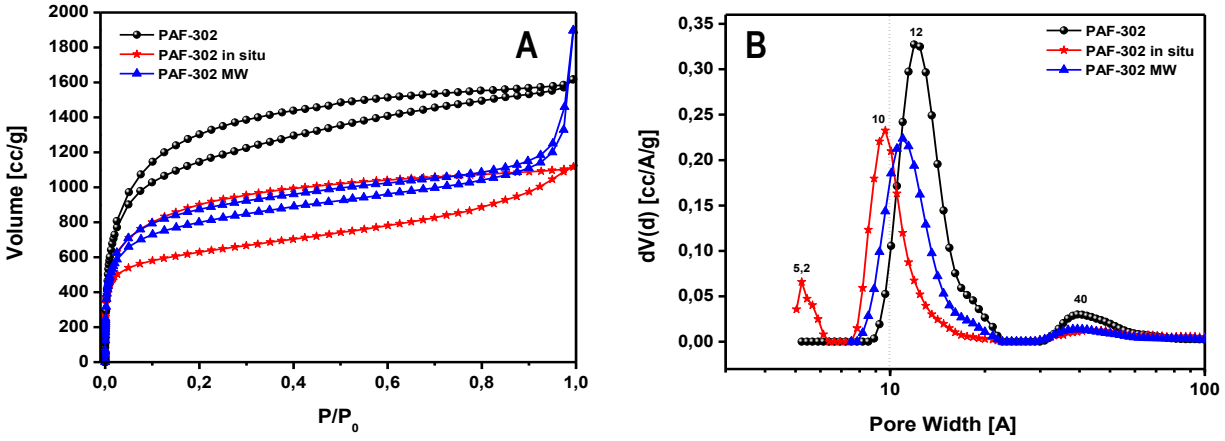

Figure 2.9 N_2 adsorption-desorption isotherms at 77K and relative pressures (P/P_0) from $1x10^{-7}$ to 1 (A) and pore size distribution determined by QSLDFT methods (B) of PAF-302 (black spheres), PAF-302 in situ (red stars) and PAF-302-MW (blue tringles).

The isotherms can be described as type I following IUPAC classification in the adsorption branch, with large quantities of gas (>500 cm^3/g and up to 1000 cm^3/g) adsorbed at low relative pressures, which is a signature feature of microporous materials. All the materials showed a H1-type hysteresis loop in the desorption branch, which could be due to: (i) mesoporosity, (ii) the swelling effects of soft porous organic materials and defects of PAFs [14].

The specific surface area (SSA) of the materials was estimated by BET method, calculated over a relative pressure range P/P_0 = 0.017−0.15. This pressure range was calculated using the "Micropore BET Assistant", a program that is implemented in ASiQWin Quantachrome software to facilitate the selection points within the linear range of the BET plot for microporous materials.

The PAF-302 sample shows a SSA of 4293 m^2/g, which is somewhat lower than the value of 5600 m^2/g published by Ben et.al [1]. Although the reaction was repeated several times, the surface area of 5600 m^2/g has never been achieved with our procedure. The sample of PAF-302-MW synthesized using Microwave assisted heating shows a BET surface area of 2966 m^2/g, whereas PAF-302 in situ sample gives a surface area of 2200 m^2/g.

PAF-302 materials studied in this work can be considered as a nanoporous material with diamond-like structure. In the literature [15], the most widely used procedure to describe pore distributions are modern microscopic methods based on statistical mechanics such as nonlocal density functional theory (NLDFT). The application of methods based on NLDFT allows one not only to describe the adsorption and phase behavior of fluids in pores at a molecular level, but also to obtain an accurate pore size distribution over the complete micro/mesopore range [16]. Recently, a novel approach has been suggested to account for the effect of roughness of porous surfaces, the so-called quenched solid density functional theory (QSDFT), which

considers quantitatively the surface geometrical inhomogeneity in terms of a roughness parameter [17]. These DFT methods are currently widely used for the interpretation of experimental data, and the pore size distribution (PSD) calculation from adsorption isotherms is now featured in a recent standard by the International Standard Organization ISO (ISO-15901-3 2007).

To choose the best pore model for PAF-302 materials, we applied all kernels implemented in ASiQWin Quantachrome software.

As an example, we present in figure 2.10 the kernels applied to the material PAF-302: the figure shows pore distributions obtained on different surfaces (carbonaceous or zeolite / silica) and different geometries. In the inset of the figure 2.10 the relative percentage of fitting error are also reported, which indicates the percentage of deviation between the experimental isotherms and those calculated by the model used.

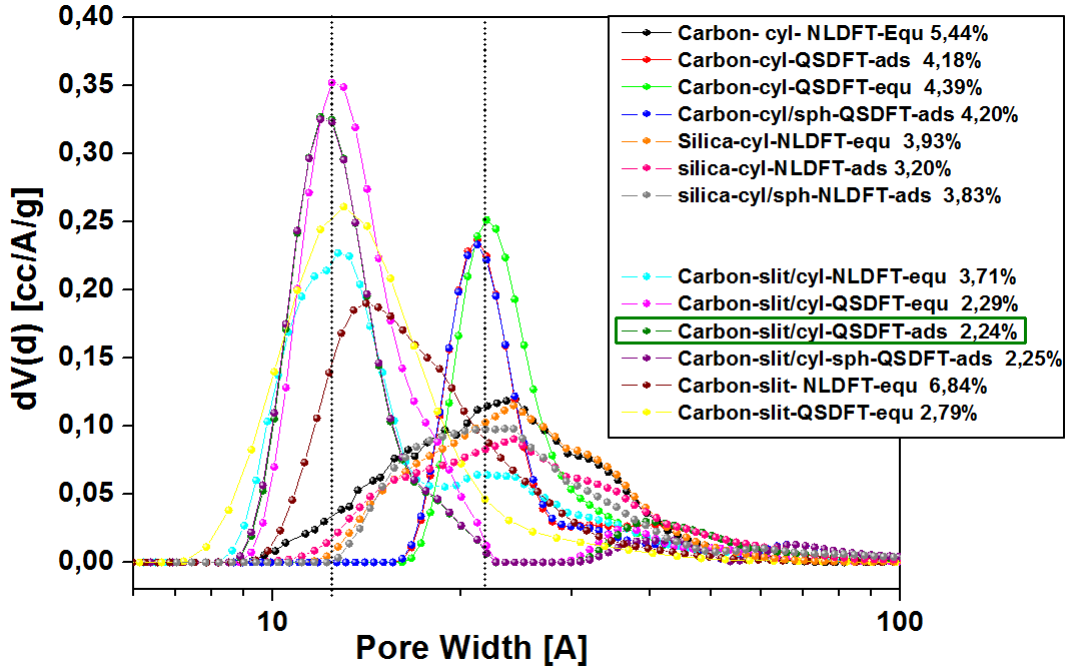

Figure 2.10. Experimental pore distributions obtained from N_2 adsorption isotherm at 77 K on PAF-302. NLDFT and QSDFT models were applied considering carbon and silica surface with different pore geometries. Inset shows the fitting error for each model

From the comparison, it follows that the lowest fitting error (2.24 %) is given by using the model QSDFT applied on carbon and with hybrid slit/cylindrical geometry. A schematic 3D molecular structure of this material is shown in figure 2.11, and from this it follows that the assumption of a cylindrical pore model seem to be realistic with regard to the main pore channels.

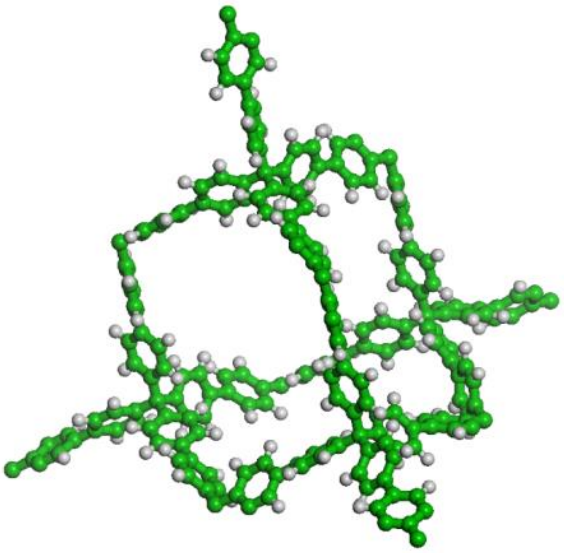

Figure 2.11. Molecular model of PAF-302 unit cell

In figure 2.9B the pore distributions of the samples PAF-302 (black spheres), PAF-302 in situ (red stars) and PAF-302-MW (blue triangles) are compared. All the samples show a narrow pore size distribution, with diameter values of 10 Å for PAF-302 in situ, 11 Å for PAF-302-MW and 12 Å for PAF-302. All materials show a small mesoporosity at 40 Å and only PAF-302 in situ sample is characterized by ultramicropores at 5.2 Å. In the table 2.2, the BET surface area, total pore volume and micropore volume of PAF-302, PAF-302-MW and PAF-302 *in situ* samples are reported.

Table 2.2: BET surface area and pore size distribution obtained from N_2 physisorption measurements at 77 K.

Sample	**BET surface area (m^2/g)**	**Total Pore Volume (cc/g)**	**Micropore Volume (cc/g)**		
			<10Å	**10<Å<20**	**Total**
PAF-302	4293	2,38	0.029	1.49	**1.52**
PAF-302 MW	2966	1.89	0.128	0.872	**1.00**
PAF-302 in situ	2200	1.69	0.36	0.41	**0.77**

PAF-302, PAF-302-MW and PAF-302 in situ are characterized by pore volume of 2.38, 1.89 and 1.69 cc/g, respectively. These pore volume values follow the trend of the surface areas of the samples. However, if we consider the total micropore volume and, in particular, the pores smaller than 10Å, the sample PAF-302 in situ shows a value of 0.36 cc/g which is much higher than that of the other materials.

2.3.2 Modification of PAF-302 surface: Functionalization with amino groups

After the optimization of the synthetic process for PAF-302, the material was functionalized by inserting amino groups in the aromatic network.

It has been demonstrated that the presence of micropores is relevant to improve the storage capacity of CO_2 at low pressure [18]. In addition, also electron-rich aromatic groups and nitrogen atoms with lone pairs have been found to be important to enhance the interaction with the CO_2 molecule.

Functionalization with amino groups of porous solid adsorbents with the aim at improving the adsorption capacity and selectivity towards the target molecule (CO_2) is a strategy that has been also applied to silica based sorbents [19], zeolites [20], and MOFs [21]. The introduction of polyamines in PAFs has revealed that the aromatic chloromethylation over the predesigned PAFs and a subsequent polyamine substitution bestowed the materials with significantly enhanced CO_2-uptake, especially at low pressures, and much lower N_2-uptake capacity [22].

Different approaches have been reported for introducing amine functionalities into the porous materials:

I. Impregnation methods with amino groups [23].
II. Post-synthesis grafting: post-functionalization of the surface using particular functional groups [22, 24, 25].
III. Introduction prior to synthesis, starting from precursors having amine functionalities [10, 21].

In this thesis work, two different methods of functionalization were used:

(I) A precursor with a protected alkyl amine functionality was synthesized, (4-Bromo-3-phtalimidomethyl)phenyl)tris(4-bromophenyl)methane). This molecule was polymerized using a modified Yamamoto reaction reported by Garibay [10]: PAF-302-CH_2-phthalimide was firstly obtained, which was subsequently deprotected to obtain PAF-302-CH_2-NH_2.

(II) Post-synthesis modification of the polymer PAF-302: plasma technique to introduce directly amine groups in the polymer was used. This is a new and easy synthetic procedure of amination of PAF-302, which is reported here for the first time for this material.

Plasma modification has become an alternative technique to wet-chemical processes for the modification of surfaces due to its many important advantages such as uniformity and reproducibility, short reaction time and environmental safety [26, 27].

One of the major limitations of plasma technology is that several functional groups are produced in the plasma: various homolytic bond fissions and ionization events, as well as secondary collisions, are in fact produced on the precursors. Subsequent molecular fragmentations, reactions, and ionization processes result in a spread of functionalities on the plasma-treated surfaces. However, the desired functionality can be obtained by tuning the discharge power.

F. Renò et al. [28] proposed a reaction mechanism of the precursor 1,2-diaminopropane (DAP) inside the plasma. In the figure 2.12 are represented the principal species (radicals), which can be produced during the plasma process.

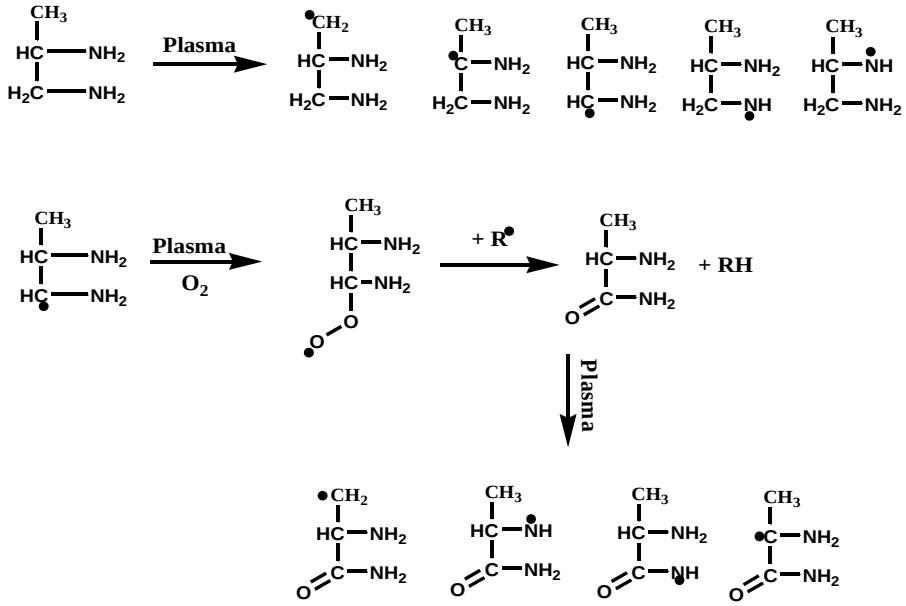

Figure 2.12. Example of reaction mechanism of DAP proposed in ref. 28. The formation of radical species, either extraction of an hydrogen atom from a primary/secondary carbon or extraction of an hydrogen atom from aminic functionality, is enlightened.

The structure, stability and porosity of the amino-functionalized PAF-302-CH_2NH_2 material was fully characterized by using Fourier transform infrared spectroscopy (FT-IR), ^{13}C solid-state NMR, PXRD analysis, thermogravimetric analysis (TGA) and N_2 physisorption at 77K; while for the sample PAF-302 plasma the characterization is still in progress: it was only possible to record FTIR, TGA and N_2 physisorption at 77K.

2.3.2.1 FTIR spectroscopy

FT-IR spectroscopy was used to investigate the structures of functionalized PAF-302 materials. The spectra of parent PAF-302 (curve a), PAF-302-CH_2NH_2 (curve b) and PAF-302 plasma (curve c) are compared in figure 2.13.

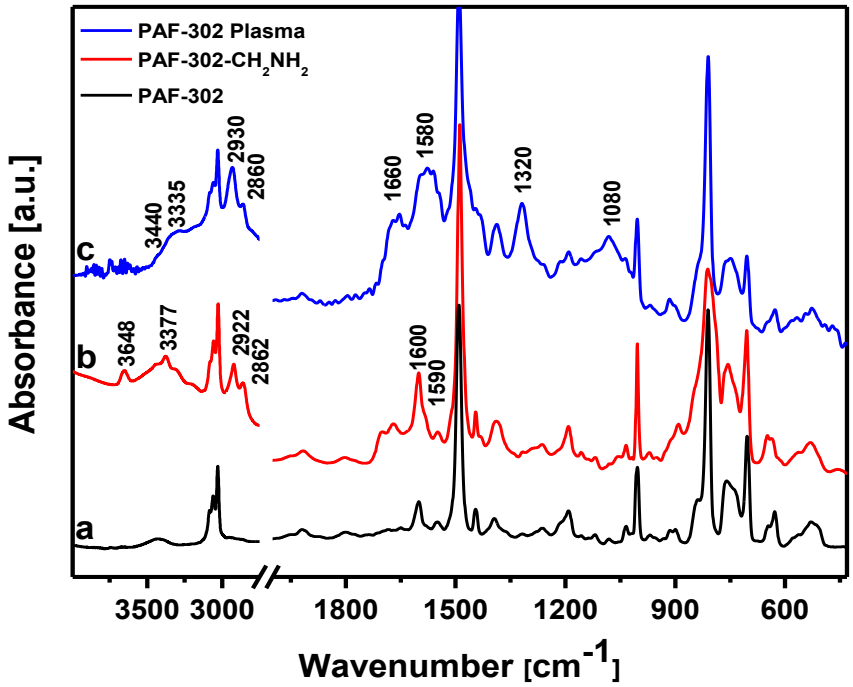

Figure 2.13. FTIR spectra of: (a) PAF-302, (b) PAF-302-CH_2NH_2 and (c) PAF-302 plasma (in KBr pellets) recorded under vacuum.

As for PAF-302, the peaks at around 1075 cm^{-1} and 600 cm^{-1}, due to the C–Br bonds (section 2.3.1.1), are almost negligible for the PAF-302-CH_2NH_2, and this confirmed that a complete polymerization occurred also for this material. As shown in the figure 2.12, the spectrum of the PAF-302-CH_2NH_2, clearly indicates the presence of $–CH_2NH_2$ functionality: at high frequencies the polymer shows a broad band in the region 3530-3270 cm^{-1} with a maximum at 3377 cm^{-1} attributed to the N-H stretching of primary amine group. The peak at 3648 cm^{-1}, assigned to a hydroxyl group, is likely due to the ethanol used to wash the material after the reduction reaction. The peaks with medium intensities at 2922 and 2862 cm^{-1} were assigned to the asymmetric and symmetric stretching of methylene groups, respectively. In the low frequency region, the band at ca. 1600 cm^{-1} due to the NH_2 bending confirms the presence of the amine groups. The peaks at 1700 and 1670 cm^{-1} with medium intensity, assigned to carbonyl stretches are due to impurities from phthalimide functionalities

probably trapped in the porous structure. Despite these impurities, FTIR spectroscopy provides clear evidence of deprotection and removal of large part of the bulky phthalimide groups.

The FT-IR spectrum of PAF-302 plasma polymer (figure 2.13c) shows in the high frequency region, a broad band with medium intensity centered at 3335 cm^{-1} with a shoulder at 3440 cm^{-1}, which are assigned to NH_2 symmetric and asymmetric stretching, respectively. The broad bands centered at about 2930 and 2860 cm^{-1} are attributed to the stretching of CH aliphatic groups: the possible radicals which can be generate by plasma include CH, CH_2 and CH_3 functionalities as shown in figure 2.12. The low frequency region is characterized by two broad bands with medium intensities centered at 1660 and 1580 cm^{-1}; the band at 1660 cm^{-1} involve C=O stretching and NH_2 deformation of amide functional group, meanwhile the band at 1580 cm^{-1} is attributed to NH_2 bending of primary amines. The peak at 1320 cm^{-1} with medium intensity, demonstrates the presence of unsaturated primary amines directly attached to aromatic rings of the polymer. From the reaction mechanism proposed literature (figure 2.12) the presence of aromatic amines is not expected; however, further investigations with other techniques are needed to confirm the presence of this group. The absorption at 1080 cm^{-1} is assigned to C-N stretching of primary aliphatic amines ($-CH_2-NH_2$). It is thus inferred that aliphatic amine and amide functionalities, deriving from homolytic bond fissions and ionization events of the precursor 1,2-diaminopropane, are present in PAF-302 plasma polymer.

2.3.2.2 Solid-state ^{13}C MAS NMR

The ^{13}C solid-state NMR (CP/MAS) measurements were preformed to study the local structures of the functionalized PAF-CH_2NH_2 (curve b) network (Figure 2.14). The spectrum of PAF-302 (curve a) is also reported for comparison. Before analysis, the PAF-CH_2NH_2 and PAF-302 were treated at 250 ° C for 5 h to remove the adsorbed solvents.

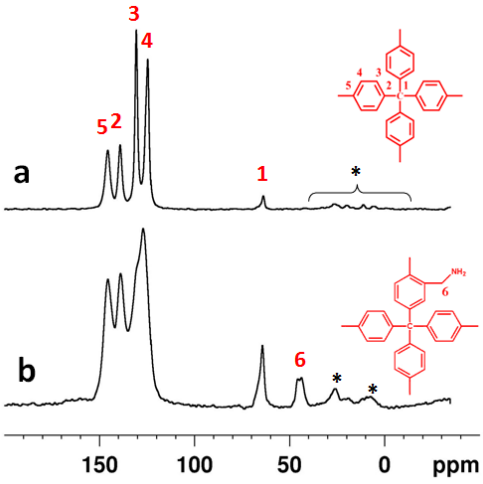

Figure 2.14. ^{13}C solid state CPMAS NMR spectra of: (a) PAF-302 and (b) PAF-302-CH_2NH_2. A cross polarization contact time of 5 ms and a MAS spin rate of 5 kHz were used in the experiment. * denotes spinning sidebands.

The solid state ^{13}C CP-MAS NMR spectrum of PAF-302–CH_2NH_2 shows in the region of aromatic carbons the peaks assigned to the phenylene groups of the framework, discussed in the section 2.3.1.2. Additionally, a corresponding peak at around 64 ppm in the structures is assigned to the quaternary carbon of TPM units. The sample PAF-302–CH_2–NH_2 compared to PAF-302, show a broad peak at 120-130 ppm overlapping different carbon atoms due to the benzylic CH_2NH_2 substitution. In the aliphatic carbon region, it can be seen a new resonance at around 46 ppm, which is assigned to the methylene groups.

The comparison between the signals of the two materials, even if they are recorded in the same condition (5 ms), shows that the sample PAF-302–CH_2NH_2 is characterized by an intense peak for the tetrahedral carbon. This can be explained by the efficiency of the magnetization transfer that depends on the flexibility of the frameworks: when the framework is more flexible, the transfer is less efficient and leads to lower peak intensity; in the case of PAF-302-CH_2NH_2 sample, probably the functionalization leads to greater rigidity of the network and thus to a more intense peak.

2.3.2.3 Thermogravimetric analysis (TGA)

Thermogravimetric analysis (TGA) under argon atmosphere (Figure 2.15) was performed to study the thermal stability of PAF-302-CH_2NH_2 (curve b) and PAF-302 plasma (curve c), compared with PAF-302 (curve a).

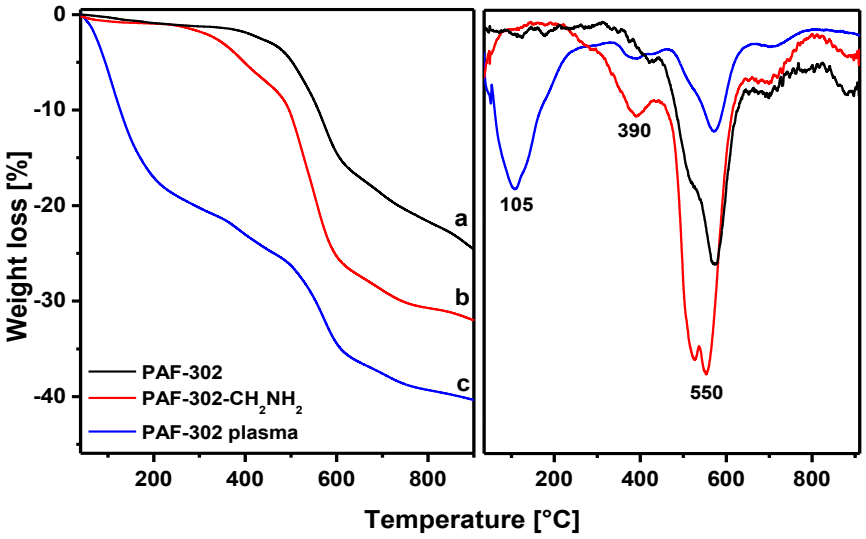

Figure 2.15. TGA plots of (a) PAF-302, (b) PAF-302-CH_2NH_2 and (c) PAF-302 plasma samples, obtained at 2 °C/min under Argon atmosphere up to a maximum temperature of 900 °C

The TGA of PAF-302-CH_2NH_2 (Figure 2.15 curve b) shows mainly two weight losses: the first at 390°C of about 7.5% is assigned to the decomposition of methylene amine functionalities, and the second, which begins at around 450°C, is due the decomposition of the framework. The sample PAF-302 plasma shows more weight losses. As noted before, the introduction of new functionalities in the polymer using plasma process leads to different functionalizations which includes not only the amine groups but also alkylamines and amides. The first weight loss of about 16%, centered at 105°C may be due to the alkylamine groups trapped in the pore system. The second weight loss of 5% is centered at a temperature of 390 °C could be due to alkylamine groups covalently linked to the framework. Finally, the weight loss beginning at 450°C indicates the start of the decomposition of the framework.

2.3.2.4 PXRD measurements

To investigate the crystallinity of the functionalized PAF-302 samples, powder X-ray diffraction (PXRD) was performed (Figure 2.16).

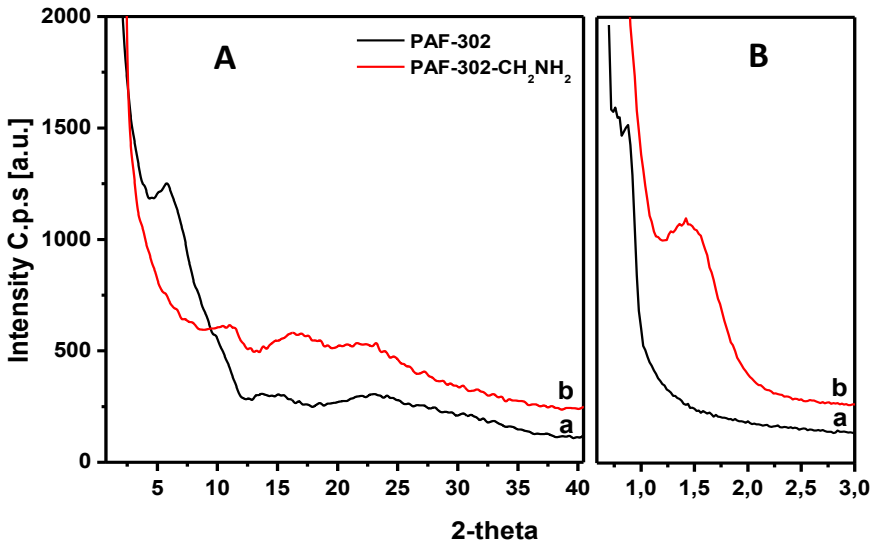

Figure 2.16 PXRD patterns of PAF-302 (a) and PAF-302-CH_2NH_2 (b) samples.

The PXRD pattern of the sample PAF-302-CH_2NH_2 shows an amorphous texture. Compared to PAF-302, PAF-302-CH_2NH_2 sample is characterized by the absence of the peak at~ 5 2-theta and the appearance of a new band at low angles at about 1,5 2-theta (figure 2.16 B). These variations are due to the structural change induced by functionalization.

2.3.2.5 N_2 physisorption measurements

In order to characterize the porosity of the frameworks, nitrogen adsorption–desorption isotherms at 77K were obtained, and the Brunauer–Emmett–Teller (BET) surface areas of the polymers were calculated as well as pore volume and distribution. Before analysis, the samples were treated at 250 ° C for 18 h to remove the adsorbed solvents.

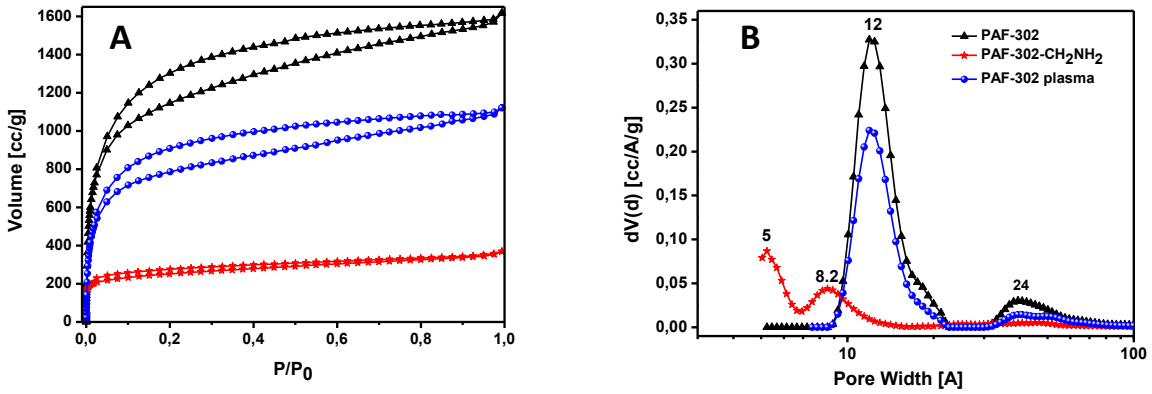

Figure 2.17. (A) N_2 adsorption-desorption isotherms at 77K and relative pressures (P/P0) from $1x10^{-7}$ to 1 and (B) pore size distribution determined by QSDFT methods of PAF-302 (black triangles), PAF-302CH_2NH_2 (red stars) and PAF-302 plasma (blue spheres)

As shown in Figure 2.17, the functionalized polymers displayed a Type I shape in the adsorption branch with high gas uptake at low pressures which is a signature feature of microporous materials. PAF-302 plasma, similarly to PAF-302, shows a H1-type hysteresis loops in the desorption branch, whereas PAF-302-CH_2NH_2, shows a very small hysteresis loop. The apparent surface areas calculated from the BET model for P/P_0 between 0,012 and 0,13 were 2980 m^2 g^{-1} and 923 m^2 g^{-1} for PAF-302 plasma and PAF-302-CH_2HN_2 respectively. The data of surface area and porosity of the materials are shown in table 2.3.

Pore size distribution curves for the functionalized PAF-302 materials were determined from appropriately fitting density functional theory (DFT) models. As for PAF-302, the lowest fitting error is obtained by the QSDFT model applied on carbon surfaces with hybrid slit/cylindrical geometry.

Based on the pore distributions, the average pore size for PAF-302 plasma is about 12Å, similar to PAF-302. The total pore volume is 1.57 cc/g with a total micropore volume of 1.02 cc/g. The decrease of the total pore volume is in accordance with the decrease of the surface area. The pore distribution is not much changed by the functionalization with plasma, which means that the functionalization of the pores of the material was limited, and that it occurred essentially on the external surface.

PAF-302-CH_2NH_2 instead shows very different pore size distribution (figure 2.17 B): the typical mesopores at 12 and 24 Å of PAF-302 are in fact absent in this sample, which displays small micropores of 8 Å and ultramicropores of 5 Å. The total pore volume is 0.51 cc/g while its micropore volume is 0.275 cc/g. The large amount of pores with diameter <10 Å, ten times higher than the PAF-302, is however very promising for its gas uptake capacity at low pressure.

Table 2.3. BET surface area and pore size distribution obtained from N_2 physisorption measurements at 77 K.

Sample	BET surface area (m^2/g)	Total Pore Volume (cc/g)	Micropore Volume (cc/g)		
			<10Å	**10<Å<20**	**Total**
PAF-302	4293	2,38	0.029	1.49	**1.52**
PAF-302-CH_2NH_2	923	0.51	0.22	0.055	**0.275**
PAF-302 plasma	2980	1.57	0.022	0.997	**1.02**

2.3.3 Methane Adsorption on PAF-302: FTIR and Theoretical Combined Studies

Since the proposed applications of PAF-302 material for methane storage and transportation are very promising, an extensive study of the methane/PAF-302 interactions was performed. In this context, FT-IR spectroscopy was employed, along with ab initio calculations, to describe the vibrational features of PAF-302 material (discussed in section 2.3.1.1) and the interactions of methane with the surface of the porous framework. The CH_4 loading (i.e. the CH_4 pressure) was varied during the experiment to get some hints on the strength of the interactions. The complete discussion is published in the ref. 11, here a summary of the study is provided.

Adsorbed methane modes depend on the type of interactions between adsorbate-adsorbent, which are connected with the chemistry of the framework. In the literature, FTIR studies on the adsorption of CH_4 in different materials are reported: in systems such as zeolites [29] and oxides [30] the polarization of the methane molecules is primarily due to strong electric fields such as ionic sites, acidic and basic sites. In other adsorbents, such as silica and alumina, the adsorbed methane interacts with the surface hydroxyls [31, 32]. Thus, in these cases, dipolar interactions and hydrogen bonds are involved. On the other hand, for carbon-based adsorbents [33, 34] like PAF-302 only van der Waals interactions can be envisaged.

The methane/PAF system was studied by considering the possible local symmetry of methane molecules interacting with the porous network. PAF-302 polymer is characterized by a 3D structure where methane can interact simultaneously with faces and edges of phenyl rings, and monodentate (local C_{3v} symmetry) and bidentate (local C_{2v} symmetry) configurations of methane molecules are possible. Figure 2.18 shows the theoretical stretching and bending harmonic frequencies of free CH_4 (T_d symmetry), p-xylene - methane (C_{3v} symmetry) and di-tolylmethane - methane (C_{2v} symmetry) structures: after the adsorption of methane the forbidden modes (that would be normally detected only by Raman spectroscopy) may become observable in the infrared spectra because of surface interactions.

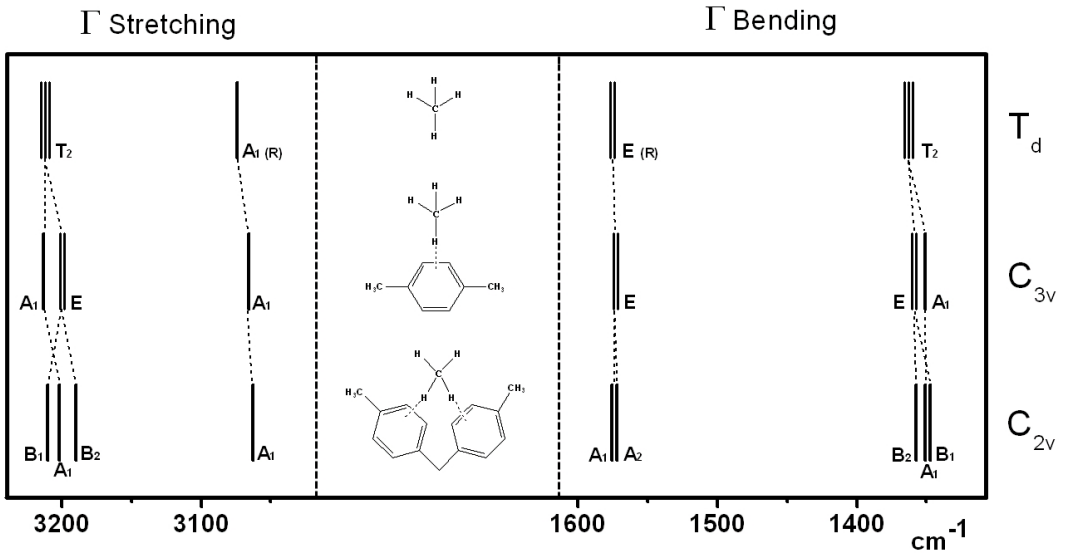

Figure 2.18. Representation of the theoretical stretching and bending harmonic frequencies of free CH_4 (T_d symmetry) p-xylene - methane (C_{3v} symmetry) and di-tolylmethane - methane (C_{2v} symmetry) structures. The normal modes of vibration are classified on the basis of the T_d point group to which the adsorbed methane belongs.

FTIR spectra were recorded after adsorbing different CH_4 loadings. They were resolved by comparison with the spectra of adsorbed CD_4, and with the help of theoretical calculations on model systems, such as methane interacting with p-xylene and with di-tolylmethane in "pseudo" C_{3v} and C_{2v} local symmetry respectively. The use of these simplified models, studied at ab initio level, greatly supported the experimental analysis. Difference spectra after gas adsorption on PAF-302 were examined (figure 2.19), in order to reveal bands of adsorbed methane (or deuterated methane) possibly masked by the structural bands of the material. The experimental vibrational frequencies of free methane and adsorbed methane are reported in Table 2.4, where the case of deuterated methane is also considered.

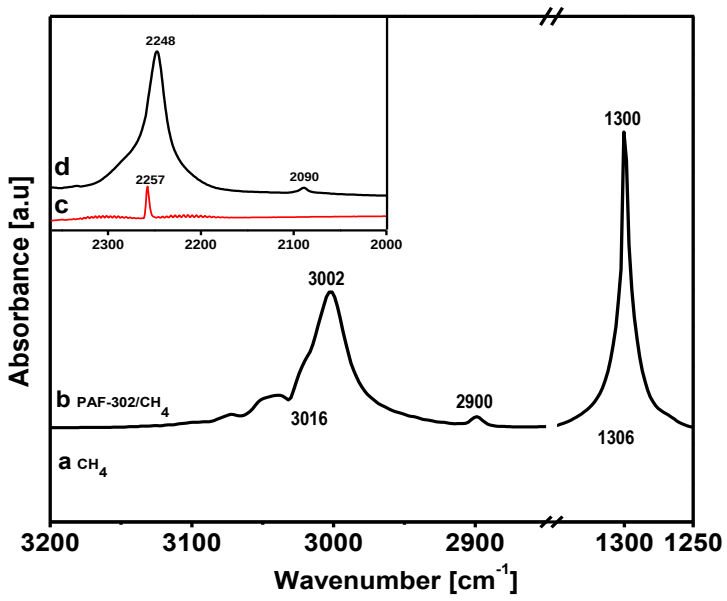

Figure 2.19. IR spectra of: (a) CH_4 gas, (b) difference spectrum obtained after subtracting that of the bare sample. In the inset are reported: (c) CD_4 gas, (d) difference spectrum at equilibrium pressure of 7 mbar CD_4.

Table 2.4. IR frequencies and shifts upon CH_4 and CD_4 adsorption on PAF-302 .

mode	CH_4 (gas) [cm^{-1}]	CH_4 (ads.) [cm^{-1}]	Shift, $\Delta\nu$/ cm^{-1}	CD_4 (gas) [cm^{-1}]	CD_4 (ads.) [cm^{-1}]	Shift, $\Delta\nu$/ cm^{-1}
ν_1 (A_1)	2917[a] (*R*)	2900	-17	2101[a] (*R*)	2090	-11
ν_2 (E)	1533[a] (*R*)	b	-	1090[a] (*R*)	b	-
ν_3 (T_2)	3016 (*IR*)	3002	-14	2257 (*IR*)	2248	- 9
ν_4 (T_2)	1306 (*IR*)	1300	-6	995 (*IR*)	990	-5

[a] Ref. 35; [b] Not detected because masked by PAF-302 structural vibrations.

The very intense band at 3002 cm^{-1} with a shoulder at higher wavenumber is assigned to the ν_3 stretching mode of adsorbed CH_4 shifted of 14 cm^{-1} with respect to the vibration at 3016 cm^{-1} in the methane gas (figure 2.19, curve b): this vibrational mode is triply degenerated in gaseous methane, while the degeneration is removed when the interactions with the surface lower the symmetry, in agreement with the broad and asymmetric band observed in the spectrum of adsorbed methane. The calculated shifts are -12 and -22 cm^{-1} for "pseudo" C_{3v} and C_{2v} complexes, respectively. This accounts for the very broad band found in the experimental spectrum, which is probably formed by several unresolved components whose nature cannot be precisely identified. However, it is likely that either monodentated or bidentate adducts can be formed upon adsorption of methane on PAF302, notwithstanding other host-guest interactions are also possible as described in figure 2.20.

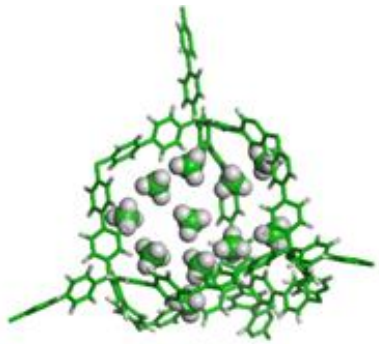

Figure 2.20. A model of PAF-302 crystalline structure with a number of adsorbed CH_4 molecules, to illustrate the variety of possible positions inside the porous material.

The symmetric stretching (v_1) mode, which becomes IR active after the interaction with the PAF-302 framework, is characterized by a weak band at 2900 cm^{-1}: the corresponding frequency in the free molecule, visible in the Raman spectrum of gaseous methane, falls at 2917 cm^{-1} [35]. Upon adsorption the v_1 mode is shifted by -17 cm^{-1}, in comparison to the theoretical shifts of -8 and -11 cm^{-1} for interactions with one or two aromatic rings, respectively. Also considering the errors due to the harmonic approximation in the theoretical results (strongly reduced when frequency *shifts* are computed, anyway), the measured v_1 shift indicates a strong interaction of methane with PAF-302 aromatic moieties, apparently with more than two phenyl rings affecting this vibration mode.

Finally, in the low frequency region the v_4 bending mode at 1306 cm^{-1} is shifted of -6 cm^{-1} with respect to free CH_4 gas. Because the deformation modes are normally less perturbed when the molecule is adsorbed, this result is consistent with the PAF/CH_4 interactions previously described.

In conclusion, a simple model based on the symmetry reduction passing from gaseous to adsorbed methane allowed to predict the structure of the vibrational bands upon adsorption: the calculations on the molecular models provided an estimate of the expected frequency shifts. On the basis of these results, the spectra recorded after adsorption indicate multiple interactions between methane and PAF surface, where one or two phenyl rings (i.e. monodentate or bidentate adducts, respectively) are involved.

2.4 Conclusions

In this chapter, the synthesis and characterization of PAF-302 and amino-functionalized PAF-302 samples were reported.

The physico-chemical properties have been studied by a combination of different experimental techniques such as SS-MAS NMR and FTIR spectroscopies, X-ray diffraction, N_2 physisorption measurements and TGA analysis.

The synthetic procedure reported in the literature [1] for PAF-302 sample was modified in our laboratory. The material is characterized by high stability and high porosity (surface area and total pore volume of 4293 m^2/g and 2,38 cc/g, respectively).

Beside the traditional synthesis to prepare PAF-302 material, two novel synthetic routes were optimized: i) synthesis assisted by microwave and ii) synthesis with $Ni(COD)_2$ made directly in situ. These materials showed very similar framework structure of PAF-302 but with low surface area. However, if we consider the pores smaller than 10Å, which are the optimum for the storage of H_2 and CO_2, the sample PAF-302 in situ shows a value of 0.36 cc/g much higher than those of the other two materials synthesized in this thesis.
In order to improve gas storage adsorption and in particular CO_2 adsorption, functionalization of PAF-302 with amino groups were made using both wet synthesis starting from amine functionalized precursor and post-synthesis treatment in which amino groups were introduced using a plasma technique obtaining two new materials named PAF-302-CH_2NH_2 and PAF-302 plasma, respectively. These materials are characterized by lower surface area and pore volume in comparison to the parent PAF-302; the pore distribution of PAF-302 plasma is, however, similar to PAF-302 with pore size at 12Å, whereas PAF-302-CH_2NH_2 shows very different pore size distribution characterized by small micropores of 8 Å and ultramicropores of 5 Å. Beside the very small pores, this sample is also characterized by micropore volume of 0.275 cc/g, which is ten times higher than the PAF-302.

All the samples synthesized are characterized by good thermal and chemical stability that, together with the high surface area and pore volume (especially microporous) make these samples good candidates for gas storage. In the chapter 4, their storage capacity of CO_2, H_2 and CH_4 in different conditions of temperature and pressure will be discussed.

Finally, experimental FTIR spectroscopy combined with computational calculations were used to investigate the structure of PAF-302 before and after adsorption of CH_4: on the basis of the obtained results, multiple interactions between methane and PAF surface, where one or two phenyl rings (i.e. monodentate or bidentate adducts, respectively) are involved.

References:

[1] Ben, T.; Ren, H.; Ma, S.; Cao, D.; Lan, J.; Jing, X.; Wang, W.; Xu, J.; Deng, F.; Simmons, J. M.; Qiu, S.; Zhu, G. Targeted Synthesis of a Porous Aromatic Framework With High Stability and Exceptionally High Surface Area. *Angew. Chem., Int. Ed.* **2009**, *48*, 9457-9460.

[2] Semmelhack, M. F.; Helquist, P.; Jones, L. D.; Keller, L.; Mendelson, L.; Ryono, L. S.; Smith, J. G., Stauffer, R. D. Reaction of Aryl and Vinyl Halides with Zerovalent Nickel-Preparative Aspects and the Synthesis of Alnusone. *Journal american chemistry society* **1981**, 103, 6460-6471.

[3] Yamamoto, T.; Wakabayashi, S.; Osakada, K. Mechanism of C-C coupling reactions of aromatic halides, promoted by $Ni(COD)_2$ in the presence of 2,2'-bipyridine and PPh3, to give biaryls. *Journal of Organometallic Chemistry* **1992**, 428, 223-237.

[4] T. Ben and S. Qiu, Porous aromatic frameworks: Synthesis, structure and functions. *Cryst Eng Comm* **2013**, 15, 17-26.

[5] Yamamoto, T.; Fukuda, T.; Begum, F.; Ikeda, T.; Sasaki, S.; Takezoe, H.; Kubotall, K. Pi-conjuygated Poly(pyridine-2,5-diyl), Poly(2,2'-bipyridine-5,5'-diyl), and their alkyl derivatives. Preparation, Linear structures, Function as a ligand into form their transition metal complexes, catalytic reactions, n-type electrically conducting prope. *Journal american chemistry society* **1994**, 116, 4832-4845.

[6] Galand, E. M. Processable Variable Band Gap Conjugated Polymers For Optoelctronic Devices. University of Florida, **2006**.

[7] Trewin, A.; Cooper, A. I. Porous Organic Polymers : Distinction from Disorder?. *Angew. Chem. Int . Ed.* **2010**, 49, 1533 – 1535.

[8] Wilson, L. M., Griffin, A. C. Synthesis of molecular "jacks": rigid tetrahedral molecules with p-phenylene arms. *Journal of Materials Chemistry* **1993**, 3, 991-994.

[9] Krysan, D. J.; Mackenzie, P.B. A new convenient preparation of Bis(1,5-cyclooctadiene)nickel(0). *J. Org. Chem.* **1990**, 55, 4229-4230.

[10] Garibay, S. J.; Weston, M. H.; Mondloch, J. E.; Colon, Y. J.; Farha, O. K.; Hupp, J. T.; Nguyen., S. T. Accessing functionalized porous aromatic frameworks (PAFs) through a de novo approach.*CrystEngComm* **2013**, 15, 1515 −1519.

[11] Errahali, M.; Gatti, G.; Tei, L.; Canti, L.; Fraccarollo, A.; Cossi, M.; Marchese, L. Understanding Methane Adsorption in Porous Aromatic Frameworks: An FTIR, Raman, and Theoretical Combined Study. *J. Phys. Chem C,* **2014**, *118*, 10053-10060.

[12] Socrates, G. *Infrared and Raman Characteristic Group Frequencies: Tables and Charts.* 3rd Edition. John Wiley & Sons Inc: New York , **2004**; 157-161.

[13] Colthup, N.B.; Daly, L.H.; Wiberley, S.E. *Introduction to Infrared and Raman Spectroscopy. Introduction to Infrared and Raman Spectroscopy*. Academic Press: New York, **1964**; 261-280.

[14] Ben, T.; Pei, C.; Zhang, D.; Xu, J.; Deng, F.; Jing, X.; Qiu, S. Gas Storage in Porous Aromatic frameworks (PAFs). *Energy Environ. Sci.* **2011**, *4*, 3991-3999.

[15] Lowell, S.; Shields, J. E.; Thomas, M. A.; Thommes, A. *Characterization of Porous Solids and Powders: Surface Area, Pore Size and Density*; Kluwer Academic Publishers: Dordrecht, NL, **2004**.

[16] Ravikovitch, P.I.; Vishnyakov, A.; Russo, R.; Neimark, A.V. Unified approach to pore size characterization of microporous carbonaceous materials from N_2, Ar, and CO_2 adsorption isotherms. *Langmuir* **2000**, 16, 2311–2320.

[17] Neimark, A.V.; Ravikovitch, P.I.; Lin, Y.; Thommes, M. Quenched solid density functional theory and pore size analysis of micromesoporous carbons. *Carbon* **2009**, 47, 1617.

[18] Sevilla,M.; Falco, C.; Titirici, M.-M.; Fuertes, A. B. High-performance CO_2 sorbents from algae. *RSC Adv*. **2012**, 2, 12792-97.

[19] Knowles, G.P.; Graham, J.V.; Delany, S.W.; Chaffee, A.L.. Aminopropyl-Functionalized Mesoporous Silicas as CO_2 Adsorbents. *Fuel Process. Technol* **2005**, 86, 1435-1448.

[20] Chatti, R.; Bansiwal, A.K.; Thote, J.A.; Kumar, V.; Jadhav, P.; Lokhande, S.K.; Biniwale, R.B.; Labhsetwar, K.N.; Rayalu, S.S. Amine Loaded Zeolites for Carbon Dioxide Capture: Amine loading and adsorption studies. *Micropor. Mesopor. Mater* **2009**, 121: 84-89.

[21] Ahnfeldt, T.; Gunzelmann, D.; Loiseau, T.; Hirsemann, D.; Senken, J.; Ferey, G.; Stock, N. Synthesis and Modification of a functionalized 3D Open-Framework Structure with MIL-53 Topology. *J. Am. Chem. Soc* **2009**, 48, 3057-3064.

[22] Lu, W.; Sculley, J. P.; Yuan, D.; Krishna, R.; Wei, Z.; Zhou, H.-C. Polyamine-tethered porous polymer networks for carbon dioxide capture from flue gas. *Angew. Chem., Int. Ed.* **2012**, 51, 7480-4.

[23] Pevida, C.; Plaza, M.G.; Arias, B.; Fermoso, J.; Rubiera, F.; Pis, J.J. Surface Modification of Activated Carbons for CO_2 Capture. *Appl. Surf. Sci* **2008**, 254, 7165-7172.

[24] Serna-Guerrero, R.; Belmabkhoutb, Y.; Sayari, A. Further investigations of CO_2 capture using triamine-grafted pore-expanded mesoporous silica. *Chemical Engineering Journal* **2010**, 158, 513-519.

[25] Wang, X. R.; Li, H. Q.; Liu, H.T.; Hou, X.J. As-synthesized mesoporous silica MSU-1 modified with tetraethylenepentamine for CO_2 adsorption. *Microporous & Mesoporous Materials* **2011**, 142, 564-569.

[26] Mutlu, S.; Çökeliler, D.; Mutlu, M. Modification of food contacting surfaces by plasma polymerization technique. Part II: Static and dynamic adsorption behavior of a model protein ‘‘bovine serum albumin’’ on stainless steel surface. *J. Food Eng.* **2007**, 78, 494-499.

[27] Siow, K. S.; Britcher, L.; Kumar, S.; Griesser, H. J. Plasma Methods for the Generation of Chemically Reactive Surfaces for Biomolecule Immobilization and Cell Colonization - A Review. *Plasma Process. Polym*. **2006**, 3, 392–418.

[28] Reno`, F.; D’Angelo, D.; Gottardi, G.; Rizzi, M.; Aragno, D.; Piacenza, G.; Cartasegna, F.; Biasizzo, M.; Trotta, F.; Cannas, M. Atmospheric Pressure Plasma Surface Modification of Poly(D,L-lactic acid) Increases

Fibroblast, Osteoblast and Keratinocyte Adhesion and Proliferation. *Plasma Process. Polym.* **2012**, 9, 491–502.

[29] Yamazaki, T.; Watanuki, I.; Ozawa, S and Ogino, Y. Infrared Spectra of Methane Adsorbed by Ion-Exchanged ZSM-5 Zeolites. *Langmuir* **1988**, 4, 433-43.

[30] Li, C.; Li, G. and Xin, Q. FT-IR Spectroscopic Studies of Methane Adsorption on Magnesium Oxide. *J. Phys. Chem.* **1994**, 98, 1933-1938.

[31] Chen, L.; Lin, L.; Xu, Z.; Zhang, T. and Liang, D. Interaction of methane with surfaces of silica, aluminas and HZSM-5 zeolite. A comparative FT-IR study. *Catalysis Letters* **1995**, 35, 245-258.

[32] Kishima, M.; Okubo, T. Characterization of Microporous Titanosilicate ETS-10 by Infrared Spectroscopy with Methane as a Probe Molecule for Basic Sites. *J. Phys. Chem. B* **2003**,107,8462-8468.

[33] Yoshida, H.; Yamazaki, T. and Ozawa, S. IR Spectra of CH_4 Physisorbed on an Active Carbon at Low Temperature. *Journal of Colloid and Interface Science* **2000**, 224,261–264.

[34] Lubezky, A.; Chechelnitsky, L. and Folman, M. IR spectra of CH_4 , CD_4 , C_2H_4 , C_2H_2, CH_3OH and CH_3OD adsorbed on C_{60} films. *J. Chem. SOC., Faraday Trans.***1996**, 92, 2269-2274.

[35] Shimanouchi, T. *Tables of Molecular Vibrational Frequencies*, Consolidated Volume I: National Standard Reference Data Series; National Bureau Of Standards: Washington DC, **1972**; Vol. 39; 45-47.

CHAPTER 3

Microporous hyper-crosslinked aromatic polymers: synthesis, characterization and functionalization with amino groups

3.1 Introduction

Hyper-Crosslinked Polymers (HCPs) are a class of low cost porous organic networks easily prepared by Friedel–Crafts reaction. The permanent porosity in HCPs is a result of extensive crosslinking reactions of aromatic residues, which prevents the polymer chains from collapsing into a dense, nonporous state [1]. The extensive crosslinked nature of the materials confers them high thermal stability that is not commonly expected for organic polymers. The stability, combined with high surface areas and simple, cost-effective and easy to scale-up preparation, make HCPs highly promising materials for fuel gas storage (methane and hydrogen) and carbon dioxide capture applications [2].

The Friedel-Crafts reaction is relevant both in fundamental research and industrial application, so it is considered be a hotspot in the research from its birth to the present. This reaction is catalysed by Lewis acids (such as $FeCl_3$, $AlCl_3$...etc.), and represents a versatile route that avoids the need for monomers with specific polymerizable functionalities. In addition, it requires mild conditions without any expensive materials and catalysts, offering an economical and an easier approach for the synthesis of a variety of porous polymers [3,4]. Recently, a new method for preparing microporous polymers by using formaldehyde dimethyl acetal (FDA) as crosslinking agent to polymerize various aromatic monomers has been reported [5]. During their extensive research on organic materials, Cooper and co-workers applied this approach to the polymerization of the rigid aromatic structure of tetraphenylmethane (TPM) obtaining materials with good CO_2 storage properties [6]. Herein, we apply the Friedel–Crafts reaction using formaldehyde dimethyl acetal (FDA) to crosslink various tetrahedral aromatic monomers in order to get different microporous polymers.

A proposed reaction mechanism concerning the use of the FDA linker agent is reported in figure 3.1:

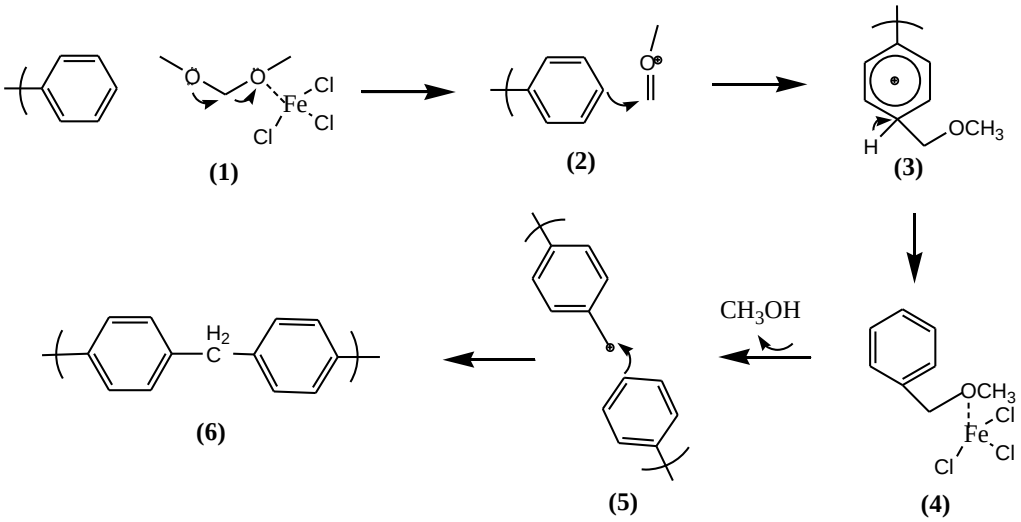

Figure 3.1. The mechanism of the Friedel-Crafts reaction in the presence of FDA linker.

Step I: Lewis acid attack the FDA with the formation of an oxocarbenium ion (1).

Step II: Electrophilic aromatic substitution reaction between the intermediate (1) and the aromatic ring results in the formation of a resonance stabilized carbocation (2). The carbocation intermediate loses a proton and the aromaticity is restored.

Step III: the resulting ether undergoes rapid cleavage with iron chloride to give methanol and the carbocation intermediate (5), which undergoes a further electrophilic aromatic substitution generating a methylene bridge between two aromatic rings (6).

In addition to the main coupling mechanism other side reactions due to the presence of excess of Lewis acid and FDA are possible (figure 3.2):

1) Formation of the chloro-methylene substituents

2) Acid hydrolysis of the methoxy group with the formation of the hydroxyl-methylene substituent group.

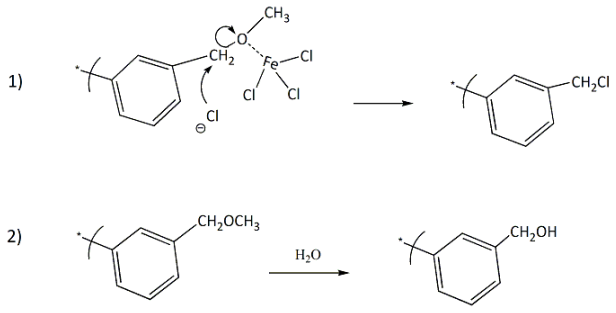

Figure 3.2. Reaction mechanism for the side products formed during the synthesis of the HCP polymers by Friedel–Crafts reaction.

This chapter describes the optimization of the synthetic processes that make use of different tetrahedral aromatic monomers to obtain high surface areas and high microporsity. In this context, the research work was focused on:

1. The optimization of the Friedel-Crafts synthetic conditions: the ratio between the monomer TPM and the linker FDA was changed in order to optimize the porous properties of the polymers. The polymers were named mPAF-1/n, as *micro*porous aromatic framework, where n indicate the TPM/FDA ratio used in the synthesis;
2. The mPAF-1/n polymer with the highest surface area and ultramicropore volume was further optimized, in terms of porosity and gas storage capacity, using two different methods: (I) thermal treatment under different conditions, and (II) functionalization with different amine groups.
3. The synthesis of HCP polymers using aromatic precursors with different tetrahedral centres, in particular tetraphenyladamantane (TPA), tetraphenylethane (TPEa), tetraphenylethylene (TPE), tetraphenylsilane (TPS) and tetraphenyltin (TPT) was also tempted and the properties of the resulting polymers were studied.
4. A preliminary study on further optimization of the HCP synthesis, where both the effect of the amount of solvent (i.e. precursors concentration) and the heat treatment after synthesis, on the porosity of the polymers synthesized, were described.

A comparative investigation of the physico-chemical properties of the prepared polymers was carried out using elemental analysis, FTIR, SS-NMR, PXRD, TGA and N_2 physisorption at 77K.

3.2 Experimental

3.2.1 Standard procedure for the synthesis of mPAF materials with different TPM:FDA ratio. In a typical procedure, ferric chloride (0.16 mol) and tetraphenylmethane (TPM 0.01 mol) were suspended in dichloroethane (DCE, 240 mL). The resulting mixture was stirred vigorously at room temperature to obtain a homogeneous solution. Then, formaldehyde dimethylacetal (FDA 0.16 mol) was added dropwise. The resulting thick gel was stirred at room temperature for 4h and then heated under reflux overnight. During the polymerization, the networks precipitated from solution as a brown solid. After cooling to room temperature, the gel was diluted with methanol and washed several times with water until the pH become neutral, and finally dried in oven at 100 °C overnight. In addition, the reaction was carried out changing the TPM:FDA ratio (1:3, 1:9 and 1:30). At higher TPM:FDA ratio, macroscopic gelation of solutions was observed immediately after FDA addition then evolving quickly in extremely thick phase (65-96 % yields). All mPAF-1/n (n ranges 3 to 30, as stated above) materials are totally insoluble in all solvents tested (water and common organic solvents) and exhibited good chemical stability to strongly acidic and basic conditions (37% HCl, saturated aqueous NH_4OH). The elemental analysis of the polymers is reported in table 3.1:

Table 3.1. Elemental analysis and EDX of the mPAF materials

Material	TPM/FDA	Elemental analysis (%)		EDX analysis (%)		
		C	H	Cl	O	Fe
mPAF-1/3	1:3	85.47	5.23	1.64	4.63	0.45
mPAF-1/9	1:9	78.28	4.91	2.16	6.78	0.11
mPAF-1/16	1:16	78.78	4.84	1.80	8.30	0.08
mPAF-1/30	1:30	78.54	4.95	1.66	9.08	0.13

3.2.2 Post-synthetic temperature treatments of mPAF-1/16

mPAF-1/16@*380.* 1.0 g of mPAF-1/16 material was placed in an alumina crucible and heated at a temperature of 380 °C for 16 h with a heating rate of 2 °C/min under nitrogen flow. (0,8 g, 80% yield)

mPAF-1/16@*800-KOH.* 1.0 g of mPAF-1/16 material was homogeneously grinded with 3g of KOH. The mixture was kept in the air for 5 h to make sure that the KOH moisture enters into the porosity of the material and acts not only as activating agent but also as a templating agent to prevent the collapse of the porosity. The mixture was placed in a crucible of alumina and calcinated at a temperature of 800 °C for 2 h with a heating rate of 2 °C/min under nitrogen flow. (0,47g, 48% yield)

3.2.3 Post-synthetic amination of mPAF-1/16

mPAF-1/16-*$NHCH_3$.* 0.8 g of mPAF-1/16 sample was swelled in 75 ml of benzene and stirred for 48h at 298K. Then, the mixture was centrifuged and benzene surnatant was removed from the container. The material was placed in a schlenk tube and a 2.0 M solution of methylamine in THF (11 ml) was added and kept under stirring for 1 night at 35°C. The mixture was filtered and washed with water until a neutral pH. Finally, the sample was extracted with methanol for one night in a soxhlet. The final product was placed in an oven at 120°C for 48h (0,789 g, 93% yield).

mPAF-1/16-*$N(CH_2CH_3)_2$.* 0.8 g of mPAF-1/16 sample was swelled in 75 ml of benzene and stirred for 48h. Then, the mixture was centrifuged and benzene surnatant was removed before adding a solution of diethylamine 99.5 % (11 ml). The mixture was placed in a schlenk tube and kept under stirring for 1 night at 35°C . The mixture was filtered and washed with water until neutral pH. The sample was washed in soxhlet by refluxing in methanol for one night. The final product was placed in an oven at 120°C for 48h (0,77 g, 90 % yield).

mPAF-1/16-*TETA*. An autoclave was charged with mPAF-1/16 (0,2 g) and triethylenetetramine (TETA, 20 mL). The autoclave was sealed and heated to 90°C for 3 days. The resulting solid was collected, washed with water and methanol, and then dried in vacuum to produce mPAF-1/16-TETA as a brown powder (0,11g, 45,8 % yield).

3.2.4 Synthesis of mPAF materials with different tetrahedral monomers. The same synthetic procedure, reported for mPAF-1/n polymers was used on the precursors tetraphenylsilane, tetraphenyltin, tetraphenyladamantane, tetraphenylethane and tetraphenylethene. The precursor structures are reported in figure 3.3.

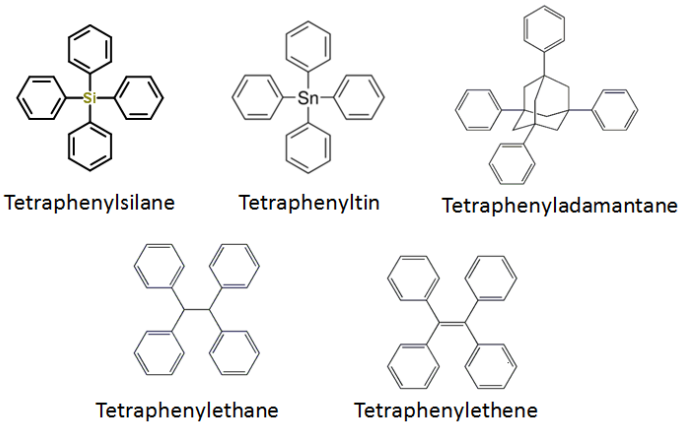

Figure 3.3. Tetrahedral precursors used for the synthesis of new HCP polymers

Tetraphenylsilane, tetraphenyltin, tetraphenylethane and tetraphenylethene were purched from Sigma-aldrich and used without purification, while tetraphenyladamantane precursor was prepared from ref 7.

In a typical procedure, ferric chloride (0.16 mol) and the polymer precursor (0.01 mol) were suspended in dichloroethane (DCE, 240 mL). The resulting mixture was stirred vigorously at room temperature to obtain a homogeneous solution. Then, formaldehyde dimethylacetal (FDA 0.16 mol) was added dropwise. The resulting thick gel was stirred at room temperature for 4h and then heated under reflux overnight. After cooling to room temperature, the gel was diluted with methanol and washed several times with water until the pH become neutral, and finally dried in oven at 100 °C overnight. The polymer networks were obtained in quantitative yields as dark brown, powdery solids (55 - 98 % yields). The samples used for characterization were activated under vacuum at 150 °C for 10 h before use.

3.2.5 Friedel-Crafts reaction optimization: Effect of precursor concentration combined with thermal treatment

With further optimization of the synthesis, it is seen that not only the different TPM:FDA ratio leads to a good surface area and porosity suitable for the gas storage, but also the precursor concentration in DCE combined with post synthesis thermal treatment lead to a great improvement of the porosity of the materials. This optimization is still in progress, however one example of the synthesis procedure and the following thermal treatment, for the selected sample mPAF-1/8, is shown below:

mPAF-1/8 dil and mPAF-1/8 dil@380°C: Ferric chloride (4.055 g, 0.025 mol) and tetraphenylmethane (TPM 1 g, 0.0031 mol) were suspended in dichloroethane (DCE, 135 mL). The resulting mixture was vigorously stirred at room temperature to obtain a homogeneous solution, then formaldehyde dimethylacetal FDA, (1.90 g, 0.025 mol) was added dropwise. The resulting thick gel was stirred at room temperature for 4 hours and then heated to reflux for 17 hours. After cooling to room temperature, the gel was diluted with ethanol and

washed several times with water until the pH become neutral, and finally dried in an oven at 100 °C overnight to give **mPAF-1/8 dil**. The resulting polymer was heated at a temperature of 380 °C for 16 h with a heating rate of 2 °C/min, to obtain **mPAF-1/8 dil@380°C**.

mPAF-1/8 conc and mPAF-1/8 conc@380°C : Ferric chloride (4.055 g, 0.025 mol) and tetraphenylmethane (TPM 1 g, 0.0031 mol) were suspended in dichloroethane (DCE, 13.5 mL). The resulting mixture was vigorously stirred at room temperature to obtain a homogeneous solution, then formaldehyde dimethylacetal FDA, (1.90 g, 0.025 mol) was added dropwise. The resulting thick gel was stirred at room temperature for 4 hours and then heated to reflux for 17 hours. After cooling to room temperature, the gel was diluted with ethanol and washed several times with water until the pH become neutral, and finally dried in an oven at 100 °C overnight to give **mPAF-1/8 conc**. The resulting polymer was heated at a temperature of 380 °C for 16 h with a heating rate of 2 °C/min, to obtain **mPAF-1/8 conc@380°C**.

3.3 Results and discussion

3.3.1 mPAF materials with different TPM:FDA ratio.

In the optimization process of Friedel-Crafts reaction, at first we focused our study on understanding how different synthetic conditions and reagents ratio can influence the microscopic structure of the polymers. Different reaction conditions, which in principle could modulate the substitution of the aromatic residues from partial to extensive substitution, were explored. In particular all reaction parameters were kept constant except the amount of catalyst and FDA employed as crosslinking agent. We rationalized that ideal reaction conditions should exist to grant regular and extended polymerization giving narrow pore size and large surface areas. Therefore, at a first stage, the reaction was performed with a TPM:FDA ratio (1:3), lower than that needed for a full cross-linking polymerization, to get the first material (mPAF-1/3). Then, an intermediate crosslinking was explored by synthesizing a polymer with a TPM:FDA ratio 1:9 (mPAF-1/9). A TPM:FDA ratio 1:16 was also used to yield the (supposedly) fully cross-linked material mPAF-1/16. Indeed, under these conditions the electrophile (FDA) is over-stoichiometric allowing for fast polymerization. Finally, “forced” crosslinking conditions were also explored, synthesizing a polymer with a TPM:FDA ratio 1:30 (mPAF-1/30). Elemental analysis reported in table 3.1 showed that all the produced materials contain 10-15% of elements other than the expected C and H, as also reported in the literature for analogous polymeric systems [1, 8]. EDX data report that traces of chlorine, oxygen and iron are present in the material probably due to side reactions and residues of catalyst. We hypothesized that, as polyalkylation of the aromatic rings occurs in excess of FDA, the formation of chloromethyl or hydroxyl-methyl groups would arise in presence of chloride ions or traces of

water when there is no possibility to cross-link with another TPM unit. The scheme of the synthesis of mPAF materials is reported in the figure 3.4.

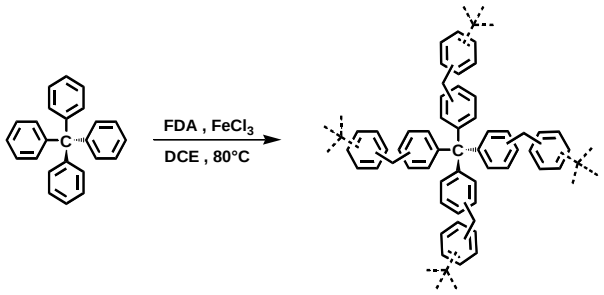

Figure 3.4. Scheme of the synthesis of mPAF materials

Structure, stability and porosity of the different mPAF-1/n polymers were characterized using different techniques such as elemental analysis (EA), Fourier transform infrared (FTIR), magic-angle spinning nuclear magnetic resonance (MAS NMR), thermogravimetric analysis (TGA), Scanning electron microscopy (SEM) analysis, powder X-ray diffraction (PXRD) and N_2 adsorption measurements at 77K.

3.3.1.1 FTIR Spectroscopy

Figure 3.5 shows the FTIR spectra of the mPAF polymers compared with the TPM precursor.

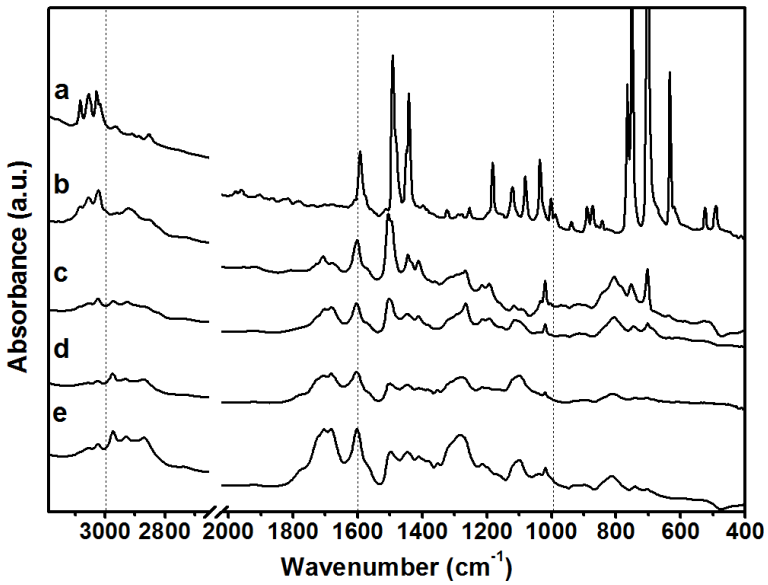

Figure 3.5. FTIR spectra of the tetraphenylmethane precursor (a), mPAF-1/3 (b), mPAF-1/9 (c), mPAF-1/16 (d), mPAF-1/30 (e) recorded as KBr pellets in the 3200-400 cm^{-1} frequency range.

In the high frequency region, both the TPM precursor (curve a) and the mPAF-1/n materials (curves b-e) are characterized by bands with medium intensity at 3100-3000 cm^{-1}, attributed to aromatic C-H groups stretching modes. After polymerization a new group of bands appears in the region 3000-2800 cm^{-1} due to the stretching of aliphatic C-H, related to methylene linkers between the aromatic rings and, in minor extent, to chloro-methylene residues. The low frequency region shows the presence of bands characteristic of substituted aromatic rings: the spectrum of mPAF-1/3 (Figure 3.5b) shows bands at 1600 cm^{-1} and 808 cm^{-1}, indicating a predominant 1,4-substitution. Increasing the relative concentration of FDA during the synthesis (mPAF-1/9, mPAF-1/16 and mPAF-1/30) increases crosslinking and multiple substitution of aromatic ring in different positions, as demonstrated by the increase of signals in the region 1650-1850 cm^{-1} [9]. All the materials prepared present characteristic band at 1441 cm^{-1} due to CH_2 bending mode of the methylene linker along with bands at 1414 cm^{-1} and 1269 cm^{-1} due to CH_2 bending and wagging modes of the chloro-methylene groups, respectively [10].

3.3.1.2 Solid-state ^{13}C MAS NMR

Standard CP MAS conditions at room temperature were used to acquire the $^{13}C[^{1}H]$ CPMAS NMR spectra on the different mPAF materials with short contact time of 2 ms (Figure 3.6, right).

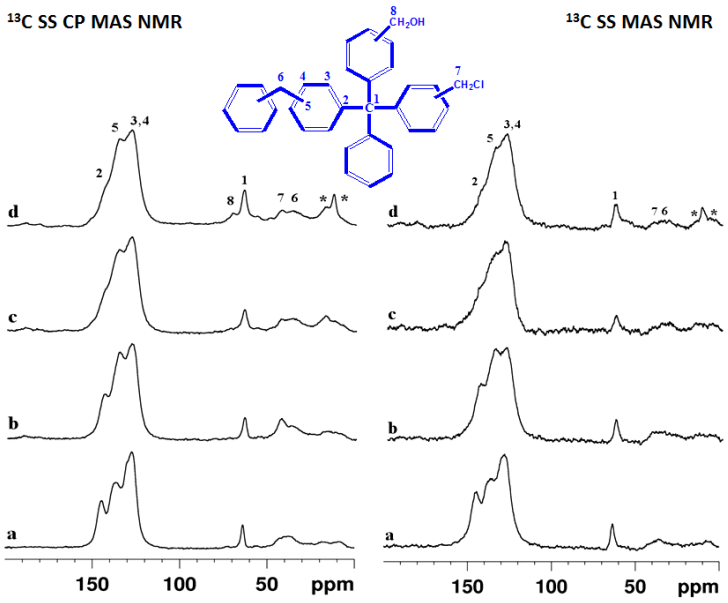

Figure 3.6. ^{13}C solid state CPMAS NMR (left) and ^{13}C solid state MAS NMR (right) spectra of mPAF-1/3 (a), mPAF-1/9 (b), mPAF-1/16 (c) and mPAF-1/30 (d). In the case of cross polarization were used a contact time of 2 ms and a MAS spin rate of 15 kHz in all the experiments. * denotes spinning sidebands.

In accordance to previous reports from the literature [1], all spectra show five peaks at about 37, 64, 128, 136 and 144 ppm. In the aliphatic carbon region, the methylene linking groups generate the peak at 37 ppm and quaternary carbon of TPM units at 64 ppm. The aromatic carbons signals are assigned as the following: 128 ppm for the aromatic C-H, 136 ppm for the methylene substituted aromatic carbons and 144 ppm for the carbon linked to the central tetrahedral carbon atom. Interestingly, the resolution of the peaks related to the aromatic carbons is reduced as the amount of FDA in the reaction increases, which confirms a greater substitution according to the FTIR spectra. Additional resonance is visible in the spectra at 43 ppm, which can be assigned to CH_2Cl substitution, while only for the sample mPAF-1/30 the spectrum shows a peak at 71 ppm probably due to CH_2OH groups [10]. However, in quantitative ^{13}C solid state MAS NMR spectra (Figure 3.6, left) this signal is under the limit of detectability: the chloromethyl carbon peak is found at very low intensity confirming that a small amount of these groups is formed during side reactions. Noteworthy, the resonances due to methylene carbons are broadened either due to the non-averaging of ^{13}C-$^{35,37}Cl$ residual dipolar couplings (as in $–CH_2Cl$) or due to the heterogeneous broadening associated with an extensive distribution of chemical shifts (as in Ph-CH_2-Ph). [1]

3.3.1.3 PXRD measurements

In order to probe the long-range structure of mPAF materials, powder X-ray diffraction (PXRD) studies were performed (figure 3.7).

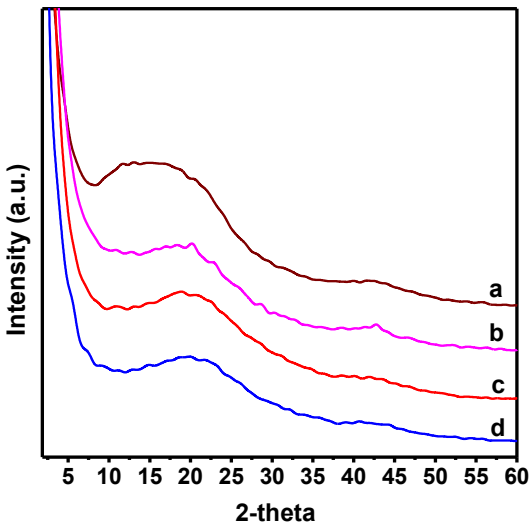

Figure 3.7. X-Ray powder pattern (Cu-Kα) of mPAF materials: (a) mPAF-1/3, (b) mPAF-1/9, (c) mPAF-1/16 and (d) mPAF-1/30.

The X-Ray patterns reported in figure 3.7 confirm the formation of amorphous materials, as expected for cross-linked polymers, with only two broad signals at 2Θ between15°- 20° and 43°, related to direct ring-ring interactions, which are favoured by the intrinsic flexibility of the polymeric structure [11].

3.3.1.4 Scanning electron microscopy analysis (SEM)

The morphology of the mPAF materials was further investigated by Scanning electron microscopy (SEM) (figure 3.8).

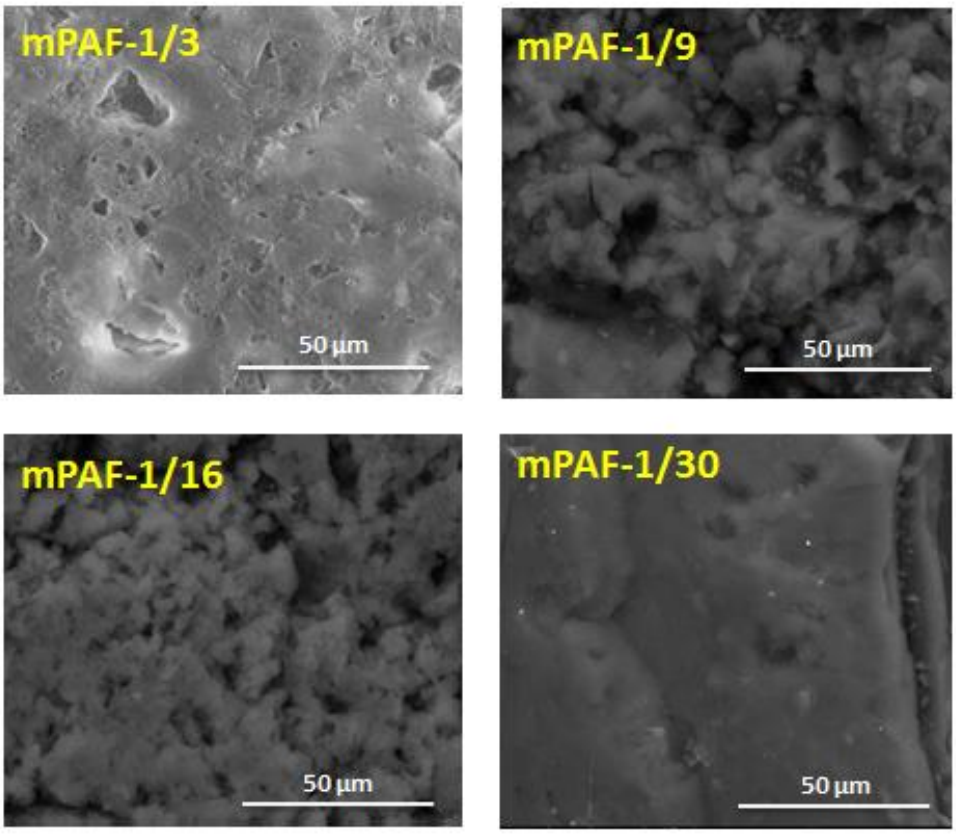

Figure 3.8. SEM images of mPAF materials at 2500 x magnification.

SEM images of all the materials indicate the presence of agglomerated particles with micrometer size.

3.3.1.5 Thermogravimetric analysis (TGA)

Thermogravimetric analysis (TGA) profiles of mPAF polymers are reported in figure 3.9.

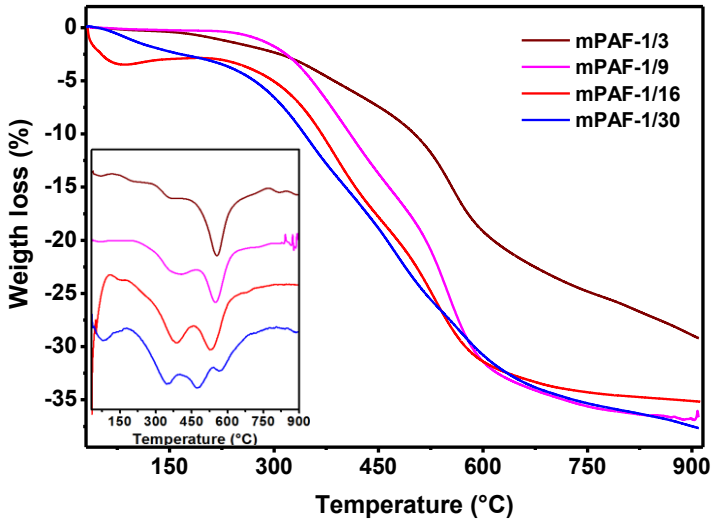

Figure 3.9. Thermogravimetric analysis (TGA) of mPAF materials from 60 to 900 °C at 5 °C/min under argon flow. In the inset are shown the DTG derivative curves.

All the materials show a good thermal stability. They are characterized by a weight loss of 8-15% between 250 and 450 °C, which can be correlated to the removal of solvent, FDA and side-products entrapped inside the pores. The degradation of the framework is found at temperatures higher than 450 °C.

3.3.1.6 Pore distribution and surface area

The polymer porosity was analysed by adsorbing N_2 at 77K: adsorption/desorption isotherms were collected for all the mPAF materials (Figure 3.10a).

The isotherms can be classified as type I, with large quantities of gas (>200 cm^3/g) adsorbed at relative low pressures, as expected for microporous materials. All the samples display also a further gradual filling of mesopores at higher relative pressures in the range 0.45-1 P/P_0. All the materials showed a H_2-type hysteresis in the desorption branch, indicative of mesoporous phase. The apparent BET surface areas (table 3.2) were calculated over a relative pressure range P/P_0 of 0.05−0.15.

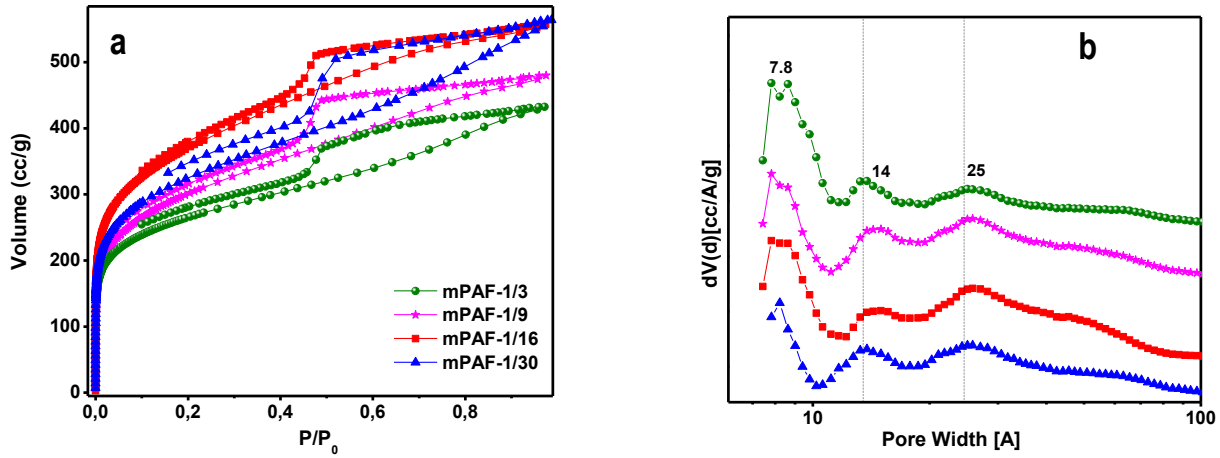

Figure 3.10. N_2 physisorption isotherms (a) and pore size distribution (b) of the mPAF polymers: mPAF-1/3 (green spheres), mPAF-1/9 (magenta stars), mPAF-1/16 (red squares) and mPAF-1/30 (blue triangles).

N_2 isotherms show that the increase of the FDA:TPM ratio leads to materials with a progressively larger surface area, from 948 m^2/g for mPAF-1/3 (FDA:TPM ratio 3:1) to 1063 m^2/g for mPAF-1/9 (ratio 9:1), and 1314 m^2/g for mPAF-1/16 (ratio 16:1). A further increase in FDA:TPM ratio to 30:1 corresponds to a lower surface area (1162 m^2/g) measured for mPAF-1/30 sample.

Table 3.2: BET, Langmuir surface area and pore size distribution of mPAF polymers obtained from N_2 physisorption measurements at 77 K.

Sample	BET surface area (m^2/g)	Langmuir surface area (m^2/g)	Total Pore Volume (cc/g)	Micropore Volume (cc/g)		
				<10Å	10<Å<20	Total
mPAF-1/3	948	1254	0.64	0.099	0.08	0.17
mPAF-1/9	1063	1512	0.71	0.08	0.08	0.16
mPAF-1/16	1314	1827	0.83	0.11	0.10	0.21
mPAF-1/30	1162	1655	0.83	0.097	0.095	0.19

The pore size distribution was assessed by NLDFT approach (Figure 3.10b): the mPAF materials show several families of pores, namely micropores at ca. 8 and 14 Å, and mesopores broadly distributed around 25 Å. In the series, the increase in surface area and pore volume (table 2) can be related to enhanced polymerization degree, associated to higher crosslinking.

3.3.2 Post-synthetic temperature treatments of mPAF-1/16

The mPAF-1/16 obtained with a fair excess of FDA in the reaction mixture is the material with the highest micropore volume and surface area. Starting from this material, we optimized a post synthesis process to further improve the textural properties. The complete characterization of mPAF materials showed the presence of residual FDA fragments and side products entrapped inside the pores. Indeed, from TGA is evident the presence of two weight losses separated, the first due to the impurities and the second due to the framework. The presence of these entrapped impurities is also demonstrated by IR spectroscopy and SS-NMR. For this reason, it was decided to treat thermally at 380°C under N_2 flow the mPAF-1/16 material, in order to investigate how the structure and the physic-chemical properties change after the elimination of the first weight loss.

The material was also mixed with KOH and treated at 800 °C under N_2 flow. In this case, the very high temperature chosen, and the presence of KOH as active reagent, gives rise to the carbonization of the material. This is an effective method for preparation of highly microporous materials. Traditionally, porous carbons were obtained by physical or chemical activation of carbonaceous materials. The commonly used activated agent are CO_2, steam, KOH, $ZnCl_2$ and so on [12, 13]. Nowadays, new types of porous carbons based on synthetic polymers are extensively investigated. Compared with conventional activated carbons and biomass-derived carbons, the use of synthetic polymers as porous carbon precursors enables better chemical composition control, easy-to-achieve precise morphology, tunable pore system, and targeted surface chemistry [14].

Recently, KOH has been shown to activate porous polymers by producing porous carbons with high surface area and excellent gas storage properties [15, 16]. Y. Li et al. [17], for example, by KOH chemical activation at different temperatures (500-900°C) of PAF-302 porous polymer, prepared porous carbons with both high surface area and CO_2, CH_4 and H_2 high heat of adsorption. Herein, we use a similar approach for the preparation of KOH-activated carbonized mPAF-1/16 with relevant increase in its surface area and microporous volume.

The thermal stability of the thermally treated polymers was studied by TGA, whereas their structural properties were characterized using FTIR and SS-NMR spectroscopic techniques.

3.3.2.1 Thermogravimetric analysis (TGA)

The thermal treatments allow the preparation of two different materials starting from mPAF-1/16:

- mPAF-1/16@380 prepared by heating mPAF-1/16 at 380°C for about 16h under N_2 flow.

- mPAF-1/16@800-KOH prepared by carbonization of mPAF-1/16 in the presence of KOH at a temperature of 800°C for 2h under N_2 flow.

TGA analysis was performed to evaluate how the thermal properties of the material change after the treatments described above. Figure 3.11 shows the comparison of the three materials mPAF-1/16 (curve a), mPAF-1/16@380 (curve b) and the carbonized material mPAF-1/16 @800-KOH (curve c).

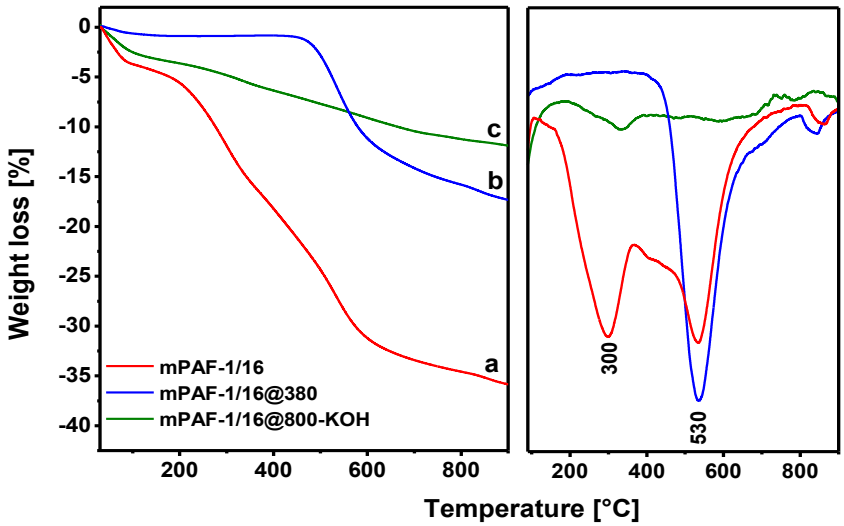

Figure 3.11. TGA analysis (A) and DTG derivative curves (B) of mPAF-1/16 (a), mPAF-1/16@380 (b) and mPAF-1/16@800- KOH (c) samples, performed under Ar flow (20 mL / min) and using a heating ramp of 2°C/min.

After the treatment at 380°C the thermal profile of mPAF-1/16@380 sample (curve b) showed only one weight loss, at about 530°C due to structure decomposition. This behaviour demonstrates the complete removal of the impurities trapped in the porous structure. TGA data indicated that the thermal treatment at 380°C does not alter significantly the thermal stability of the mPAF-1/16 framework.

The thermal profile of mPAF-1/16@800-KOH sample (curve c) showed the transformation of the framework after the carbonization, as demonstrated also by FTIR spectrum showed in the following section.

3.3.2.2 FTIR Spectroscopy

The Fourier transform infrared (FTIR) spectra of the samples are shown in figure 3.12.

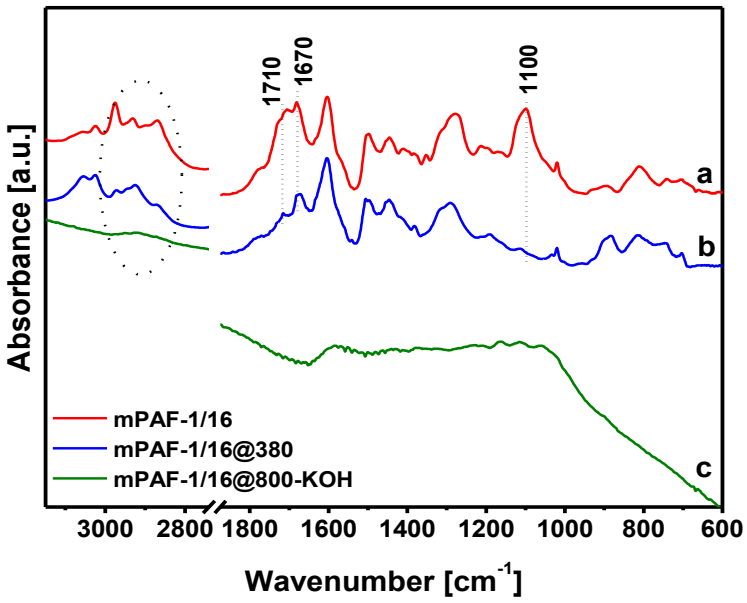

Figure 3.12. FTIR spectra in the region 3100-600 cm^{-1} of mPAF-1/16 (a), mPAF-1/16@380 (b) and mPAF-1/16@800-KOH (c) samples.

In the high frequency region, the spectrum of mPAF-1/16@380°C shows the bands ranging between 3000-2800 cm^{-1} assigned to the stretching of aliphatic C-H, intensively weakened (figure 3.12, curve b) in comparison to the parent mPAF-1/16. This demonstrates the removal of aliphatic impurities from the material. In particular, the band at 2975 cm^{-1}, which can be assigned to the asymmetric stretching of methyl groups, from FDA fragments disappeared.

In the low frequency region, also the bands at 1710 and 1670 cm^{-1}, due to vibrations of substituted aromatic rings, undergo an intensity decrease. This demonstrates that in addition to impurities, the treatment also removed part of the chloro-methylene groups, but not all. Indeed, the band at 1269 cm^{-1} due to CH_2 wagging mode of the chloro-methylene groups, is still present, but with less intensity compared to the situation before the treatment.

The absorption at 1100 cm^{-1}, which is very intense in mPAF-1/16 material, disappears completely in the mPAF-1/16@380. This band is assigned to ether group and confirms that the treatment cleaned the pores from fragments of FDA trapped in the pores.

The FTIR spectra of carbonized mPAF-1/16@800-KOH , is characterized only by a very broad band in the range 1600-1000 cm^{-1}, which confirm the complete decomposition and transformation of the starting mPAF-1/16 material.

3.3.2.3 Solid-state ^{13}C MAS NMR

Solid state ^{13}C nuclear magnetic resonance (SS-NMR) both qualitative (left) and quantitative (right) spectra of mPAF-1/16 (curve a) and mPAF-1/16@380 (curve b) are shown in figure 3.13.

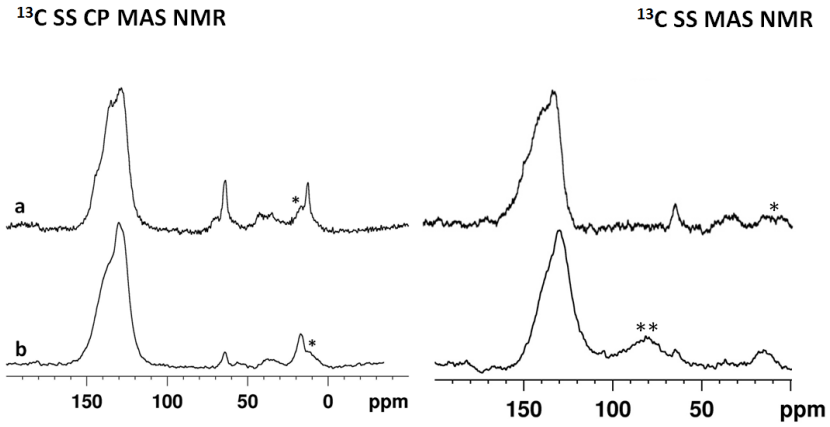

Figure 3.13. ^{13}C solid state CPMAS NMR (left) and ^{13}C solid state MAS NMR (right) spectra of mPAF-1/16 (a) and mPAF-1/16@380 (b) samples. In the case of cross polarization a contact time of 2 ms and a MAS spin rate of 15 kHz were used in all the experiments. * denotes spinning sidebands. ** band due to the background.

The band centred at 80 ppm in the quantitative spectrum of mPAF-1/16@380 is not due to species contained in the sample but only to the background.

The broad band in the range 150-100 ppm, assigned to the aromatic carbon atoms, didn't undergo any change after the thermal treatment. In the ^{13}C solid state CPMAS NMR spectra the signals at *ca*. 65 ppm and at ca. 35 ppm are maintained in the mPAF-1/16@380 spectra. They are assigned to the quaternary carbon and to the methylene carbon formed after Friedel-Crafts reaction, respectively. The peaks falling in the range 10-20 ppm, are hardly assignable considering the reaction mechanism known for the Friedel-crafts reaction. However, in quantitative ^{13}C solid state MAS NMR spectra (Figure 3.13, left) these signals are under the limit of detectability.

3.3.2.4 N_2 physisorption at 77K

The textural analysis of thermally treated mPAF-1/16 samples was made by N_2 physisorption at 77K. Before the analysis, the samples were outgassed at 150°C for 18 hours.

The physisorption isotherms (frame A) and pore size distribution (frame B) for mPAF-1/16 (red circles), mPAF-1/16@380 (blue tringles) and mPAF-1/16@800-KOH (green stars) samples are reported in figure 3.14.

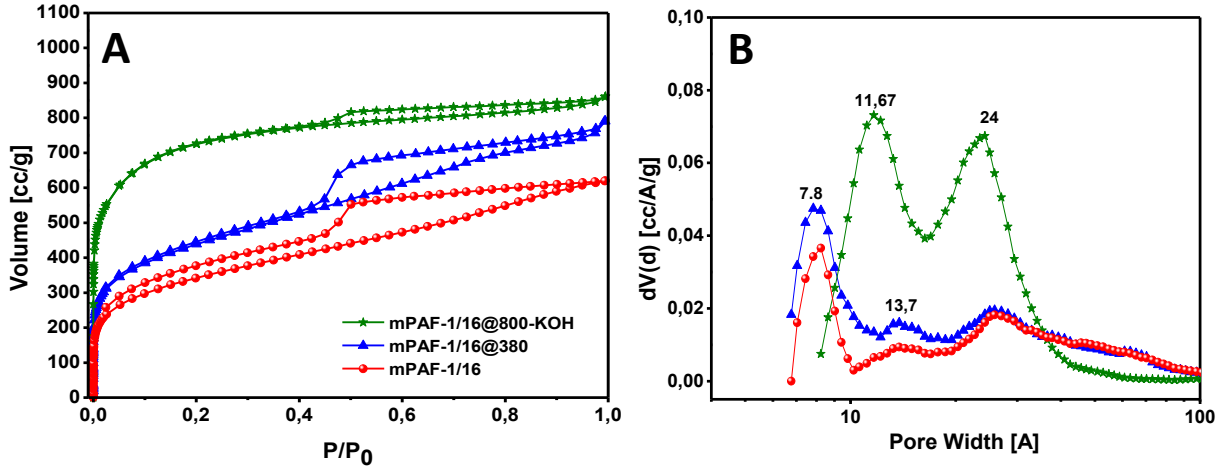

Figure 3.14. N_2 adsorption-desorption isotherms at 77K and relative pressures (P/P_0) from $1x10^{-7}$ to 1 (A) and pore size distribution determined by NLDFT method applied on silica surface with cylindrical geometry (B) of mPAF-1/16 (red circles), mPAF-1/16@380 (blue triangles) and mPAF-1/16@800-KOH (green stars) samples.

According to the IUPAC classification, mPAF-1/16 and mPAF-1/16@380 display a type I isotherm in adsorption branch with H_2-type hysteresis in the desorption branch, while mPAF-1/16@ 800-KOH displays a type I isotherm with a minimal hysteresis at higher relative pressures.

All isotherms show a large quantity of gas (>200 cm^3/g) adsorbed at low relative pressures, as expected for microporous materials. They also display a further gradual filling of mesopores at higher relative pressures in the range 0.45-1 P/P_0. The apparent BET surface areas were calculated over a relative pressure range P/P_0 = 0.05−0.15.

The porous properties of the polymers are summarized in table 3.3, where mPAF-1/16@800- KOH shows the highest BET surface area (2700 $m^2\ g^{-1}$), followed by mPAF-1/16@380 (1513 $m^2\ g^{-1}$). Figure 3.14B shows the pore size distribution for the thermally treated materials compared with mPAF-1/16 calculated using nonlocal density functional theory (NLDFT) on silica surface with cylindrical geometry applied in the adsorption branch: the method chosen gave the smallest fitting error. mPAF-1/16 and mPAF-1/16@380 polymers exhibit similar predominant microporosity with micropores of ca. 8 and ca. 14 Å and mesopores at about 25 Å. The carbonized mPAF-1/16@800-KOH shows a different pore distribution compared with the starting material

mPAF-1/16 consisting in a bimodal pore distribution with two families, a microporous distribution centred at about 12 Å and a mesoporous one at 24 Å.

Table 3.3. Surface properties and pore volume for mPAF-1/16, mPAF-1/16@380 and mPAF-1/16@800-KOH, a) Surface area calculated from the nitrogen adsorption isotherm using the BET method; b) Total pore volume at P/P_0=0.995; c) Micropore volume derived using NLDFT method.

Polymer	SSA_{BET}(a) [m^2/g]	V_{TOTAL}(b) [cc/g]	V_{MICRO}(c) [cc/g]
mPAF-1/16	1232	0,92	0,14
mPAF-1/16@380	1513	1,01	0,262
mPAF-1/16@ 800-KOH	2700	1,25	0,63

These results show that the treatment at lower temperature (i.e. mPAF-1/16@308) maintains the structure of the mPAF-1/16 starting material even though increasing its BET surface area and pore volume. These results demonstrate that the thermal treatment remove the side-products of the cross-linking polymerization entrapped in the micropores. On the other hand, the carbonization leads to a different material, with very high surface area and high micropore volume of 0.63 cc/g.

3.3.3 Wet post-synthesis amination of mPAF-1/16

It is well known from the literature that the incorporation of heteroatoms (e.g. N, O, S) is a promising potential route to increase CO_2 sorption capacity, as electron rich functional groups in the networks could result in strong dipole–quadrupole interactions with CO_2 molecules [18, 19]. To achieve this goal, amino groups were introduced by means of the wet post-synthesis: Mao et al [20] reported a study on HCP materials based on polystyrene with residual chloromethyl groups which can be replaced by other functional groups such as amino group by simple nucleophilic substitution. Also the mPAF polymers synthesized in this thesis have a small amount of chloro-methylene residues, as demonstrate above. We used the same method to substitute chlorines with three different types of amines: methylamine, diethylamine and triethylenetetramine (TETA). The amine functionalization was done on the material mPAF-1/16 that showed the highest surface area and pore volume.

Figure 3.15 shows the scheme of the amine functionalization of mPAF-1/16 material.

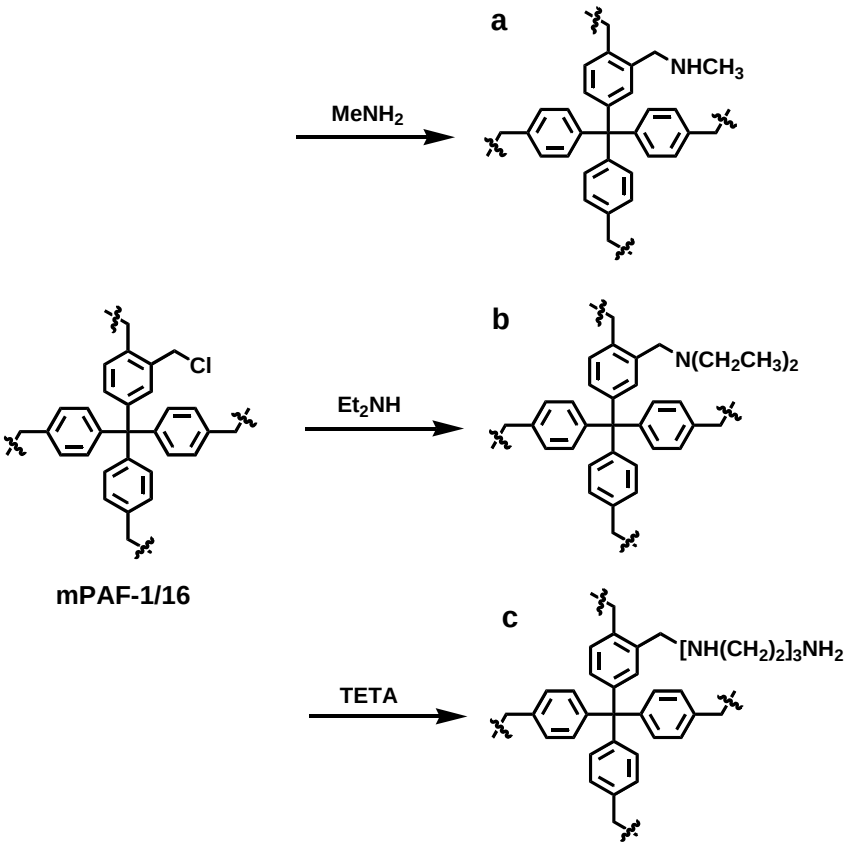

Figure 3.15. Schematic representation of the amine functionalization of mPAF-1/16 material: mPAF-1/16-NHMe (a), mPAF-1/16-NEt_2 (b) and mPAF-1/16-TETA (c).

Table 3.4. Elemental analysis and EDX of the amine functionalized mPAF materials

Material	**Elemental analysis (%)**			**EDX analysis (%)**
	N %	**C %**	**H %**	**Cl %**
mPAF-1/16	--	76,12	4,74	2,16
mPAF-1/16-NHMe	2,60	76,90	5,16	0,58
mPAF-1/16-NEt_2	2,32	77,54	5,29	0,60
mPAF-1/16-TETA	6,66	65,51	5,40	--

Elemental analysis and EDX data (Table 3.4), demonstrate the successful substitution of chlorine with alkyl amine groups in the mPAF-1/16 material: the starting amount of chlorine (2,16%) in the mPAF-1/16 polymer, decreases in the amine functionalized mPAF-1/16. Simultaneously, the percentage of nitrogen, carbon and hydrogen increase as a result of the introduction of alkyl amine groups.

3.3.3.1 FTIR Spectroscopy

The resulting polymers were analysed by infrared spectroscopy (FTIR) to validate the chemical structure. Figure 3.16 reports the IR spectra of mPAF-1/16-NHMe (curve b), mPAF-1/16-NEt_2 (curve c) and mPAF-1/16-TETA (curve d) compared with the starting material mPAF-1/16 (curve a).

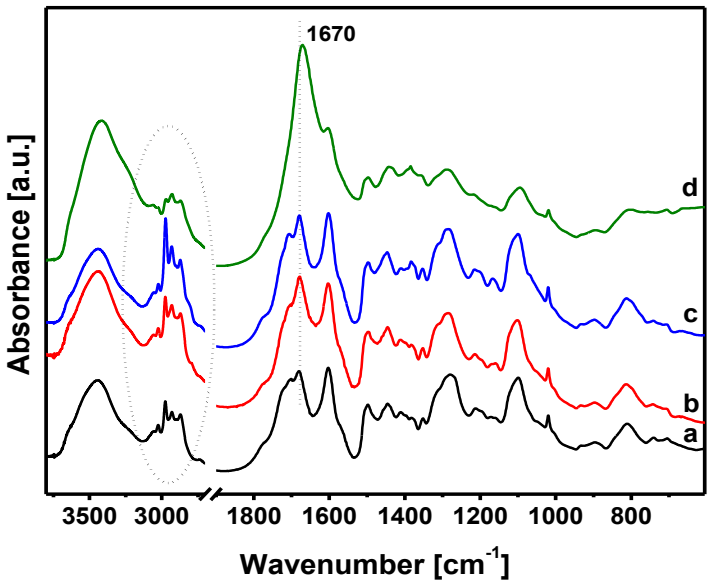

Figure 3.16. FTIR spectra in the region 3600-600 cm^{-1} of mPAF-1/16 (a), mPAF-1/16-NHMe (b) mPAF-1/16-NEt_2 (c) and mPAF-1/16-TETA (d) samples, recorded as KBr pellets.

After amination, in the high frequency region the materials show an increase in the intensity of the aliphatic bands in the range 3000-2800 cm^{-1} (curves b-d). This demonstrates the introduction of CH_2 and CH_3 groups of the alkyl amines. In the low frequency region the structural bands of the original polymer hide the new bands referred to amine groups.

3.3.3.2 Solid-state ^{13}C MAS NMR

Standard CP MAS conditions at room temperature were used to acquire the $^{13}C[^1H]$ CPMAS NMR spectra on the amine functionalized mPAF-1/16 materials with short contact time of 2 ms (Figure 3.17).

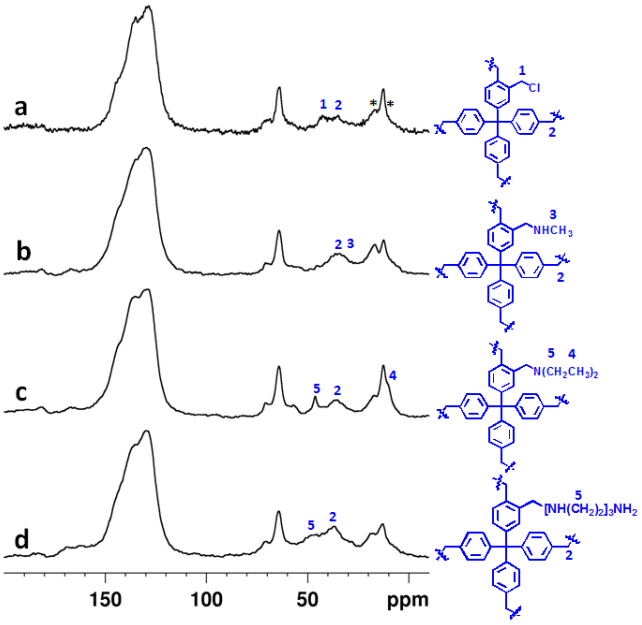

Figure 3.17. ^{13}C CP MAS NMR of mPAF-1/16 (a), mPAF-1/16-NHMe (b), mPAF-1/16-NEt_2 (c) and mPAF-1/16-TETA (d) samples. * denotes spinning sidebands

As it can be seen from figure 3.17, the aromatic carbons, the quaternary carbon of TPM units and the methylene linking groups signals didn't undergo significant change after the amination. In the aliphatic carbon region, the peak at 43 ppm, which is assigned to CH_2Cl substitution, disappeared after the amination, as expected. Additional resonances are visible in the spectra of mPAF-1/16-NHMe, mPAF-1/16-NEt_2 and mPAF-1/16-TETA due to the introduction of CH_2 and CH_3 of alkyl amine groups, as assigned in the structural schemes reported in the figure 3.17.

3.3.3.3 Thermogravimetric analysis (TGA)

The thermal stability of the amine functionalized mPAF materials was investigated using thermogravimetric analysis (TGA). The thermograms and the relative derivatives are reported in figure 3.18.

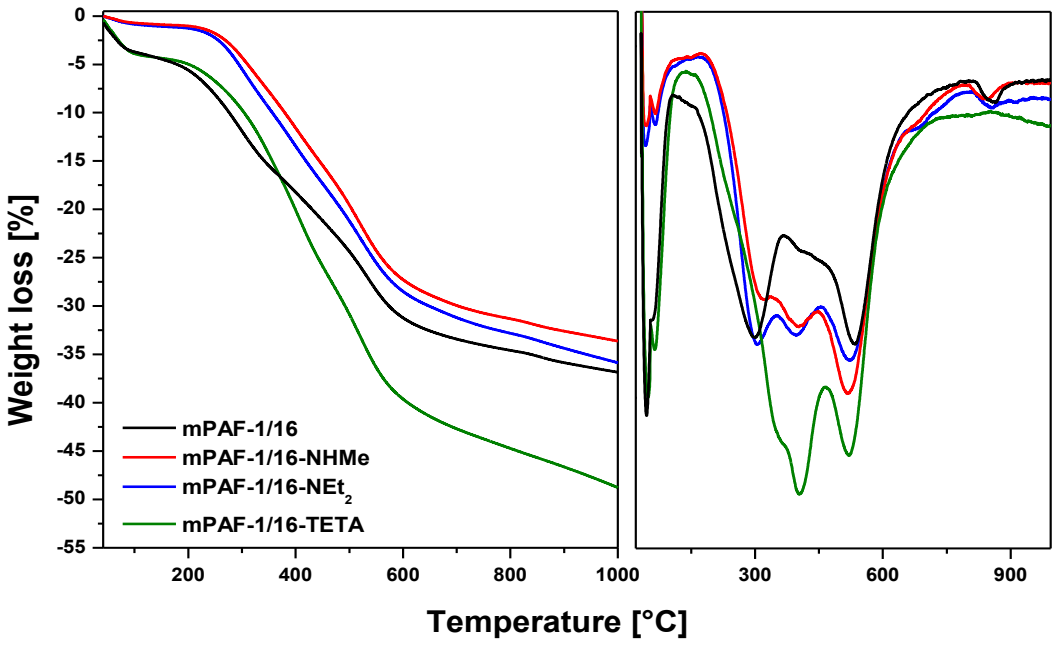

Figure 3.18. Thermogravimetric analysis (TGA) and DTG derivative curves of amine functionalized mPAF-1/16 materials, under argon flow from 60 to 1000 °C at 2 °C/min.

TGA shows for all materials a starting weigh loss before 100 °C, suggesting the presence of trapped solvents used during the functionalization. The presence of the alkyl amine groups modifies the TGA profiles especially in the temperature range of 200-450°C. mPAF-1/16-NHMe and mPAF-1/16-NEt_2 show weigh loss at 300 and 395 °C with a percentage of 12%, whereas the mPAF-1/16-TETA thermogram is characterized by a predominant weigh loss of 16% centred at 400°C. The degradation of the frameworks is found at temperatures higher than 450 °C, as for the parent mPAF-1/16 sample. These results confirm that embedded side-products, or functional groups bound to the aromatic skeleton, can be removed at temperatures ranging 200 to 450°C.

3.3.3.4 N_2 physisorption at 77K

The polymer porosity was analysed by N_2 physisorption at 77K: adsorption/desorption isotherms were collected for all the amine functionalized mPAF materials (Figure 3.19).

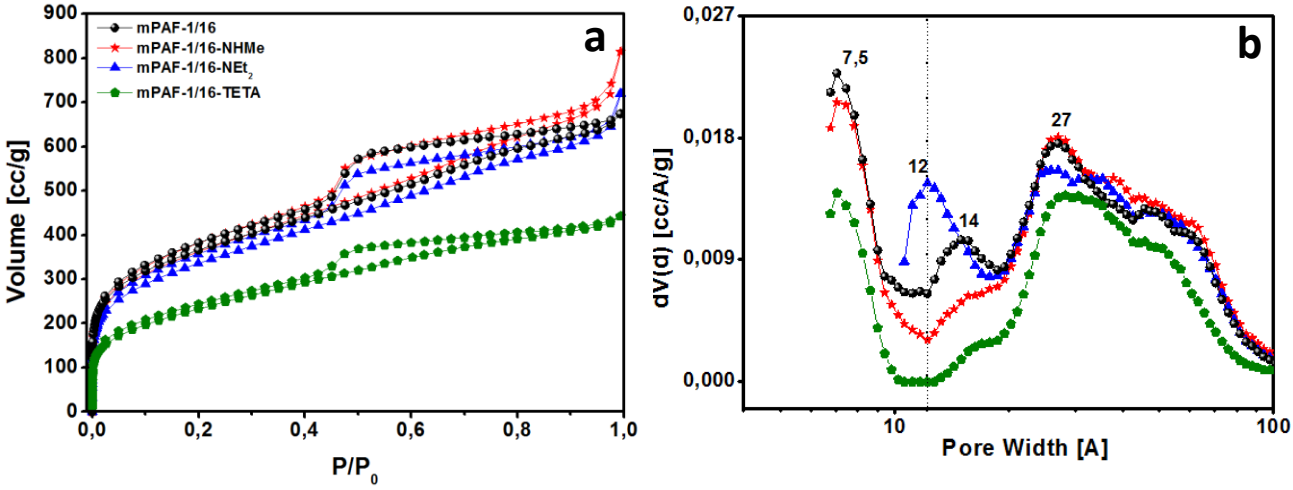

Figure 3.19. (a) N_2 adsorption-desorption isotherms at 77K in the relative pressure (P/P_0) range from $1x10^{-7}$ to 1 and (b) pore size distribution determined by NLDFT method applied on silica surface with cylindrical geometry of mPAF-1/16 (black circles), mPAF-1/16-NHMe (red stars), mPAF-1/16-NEt_2 (blue triangles) and mPAF-1/16-TETA (green polygons) samples.

The isotherms can be classified as type I, with large quantities of gas (150-200 cm^3/g) adsorbed at low relative pressures, as expected for microporous materials. All the samples, similarly to mPAF-1/16, show mesopores at higher relative pressures and a H_2-type hysteresis in the desorption branch. The apparent BET surface areas were calculated over a relative pressure range P/P_0=0.05−0.15.

The porous properties of the polymers are summarized in Table 3.5. The functionalization of mPAF-1/16 led to progressive decrease in the surface area of the resulting materials: 1304,37 $m^2\ g^{-1}$ for mPAF-1/16-NHMe, 1211,87 $m^2\ g^{-1}$ for mPAF-1/16-NEt_2 and the lowest surface area is 835,13 $m^2\ g^{-1}$ for the polymer mPAF-1/16-TETA.

Figure 3.19B shows the pore size distribution for the amino-functionalized materials compared with mPAF-1/16 calculated using nonlocal density functional theory (NLDFT) on silica surface with cylindrical geometry applied in the adsorption branch. The method chosen was the one that gave the smallest fitting error. mPAF-1/16, mPAF-1/16-NHMe and mPAF-1/16-TETA polymers exhibit similar pore distributions: the dominant pores are 7,5Å width, followed by pores of ca. 14Å and mesopores in the 23-65 Å range. The microporosity of the mPAF-1/16-NEt_2 is different in that pores of 12 Å characterized it, whereas the mesoporous distribution is similar to the other polymers.

Table 3.5. Surface properties and pore volume for amine functionalized polymers compared with mPAF-1/16, a) surface area calculated from the nitrogen adsorption isotherm using the BET method; b) Total pore volume at P/P_0=0.995; c) The micropore volume derived using NLDFT method.

Polymer	SSA $_{BET}$[a] [m²/g]	V $_{TOTAL}$[b] [cc/g]	Micropore Volume [c] (cc/g)		
			<10Å	10<Å<20	Total
mPAF-1/16	1380,16	0,99	0,087	0,083	0,17
mPAF-1/16-NHMe	1304,37	1,15	0,073	0,057	0,13
mPAF-1/16-NEt_2	1211,87	1,01	--	--	0,12
mPAF-1/16-TETA	835,13	0,65	0,047	0,015	0,062

Similarly to the surface area, the total micropore volume decreases in the amino functionalized materials. The trend indicates that the functionalization led to a progressive occlusion of the micropores with increasing the steric hindrance of the groups introduced. This confirms the success in the amine functionalization of the materials.

3.3.4 mPAF polymers with different tetrahedral monomers

Having successfully synthesized HCP polymers starting from TPM, we then selected other rigid tetrahedral monomers as building blocks. The core of the monomers was chosen from atoms different from carbon (silicon and tin) or chemical structures able to form 3D polymers (adamantane, ethylene and ethane). The same cross-linking polymerization using the optimized ratio 1:16 between precursor and FDA was carried out with the five monomers reported in figure 3.20.

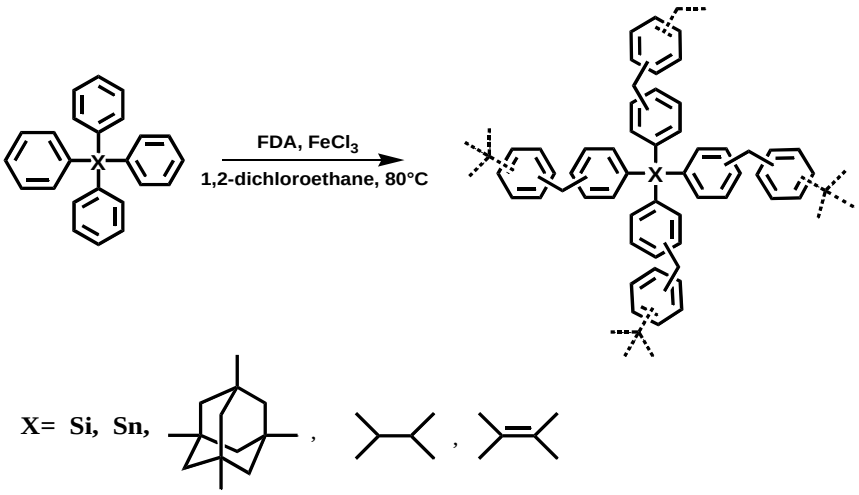

Figure 3.20. Schematic depiction of the synthesis of mPAF materials with different tetrahedral monomer

Typically, methylene groups connect the tetrahedral building blocks and chloromethyl functional groups can be retained in the networks. As discussed for the synthesis of mPAF materials with different TPM:FDA ratio, the formation of chloromethyl groups would arise in presence of chloride ions when there is no possibility to cross-link with another aromatic ring unit. The structure, stability and porosity of the materials were fully characterized with the usual techniques used in this thesis. In the table 3.6 are listed the precursors together with the adopted acronyms of the polymers.

Table 3.6. Tetrahedral precursors and acronyms of the corresponding polymers

Precursor name	Polymer name
Tetraphenylmethane (TPM)	mPAF-1/16
Tetraphenylsilane (TPS)	mPAF-TPS
Tetraphenyltin (TPT)	mPAF-TPT
Tetraphenyladamantane (TPA)	mPAF-TPA
Tetraphenylethane (TPEa)	mPAF-TPEa
Tetraphenylethene (TPE)	mPAF-TPE

All mPAF materials could not be dissolved or decomposed in common organic solvents such as DMF, $CHCl_3$, THF, etc. or in the presence of strong acid or bases, indicating their high chemical stability.

3.3.4.1 FTIR Spectroscopy

The reaction procedures were monitored by Fourier transform infrared (FTIR) spectroscopy. The FTIR spectra of mPAF materials with different tetrahedral monomers are compared with those of their precursors in figures 3.21A-E.

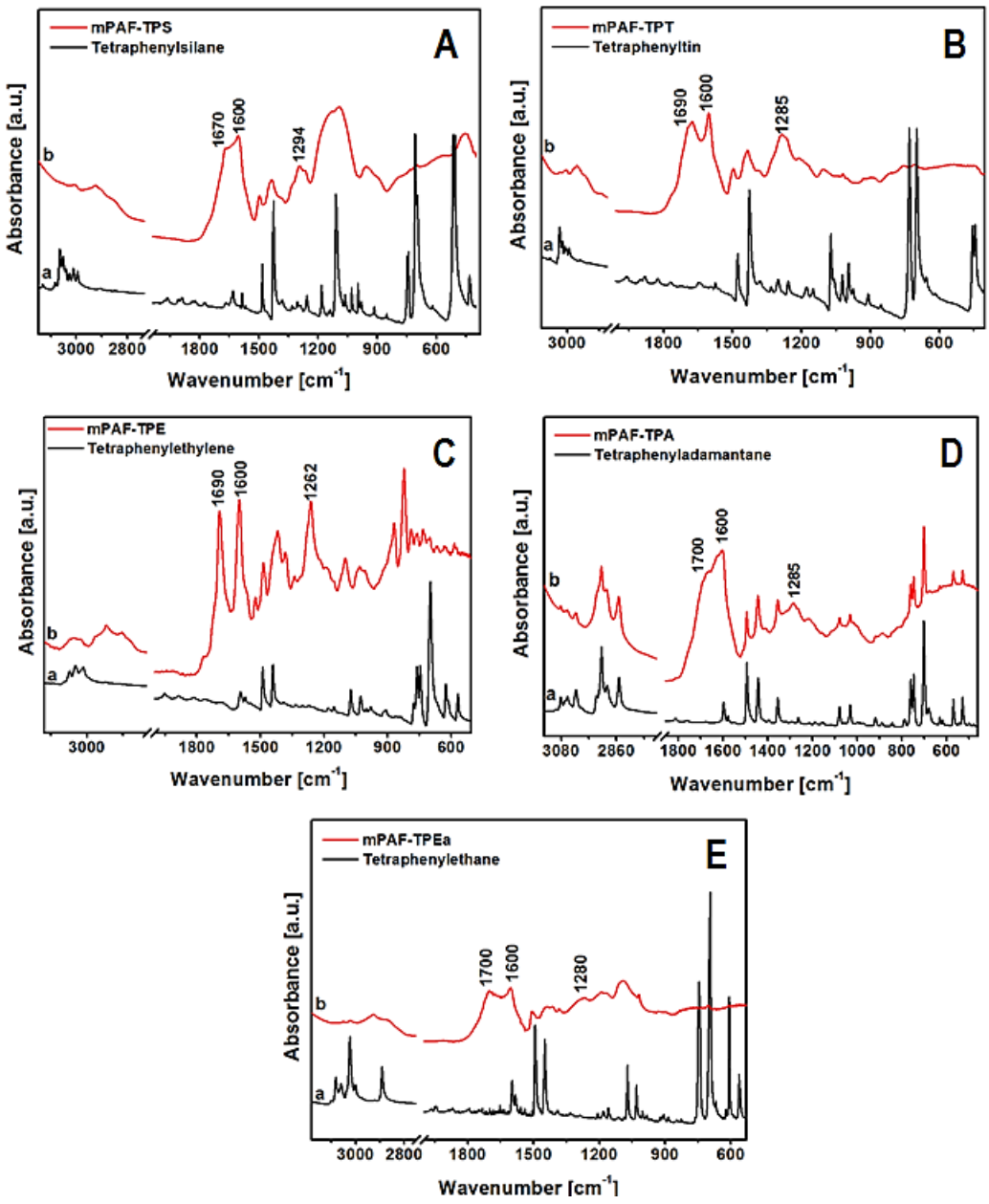

Figure 3.21. FTIR spectra of the precursors compared with the relative polymers, recorded as KBr pellets in the 3200-500 cm^{-1} frequency range: tetraphenylsilane and mPAF-TPS (A), tetraphenyltin and mPAF-TPT (B), tetraphenylethylene and mPAF-TPE (C), tetraphenyladamantane and mPAF-TPA (D) and tetraphenylethane and mPAF-TPEa (E). In each spectrum the precursor is indicated with letter (a) and the polymer (b).

The comparison between the spectra of the precursor and the polymers clearly indicates the successful formation of the expected polymers. In the high frequency region, bands with medium intensity at 3100 and 3000 cm^{-1}, due to C-H stretching modes of the aromatic rings, characterize both precursors and materials. After polymerization, a new group of bands appears in the region 3000-2800 cm^{-1} due to the C-H stretching of aliphatic groups, related to methylene linkers between the aromatic rings and, in minor extent, to chloro-methylene residues. Only the mPAF-TPA material shows minor changes in this region due to the presence of -CH_2- functional groups of the starting precursor, which hide polymer bands. This means that a mixture of mPAF-TPA and unreacted TPA is present in the latter sample.

The low frequency region of FTIR spectra shows the presence of bands characteristic of substituted aromatic rings: all the polymer spectra are characterized by signals at about 1700 and 1600 cm^{-1}, which indicate multiple substitution of aromatic ring in different positions. Additionally, all the materials prepared present characteristic band at 1441 cm^{-1} due to CH_2 bending mode of the methylene linker along with bands at 1414 cm^{-1} and 1262 -1285 cm^{-1} due to CH_2 bending and wagging modes, of the chloro-methylene groups, respectively.

3.3.4.2 Solid-state ^{13}C MAS NMR

Further investigation of the local structure of these mPAF materials was performed by solid-state ^{13}C CP MAS NMR spectroscopy (figure 3.22).

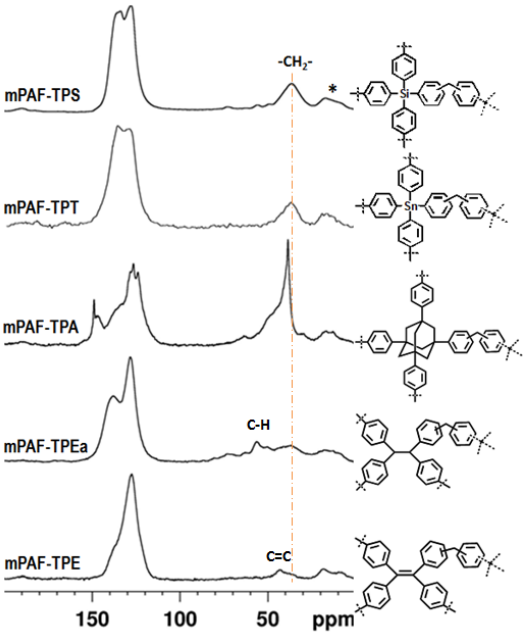

Figure 3.22. ^{13}C CP MAS NMR spectra of mPAF polymers with different tetrahedral centres. * denotes spinning sidebands

The ^{13}C CP/MAS NMR spectra of mPAF materials (figure 3.22) show somehow similar resonance peaks, due to the similarity of the polymer structure. Only the spectrum of mPAF-TPA is completely different due to the adamantane structure and, in agreement with IR results, to the presence of unreacted precursor, which gives a very narrow peak at about 40 ppm that hides some of the peaks associated to the polymer. The strong signals in the range 150–110 ppm are attributed to the aromatic carbon atoms, whereas the signals at approximately 35 ppm are due to the methylene carbon atoms, which connect the monomeric units. This confirms the formation of the polymers. The other signals present in the spectra are due to the carbon atoms connecting the four aromatic rings of the monomer building blocks: the assignment is reported directly in figure 3.22.

3.3.4.3 Thermogravimetric analysis (TGA)

The thermal stability of the mPAF materials with different tetrahedral monomers was investigated by TGA. The thermograms and the relative derivatives are reported in the figure 3.23.

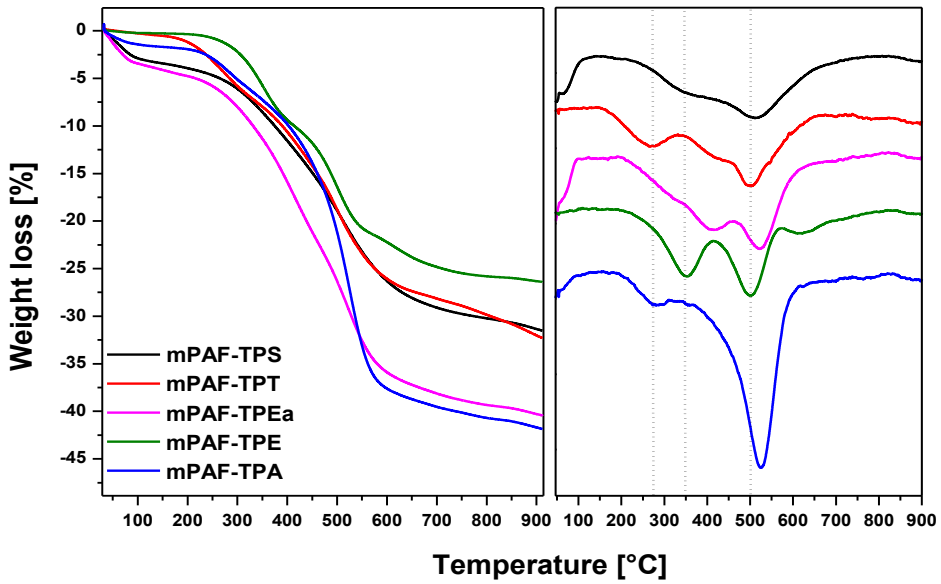

Figure 3.23. TGA (left panel) and DTG (right panel) plots of mPAF materials with different tetrahedral monomers, recorded under argon atmosphere with a heating ramp of 2°C/min up to 900 °C

TGA under inert conditions showed for all materials two main weigh losses: the first decomposition was found between 200 and 450 °C. Depending on the polymers, this weight loss is referred to one or two species, which could be assigned to FDA fragments and side products as demonstrated for mPAF materials obtained from TPM precursor. The second weight loss starts at about 450 °C and indicates the beginning of the framework decomposition. This demonstrates the high thermal stabilities of the polymers.

3.3.4.4 PXRD measurements

In order to evaluate if the prepared materials show a long-range order, PXRD was carried out and the diffraction patterns are reported in figure 3.24.

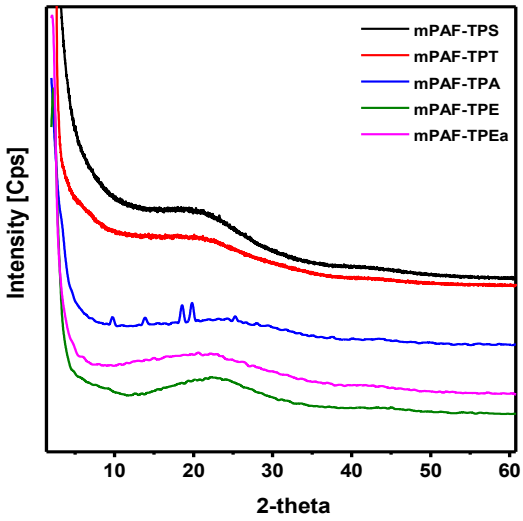

Figure 3.24. PXRD patterns of mPAF materials with different tetrahedral monomers.

PXRD patterns show that the resulting polymeric materials are characterized by amorphous phases: there is only the broad signal at 2Θ between 15°- 20°, related to direct ring-ring interactions. As already seen in the NMR and IR spectra of mPAF-TPA, also the X-ray diffraction confirms the presence of crystalline domains in the material, probably due to unreacted adamantane precursor.

3.3.4.5 Pore distribution and surface area

Finally, the pore characteristics of the mPAF materials with different tetrahedral monomers were studied by nitrogen adsorption at 77 K. Figure 3.25 shows nitrogen adsorption–desorption isotherms and pore distribution of the materials pre-treated at 150°C for 18h.

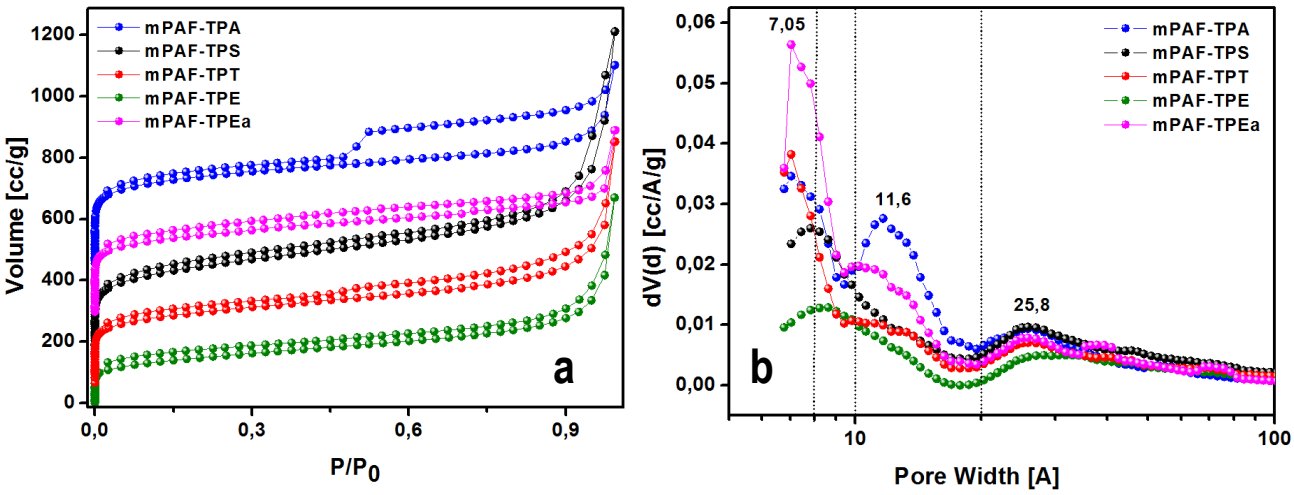

Figure 3.25. (a) Nitrogen adsorption–desorption isotherms measured at 77 K, and (b) pore size distributions calculated from NLDFT of mPAF materials with different tetrahedral monomers. Isotherms are shifted with respect to the y axis.

As shown in the nitrogen adsorption–desorption isotherms (Figure 3.25a) the mPAF materials exhibit sharp uptakes at low relative pressures, indicating the existence of micropores in their networks. Distinct hysteresis loops in the desorption branches can be observed for all samples, which is characteristic of the presence of mesopores. Table 6 summarizes the BET surface area and pore volume of the mPAF materials.

Table 3.6. BET surface area and total pore volume at P/P_0=0.995 derived using NLDFT method.

Sample	SSA BET (m^2/g)	Total Pore volume (cc/g)	Micropore volume		
			<10Å	10<Å<20	Total
mPAF-1/16	1314	0,83	0,11	0.10	0.21
mPAF-TPA	1115	0,885	0,14	0,15	0,29
mPAF-TPE	525	0,826	0,054	0,031	0,085
mPAF-TPS	1000	1,366	0,11	0,07	0,18
mPAF-TPT	831,91	0,985	0,13	0,06	0,19
mPAF-TPEa	961,59	0,762	0,14	0,10	0,24

Compared to mPAF-1/16, a small reduction in the BET surface areas can be seen in all samples: 1115 m^2/g for mPAF-TPA, 1000 m^2/g for mPAF-TPS, 961,59 m^2/g for mPAF-TPEa and 831,91 m^2/g for mPAF-TPT. The material mPAF-TPE shows a much lower surface area of 525 m^2/g if compared with the other polymers.

The pore size distributions reported in the figure 3.25b were calculated by non-local density functional theory (NLDFT), applied on silica surface with cylindrical pores. The method chosen was the one that gave the smallest fitting error. Even if these materials were formed by different precursors, there are mainly three families of pores distribution: a predominant size at ca. 7Å, a small family centred at ca. 12 Å and pores at ca. 25 Å suggesting the presence of a small amount of mesopores. The total pore volume for all materials is very high ranging between 0,762 and 1,37 cc/g.

3.3.5 Friedel-Crafts reaction optimization: preliminary characterizations

In the previous sections of this chapter, Friedel-Crafts reactions were studied by changing TPM and FDA ratio to obtain a tuning of the porosity (i.e. of the pore size distribution). The same synthesis has been applied on other tetrahedral precursors (TPA, TPS, TPT, TPE and TPEa) that gave polymers with suitable porosity for CO_2, CH_4 and H_2 storage. Treatments at high temperatures of the polymer mPAF-1/16 have shown that both the specific surface area and porosity of the polymer can be further improved.

The synthesis conditions have been optimized, as claimed in patent [21] and published in ref 22, by using different TPM:FDA ratios that led to polymers with surface area higher than 1200 m^2/g and porosity suitable for the gas storage. Moreover, great improvements of the textural properties of the materials were obtained by changing the precursor concentration and by applying a post synthesis thermal treatment.

Some of the results obtained starting from the procedure reported previously for the synthesis of HCP materials, and modified using the precursor either in high concentration (0.2 M) or more diluted (0.02 M), will be described in this section. These conditions have led to materials with different textural properties, which can be further improved and modified after thermal treatment at 380°C for 18 h under N_2 flow. As a result, not only the surface area and the total pore volume changed, but also the pore size distribution.

In particular, the following materials will be described:

- mPAF-1/8 obtained by concentrations of TPM in DCE of 0.2M (mPAF-1/8 conc) and 0.02M (mPAF-1/8 dil), respectively. After the synthesis both materials were treated at 380 °C (mPAF-1/8 conc@380°C and mPAF-1/8 dil@380°C);

- mPAF-1/16 obtained by 0.2 M concentration of TPM in DCE (mPAF-1/16 conc) and subsequently treated at 380°C (mPAF-1/16 conc@380°C)
- mPAF-1/40 obtained by 0.2 M concentration of TPM in DCE (mPAF-1/40 conc) and subsequently treated at 380°C (mPAF-1/40 conc@380°C)
- mPAF –TPE (the synthesis is reported in section 3.3.4) after thermal treatment at 380 °C (mPAF–TPE@380°C)

Note that TPM:FDA ratios of 1:8 and 1:40 were also tested to demonstrate that a microporous polymer can be obtained adopting a wider range of reaction conditions. The mPAF-TPE material was also thermally treated to 380 °C to verify if the textural properties of this polymer can be improved similarly to the systems obtained from TPM. The materials were preliminary characterized by using FTIR, TGA and nitrogen physisorption at 77K techniques.

3.3.5.1 Infrared spectroscopy (FTIR)

The Fourier transform infrared (FTIR) spectra of the samples are shown in figure 3.26.

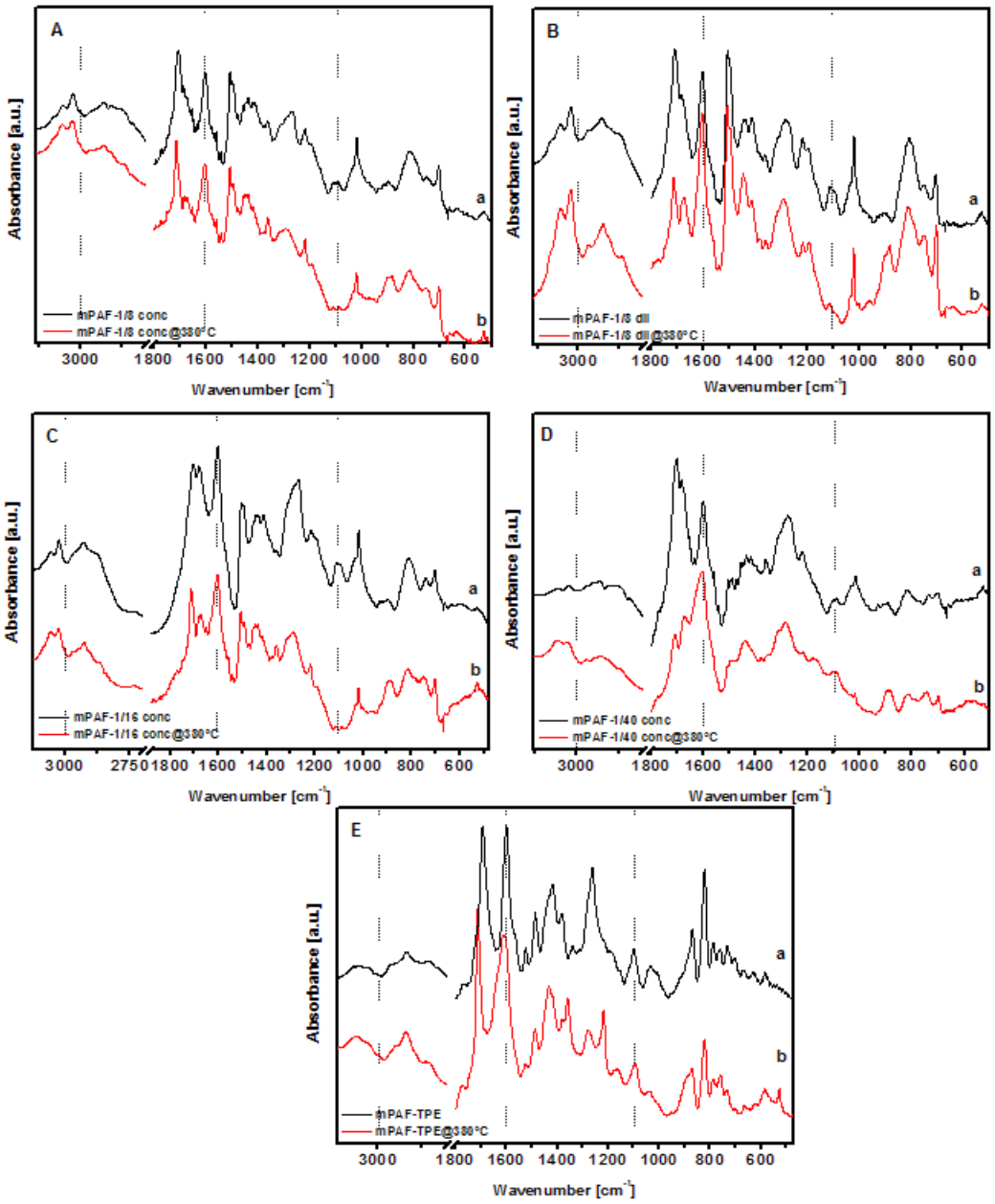

Figure 3.26. FTIR spectra of the mPAF materials before (black lines) and after (red lines) thermal treatment at 380°C, recorded as KBr pellets in the 3200-500 cm^{-1} frequency range: mPAF-1/8 conc and mPAF-1/8 conc@380°C (A), mPAF-1/8 dil and mPAF-1/8 dil@380°C (B), mPAF-1/16 conc and mPAF-1/16 conc@380°C (C), mPAF-1/40 conc and mPAF-1/40 conc@380°C (D) and mPAF -TPE @380°C and mPAF-TPE @380°C (E). The material before and after the thermal treatment are indicated with letter (a) and (b), respectively.

FTIR spectra show that the mPAF samples both with different precursor concentrations and different TPM:FDA ratios are characterized after thermal treatment at 380 °C by changes similar to those of the sample mPAF-1/16 discussed in the section 3.3.2. In particular, the band of the methyl groups at 2075 cm^{-1}, the ether group at 1100 cm^{-1}, the substitution of the aromatic rings at 1710, 1670 and 1269 cm^{-1}, decrease in their

intensity after the treatment at 380°C. As discussed before, these bands could be due to FDA fragments and side products trapped in the pores. However, to assign with certainty these groups further investigations using the GCMS technique are underway.

3.3.5.2 Thermogravimetric analysis (TGA)

TGA analyses were performed to evaluate how the thermal decomposition of the materials changes after treatment at 380 °C (Figure 3.27). All the TGA profiles were recorded under argon atmosphere with a heating ramp of 2°C/min up to 800 °C.

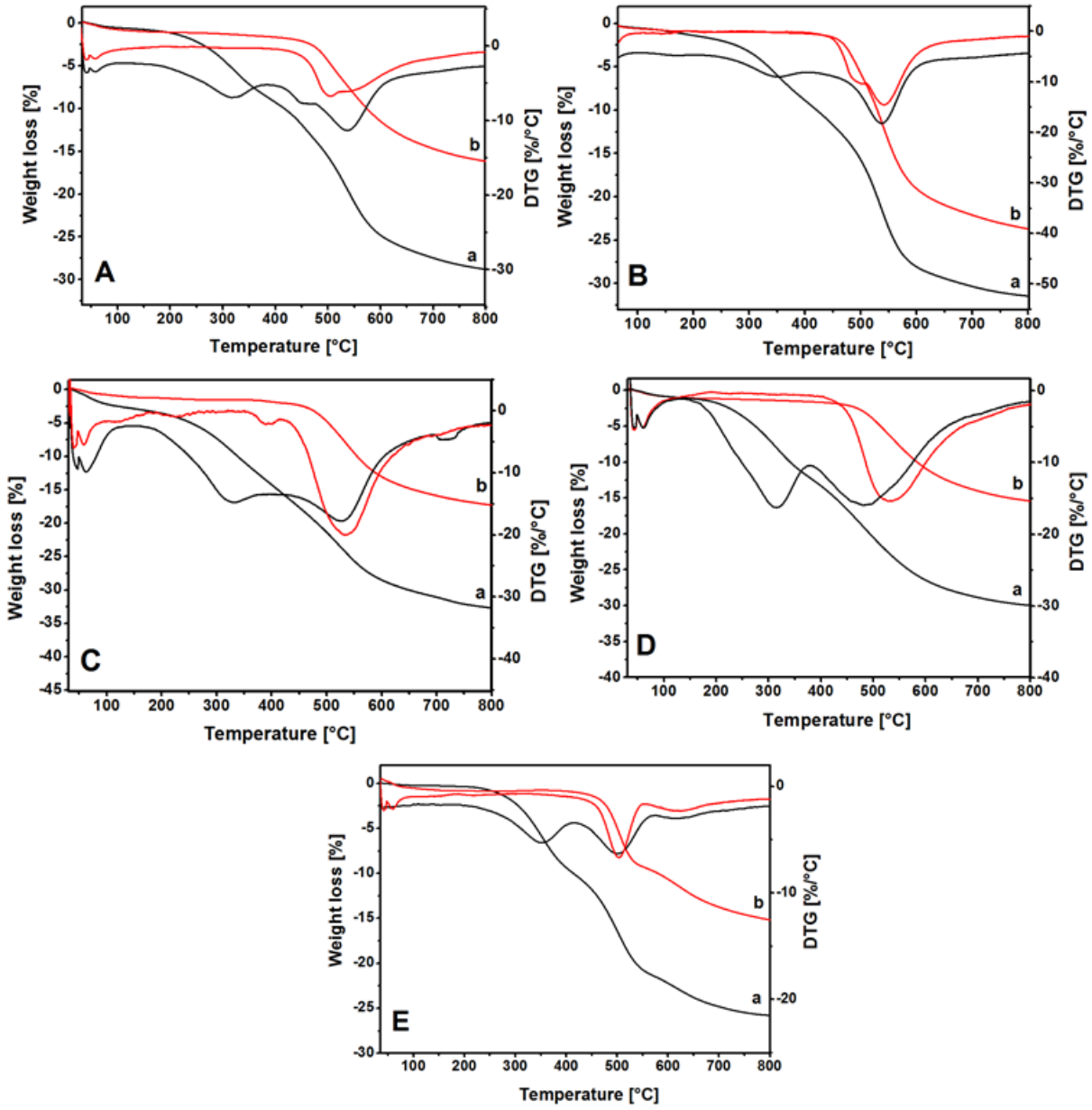

Figure 3.27. TGA analysis of the mPAF materials before and after thermal treatment at 380°C: mPAF-1/8 conc and mPAF-1/8 conc@380°C (A), mPAF-1/8 dil and mPAF-1/8 dil@380°C (B), mPAF-1/16 conc and mPAF-1/16 conc@380°C (C), mPAF-1/40 conc and mPAF-1/40 conc@380°C (D) and mPAF -TPE @380°C and mPAF-TPE @380°C (E). The materials before and after the thermal treatment are indicated with letter (a) and (b), respectively.

TGA analysis show that the mPAF samples with different precursor concentration and before thermal treatment are characterized by the presence of two separated weight losses: the first due to FDA fragments and side products trapped in the pores and the second due to the framework decomposition. The weight loss percentages are summarized in table 3.7.

After thermal treatment, all samples show only one weight loss due to structure decomposition, approximately at the same temperature of the second weight loss observed in the materials before thermal treatment. This behavior demonstrates the complete removal of the trapped organic species in the porous structure. TGA data indicate that the thermal treatment at 380°C allows cleaning the surface of the mPAF materials.

Table 3.7. Summary of the percentage of the weight losses of the mPAF samples before and after the thermal treatments.

Sample	Weight loss (%) T (150-400)	Weight loss (%) T (400-800)
mPAF-1/8- dil	6,17	14,25
mPAF-1/8- dil@380°C	--	19,64
mPAF-1/8- conc	7,95	10,05
mPAF-1/8- conc@380°C	--	11,89
mPAF-1/16- conc	7,56	11,56
mPAF-1/16- conc@380°C	--	13,17
mPAF-1/40- conc	10,19	7,62
mPAF-1/40- conc@380°C	--	12,36
mPAF-TPE	9,53	6,21
mPAF-TPE@380°C	--	4,4

3.3.5.3 N_2 physisorption at 77K

The textural analysis of the mPAF samples before and after thermal treatments was made by N_2 physisorption at 77K, with relative pressures (P/P_0) from $1x10^{-7}$ to 1. Before the analysis, the samples were outgassed at 150°C for 18 hours. The BET surface areas were calculated over a relative pressure range of 0.05−0.15, and pore size distributions were calculated using nonlocal density functional theory (NLDFT) on silica surface with cylindrical geometry applied to the adsorption branch.

The physisorption isotherms (frames A) and pore size distributions (frames B) for mPAF samples before (black circles) and after (red triangles) thermal treatment at 380°C are reported in figures 3.28–3.32.

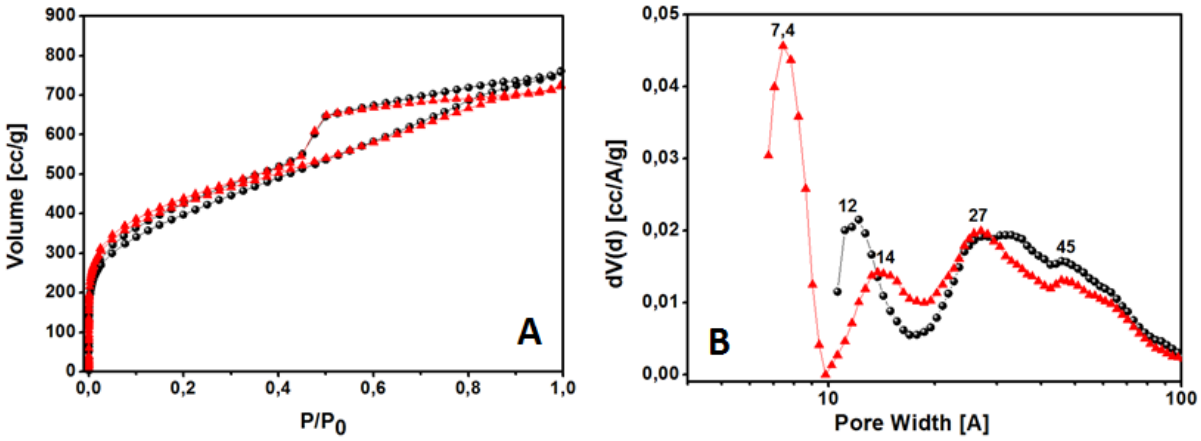

Figure 3.28. N_2 adsorption-desorption isotherms at 77K (A) and pore size distribution (B) of mPAF-1/8 conc (black circles) and mPAF-1/8 conc@380°C (red triangles) samples.

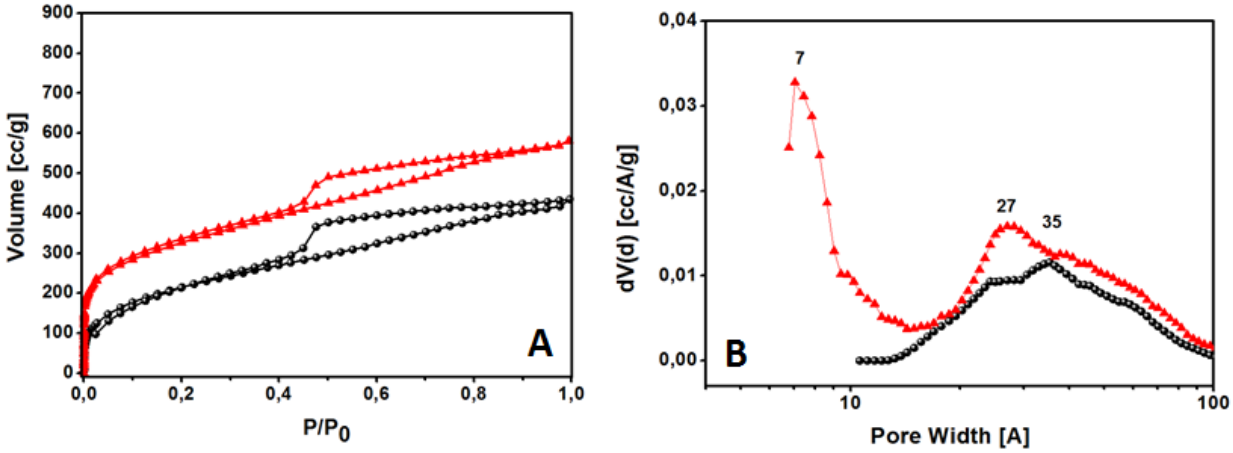

Figure 3.29. N_2 adsorption-desorption isotherms at 77K (A) and pore size distribution (B) of mPAF-1/8 dil (black circles) and mPAF-1/8 dil@380°C (red triangles) samples.

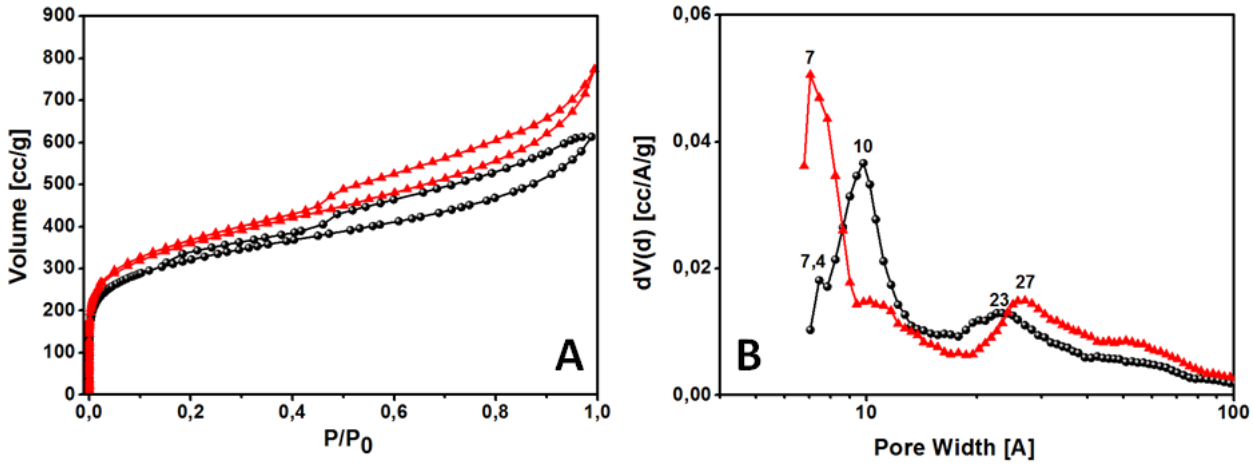

Figure 3.30. N_2 adsorption-desorption isotherms at 77K (A) and pore size distribution (B) of mPAF-1/6 conc (black circles) and mPAF-1/6 conc@380°C (red triangles) samples.

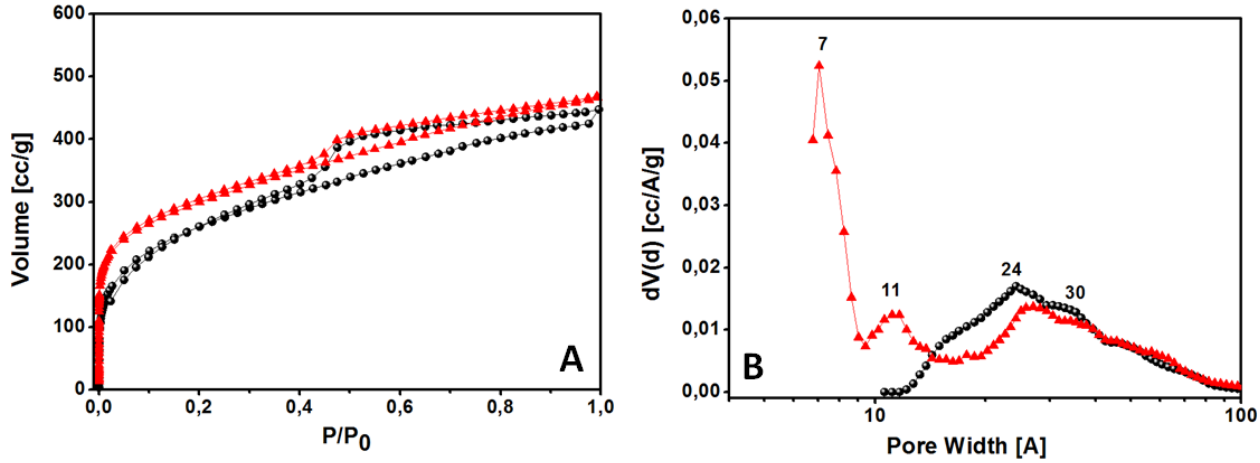

Figure 3.31. N_2 adsorption-desorption isotherms at 77K and relative pressures (P/P_0) from $1x10^{-7}$ to 1 (A) and pore size distribution (B) of mPAF-1/40 conc (black circles) and mPAF-1/40 conc@380 (red triangles) samples.

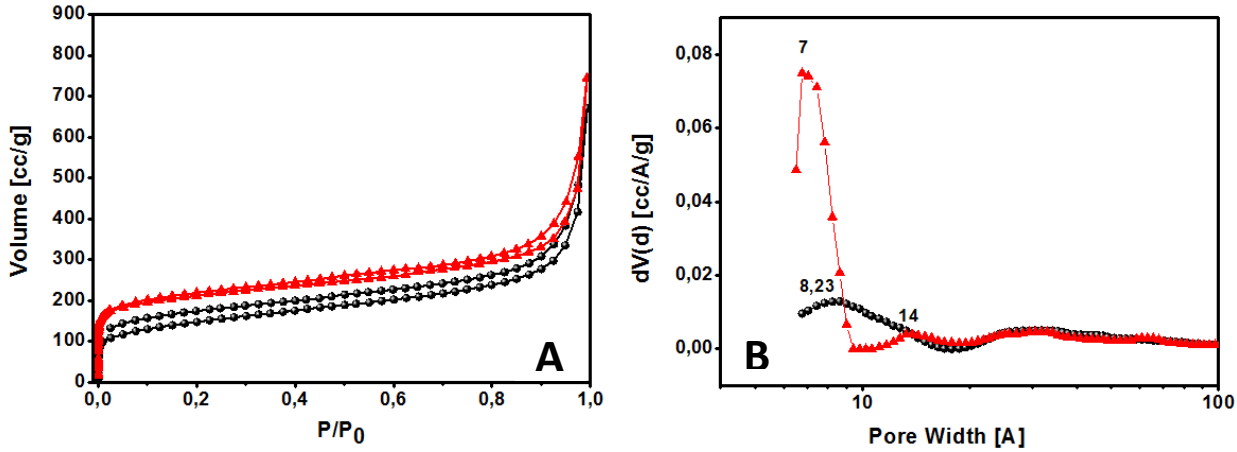

Figure 3.32. N_2 adsorption-desorption isotherms at 77K (A) and pore size distribution (B) of mPAF-TPE (black circles) and mPAF-TPE@380°C (red triangles) samples.

All isotherms show large quantities of gas (100-300 cm^3/g) adsorbed at low relative pressures, as expected for microporous materials. They also display a further gradual filling of mesopores at higher relative pressures, in the range 0.45-1 P/P_0. The porous properties of the polymers are summarized in table 3.8, where it can be seen that the BET surface areas range between 525 and 1527,66 $m^2\ g^{-1}$. It should be noted that the thermal treatment at 380 °C always leads to an improvement of the BET surface area of the individual polymers.

Table 3.8. Composition, temperature treatments, surface properties and pore volume of mPAF samples.

Sample	Precursor	precursor:FDA (mol)	precursor conc in DCE (M)	Temperature treatment (°C)	SSA $_{BET}$[a] [m^2/g]	V $_{TOTAL}$[b] [cc/g]	V $_{MICRO}$[c] [cc/g]		
							<10Å	10<Å<20	Total
mPAF-1/8 dil	TPM	1:8	0.02	150	1434,66	1,116	--	0,133	0,133
mPAF-1/8 dil@380°C	TPM	1:8	0.02	380	1527,66	1,074	0,128	0,099	0,227
mPAF-1/8 conc	TPM	1:8	0.2	150	792,55	2,26	--	0,019	0,019
mPAF-1/8 conc@380°C	TPM	1:8	0.2	380	1170,202	0,861	0,10	0,053	0,153
mPAF-1/16 conc	TPM	1:16	0.2	150	1169,41	0.903	0.062	0.148	0.21
mPAF-1/16 conc@380°C	TPM	1:16	0.2	380	1292.77	1.12	0.13	0.09	0.22
mPAF-1/40 conc	TPM	1:40	0.2	150	947,752	1,49	--	0,06	0,06
mPAF-1/40 conc@380°C	TPM	1:40	0.2	380	1073,50	0,696	0,122	0,07	0,192
mPAF-TPE	TPE	1:16	0.02	150	525	0,826	0,054	0,031	0,085
mPAF-TPE@380°C	TPE	1:16	0.02	380	776,64	0,948	0,187	0,023	0,21

a) Surface area calculated from the nitrogen adsorption isotherm using the BET method; b) Total pore volume at P/P_0=0.995; c) The micropore volume is determined using NLDFT method.

After thermal treatment, most of the samples underwent a change of pores distribution leading to the appearance of small micropores of about 7Å. These results show that the treatment at 380 °C, a temperature at which the framework is maintained, leads to an increase in BET surface area, pore volume and microporsity of the samples, all parameters greatly important for the optimization of the gas storage capacity of the porous materials.

3.4 Conclusions

In this chapter the synthesis of different HCP polymers obtained from the $FeCl_3$ catalysed Friedel-Crafts reaction between aromatic tetrahedral monomers and formaldehyde dimetil acetal (FDA) was reported. Starting from tetraphenylmethane (TPM) monomer, the polymer with the highest surface area and pore volumes was synthesised with a TPM:FDA ratio of 1:16: the material named mPAF-1/16 is characterized by a surface area 1314 m^2/g of and pore volume of 0,83 cc/g. This material was then modified using both thermal treatments and amine functionalization. Thermal treatments enhanced both surface area and total micropore volume, whereas the amine functionalization caused a decrease in the porous properties, due to the inclusion of the new groups. However, the introduction of amino groups increased the gas storage capacity, as will be described in the next chapter.

Using the optimized reaction conditions, several polymers were formed starting from precursors with different tetrahedral centres: materials with high surface areas and high microporous volume characterized by the predominance of pores of size > 10 Å were obtained.

With further optimization of the HCP synthesis, it is seen that not only the different precursor : FDA ratio claimed in the patent [21] leads to a good surface area and porosity suitable for the gas storage, but the combined effect of the amount of solvent (i.e. precursors concentration) and the heat treatment after synthesis, lead to a great improvement of the porosity of the material, which is more suitable for the gas storage of carbon dioxide, hydrogen and methane.

The storage properties of some materials described in this chapter will be discussed in chapter 4.

References:

[1] Wood, C. D.; Tan, B.; Trewin, A.; Niu, H.; Bradshaw, D.; Rosseinsky, M. J.; Khimyak, Y. Z.; Campbell, N. L.; Kirk, R.; Stöckel, E. et al. Hydrogen Storage in Microporous Hypercrosslinked Organic Polymer Networks. *Chem. Mater.* **2007**, *19*, 2034-2048.

[2] Xu, S.; Luo, Y.; Tan, B. Recent Development of Hypercrosslinked Microporous Organic Polymers Macromol. *Rapid Commun.* **2013**, *34*, 471−484.

[3] Luo, Y.; Li, B.; Wang, W.; Wu, K.; Tan, B. Hypercrosslinked Aromatic Heterocyclic Microporous Polymers: A New Class of Highly Selective CO2 Capturing Materials. *Adv. Mater*. **2012**, *24*, 5703–5707.;

[4] Dawson, R.; Ratvijitvech, T.; Corker, M.; Laybourn, A.; Khimyak, Y.A.; Cooper, A. I.; Adams, D. J. Microporous Copolymers for Increased Gas Selectivity. *Polym. Chem.* **2012**, *3*, 2034–2038.

[5] Li , B.; Gong, R.; Wang, W.; Huang, X.; Zhang, W.; Li, H.; Hu, C.; Tan, B. A New Strategy to Microporous Polymers: Knitting Rigid Aromatic Building Blocks by External Cross-Linker. *Macromolecules* **2011**, *44*, 2410-2414.

[6] Dawson, R.; Stöckel, E.; Holst, J.R.; Adams, D. J.; Cooper, A. I. Microporous Organic Polymers for Carbon Dioxide Capture. *Energy Environ. Sci.* **2011**, *4*, 4239-4245

[7] Lu, W. G.; Yuan, D. Q.; Zhao , D.; Schilling, C. I.; Plietzsch, O.; Muller, T.; Brase, S.; Guenther, J.; Lumel, J.; Krishna, R. et al. Porous Polymer Networks: Synthesis, Porosity, and Applications in Gas Storage/Separation. *Chem. Mat.* **2010**, *22*, 5964-5972

[8] Luo, Y.; Zhang, S.; Ma, Y.; Wang, W.; Tan, B. Microporous Organic Polymers Synthesized By Self-Condensation of Aromatic Hydroxymethyl Monomers. *Polym. Chem*. **2013**, *4*, 1126-1131

[9] Colthup, N.B.; Daly, L.H.; Wiberley, S.E. *Introduction to Infrared and Raman Spectroscopy*; Academic Press: New York, US, 1964.

[10] Law, R. V.; Sherrington, D. C.; Snape, C. E. Solid-State C MAS NMR Studies of Hyper-Cross-Linked Polystyrene Resins. *Macromolecules* **1996**, *29*, 6284-6293

[11] Williams, D.J.; Colquhoun, H.M.; O'Mahoney, C.A. The Structure of Poly(M-Phenylene): a Prediction From Single-Crystal X-Ray Studies of M-Deciphenyl and M-Undeciphenyl. *J. Chem. Soc., Chem Commun*. **1994**, 1643-1644

[12] Chen, Z.; Deng, S.; Wei, H.; Wang, B.; Huang, J.; Yu, G. Activated carbons and amine-modified materials for carbon dioxide capture: a review. *Front. Environ. Sci. Eng.* **2013**, 7, 326–340.

[13] Yorgun, S.; Vural, N.; Demiral, H. Preparation of high-surface area activated carbons from Paulownia wood by $ZnCl_2$ activation. *Microporous and Mesoporous Materials* **2009**, 122, 189–194.

[14] Lu, A-H.; Dai, S. *Porous Materials for Carbon Dioxide Capture*; Springer: Heidelberg, DE, **2014**.

[15] Sevilla, M.; Valle-Vigo´ n, P.; Fuertes, A. B. N-Doped Polypyrrole-Based Porous Carbons for CO_2 Capture. *Adv. Funct. Mater.* **2011**, 21, 2781–2787.

[16] Srinivas, G.; Burress, J.; Yildirim, T. Graphene oxide derived carbons (GODCs):synthesis and gas adsorption properties. *Energy Environ. Sci.* **2012**, 5, 6453–6459.

[17] Li, Y.; Ben, T.; Zhang, B.; Fu, Y.; Qiu, S. Ultrahigh Gas Storage both at Low and High Pressures in KOH-Activated Carbonized Porous Aromatic Frameworks. *Scientific Reports*, **2013**, *3*, 2420.

[18] Lu, W.; Sculley, J.P.; Yuan, D.; Krishna, R.; Wei, Z.; Zhou, H.-C. Polyamine-Tethered Porous Polymer Networks for Carbon Dioxide Capture from Flue Gas. *Angew. Chem. Int. Ed.* **2012**, 51, 1 – 6.

[19] Wang, Q.; Luo, J.; Zhong, Z.; Borgna, A. CO_2 capture by solid adsorbents and their applications: current status and new trends. *Energy Environ. Sci.* **2011**, 4, 42.

[20] Jiang, Z.-M.; Li, A.; Cai, J.; Wang, C.; Zhang, Q. Adsorption of phenolic compounds from aqueous solutions by aminated hypercrosslinked polymers. *Journal of Environmental Sciences* **2007**,19, 135–140.

[21] Patent: "A porous organic polymer capable of adsorbing gas and the method of preparing thereof"; Applicant: SOL S.p.A., et al.; Inventors: Errahali M., Gatti G., Tei L., Cossi M., Marchese L. European application 13425105.7(**2013**); PCT International extension rif. E0094969 (**2014**).

[22] Errahali, M.; Gatti, G.; Tei, L.; Paul, G.; Rolla, G. A.; Canti, L.; Fraccarollo, A.; Cossi, M.; Comotti, A.; Sozzani, P.; Marchese, L. Microporous Hyper-Cross-Linked Aromatic Polymers Designed for Methane and Carbon Dioxide Adsorption. *J. Phys. Chem. C* **2014**, 118, 28699–28710.

CHAPTER 4

Experimental and theoretical gas adsorption on the synthesized polymers

4.1 Introduction

In the previous chapters the synthesis and characterization of various materials belonging mainly to two classes of porous organic materials were discussed: Porous Aromatic Framework (PAFs) and Hyper-crosslinked polymers (HCPs). All the polymers show a good chemical and thermal stability, with a pore distribution characterized by a predominant microporsity.

It is well established that CH_4, H_2 and CO_2 adsorb and fill the microporosity at low pressure. Gas sorption is a very important part of the physical characterization for insoluble porous polymer networks and it gives an indication of the applicability of the materials for different fields such as energy applications (e.g. on-board storage of H_2 and CH_4 for transportation technologies) or for environmental purposes (e.g. carbon dioxide capture).

The storage of these three gases normally requires materials with high surface area and high pore volume, which has to be microporous. Optimal storage capacity will occur when the fraction of micropores is maximized, with no void or macropore volume. The micropores, have a size lower than 20 Å and, according to the IUPAC definition, they are in turn classified into two groups, i.e. the ultramicropores (lower than 7 Å) and the supermicropores (from 7 to 20 Å).

The micropores are important for the gas storage due to the overlap of the potential fields from both sides of the pore walls. They are characterized by higher affinity towards gases and thus higher uptake capacity comparing to pores with larger diameter [1]. As a consequence, it has been demonstrated that there is a reliable correlation between gas adsorption capacities and the porous texture of porous materials: CO_2 and H_2 storage requires narrow micropore volume (< 7 Å) [2], while for CH_4 micropores with a pore size around 11 Å are more relevant [3, 4.]. In general, it was found a correlation with the total micropore volume, including both the ultramicroporosity (size lower than 0.7 nm) and supermicroporosity (size between 0.7–2.0 nm) [5]. In particular for methane, a low amount of mesoporosity is also desirable. The presence of low mesoporosity in the form of feeder pores with size lower than 50 Å is required to some extent in order to provide easy access for the adsorbate molecules to/from the micropores [6].

The suitability of an adsorbent for gas storage application can be evaluated from two different points of view: (i) based on its capacity on a gravimetric basis (adsorption per gram of adsorbent), where textural properties (surface area, porosity and pore size distribution) are mainly the parameters that control the adsorption [7, 8, 9] or (ii) depending on its capacity per liter of adsorbent (on a volumetric basis, the most suitable way to express the results from a storage application point of view), in which not only the textural properties but also the density can affect the gas uptake [3, 10, 11].

Another important relationship between pore size and gas storage pressure should be taken in consideration: narrow pores are important to store gas at low pressures, since, when the pressure is low, it is necessary to have greater host-guest interactions between gas molecules and pore walls. On the other hand, in case of high pressures, pores with large diameter, and thus high surface area and large pore volume, become very important.

The capacity storage reported in this thesis is also supported by computational predictions, which are the main subject of the work that the PhD student Dr. Lorenzo Canti (Supervisor Prof. Maurizio Cossi) is doing in my own Department. In this chapter, the comparison between experimental and computational results on the storage capacity of selected materials will be shown. For the simulations, a Grand Canonical Monte Carlo (GCMC) algorithm was used.

This chapter describes the experimental and computational gas uptake of selected synthesized materials, at different temperatures and pressures. In particular, the research work was focused on:

- The evaluation of the pore distribution obtained from argon adsorption at 87K of the materials PAF-302 and mPAF-1/16, to obtain a more reliable characterization of the microporsity of these materials. The experimental measurements were compared with those obtained from computational results, made on optimized structures.
- The storage of CH_4 (298K) and H_2 (77K) at high pressure (up to 200 bar) on the material PAF-302, which showed the highest surface area and pore volume among the materials synthesized in this thesis work.
- The CH_4 and CO_2 uptake at different temperatures and pressures up to 10 bar on the series of mPAF-1/n materials characterized by small micropores as shown in Chapter 3. These data were published in ref .12.
- The CO_2 adsorption at low pressure (max 0,1 bar) and 35°C on almost all materials, to evaluate the interaction between the framework and the adsorbed CO_2.

The aims of this PhD thesis are: 1) to synthesize different materials using Yamamoto and Friedel-Crafts reactions; 2) to understand which synthetic strategy and precursor give materials with good porosity

properties; and 3) the relationship between the porosity and the gas storage capacity, which is important to test their real application. The gas storage experiments are, however, time-consuming and necessitate different instruments to carry out the analysis and, thus, only the most promising materials, in terms of gas sorption, were analyzed.

Different research groups have collaborated to the gas uptake measurements: i) Dr. M. Thommes of the Quantachrome instruments measured the Argon physisorption along with methane and hydrogen uptake at high pressure; ii) Prof. A. Comotti of the University of Milano "Bicocca" was involved in the methane and carbon dioxide adsorption at low pressure on the series of mPAF-1 / n materials; and iii) Prof. S. Brandani of the University of Edinburgh collaborated to the CO_2 adsorption at low pressure (0,1 bar) and at 35°C.

4.2 PAF-302: Experimental and theoretical gas adsorption

The synthesis and the optimization of the PAF-302 led to a material with a surface area of 4293 m^2/g: the modification of the synthetic method by microwave assistance and in situ catalyst formation led to two similar materials but with lower surface area.

Before considering the storage capacity, we focus more in detail on the structure of PAF-302, originally proposed by Ben et al. [13] and later by our group [14].

PAFs can be modeled starting from the diamond structure, and replacing each C−C covalent bond with one or more phenyl rings. As illustrated in figure 4.1, the resulting solids maintain the tridimensional structure of diamond (though lowering the local symmetry to P1 group) with a huge increase of the empty space inside the aromatic backbone, where a network of micro- or mesopores is formed. More details on structural and textural properties of crystalline PAF-302 model can be found in the ref.14.

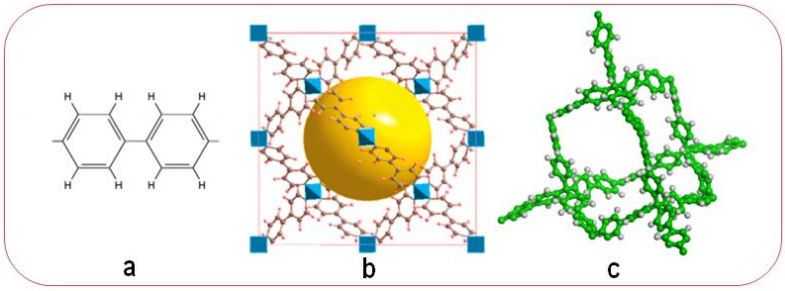

Figure 4.1. Representation of the PAF-302 unit cell from aromatic building block between tetrahedral carbons (a), tridimensional structure of the unit cell where the yellow sphere denotes the pores in 3D PAF-302 (b) and skeletal volume defined as a collection of atomic spheres by the GEPOL procedure (c).

The computational adsorption isotherms of Ar (87 K), CH_4 (298K) and H_2 (77K) were simulated with Monte Carlo technique and compared to the corresponding experimental isotherms.

The simulations were performed with a purposely adapted force field: PCFF and DREIDING force fields were used for methane and hydrogen, respectively, whereas for methane adsorption we used previously optimized PCFF force field [14].

For Ar, we used an adapted version of PCFF force field [15]; argon parameters were slightly modified to reproduce the free gas density [16] at 87 K in the 0−1 bar pressure range. The details of the optimized method are reported in ref .12.

4.2.1 Specific surface area and pore volume determination by Argon physisorption

The porosity of PAF-302, using N_2 physisorption at 77 K, was evaluated and discussed in Chapter 2.

Traditionally, the pore size distribution of a porous solid is evaluated from the analysis of nitrogen adsorption isotherms measured at 77 K, this is the approach used for all samples in this thesis to compare them with the data reported in the literature. It is well known, however, that the use of nitrogen for the characterization of microporous materials has some drawbacks [17]:

- The filling of micropores with dimensions of 0.5-1 nm occurs at very low relative pressures ($P/P_0 = 10^{-7} – 10^{-5}$). In this low pressure regime, the rates of diffusion and equilibration are very slow. At ~87 K, Argon fills micropores of dimensions 0.5-1 nm at higher relative pressures (10^{-5} to 10^{-3} torr) leading to faster equilibration and, subsequently, reduction of analysis time.
- Compared to nitrogen, argon adsorption reveals a much more straightforward correlation between pore size and the pressure at which micropores are filled: while nitrogen is a diatomic molecule with a quadrupole moment which may produce specific interactions at the gas–solid interface, argon has no dipole or quadrupole moment and is much less interacting with the solid, allowing to provide a more accurate description of the porous structure of a material.

For these reasons, in order to obtain much more accurate data of pore distribution, Ar physisorption measurement at 87 K was carried out on PAF-302.

In figure 4.2, the comparison between the experimental and theoretical isotherms (frame A) and pore distributions (B frame) are shown. Table 4.1 summarizes the comparison between experimental and computational data of porosity obtained by argon physisorption.

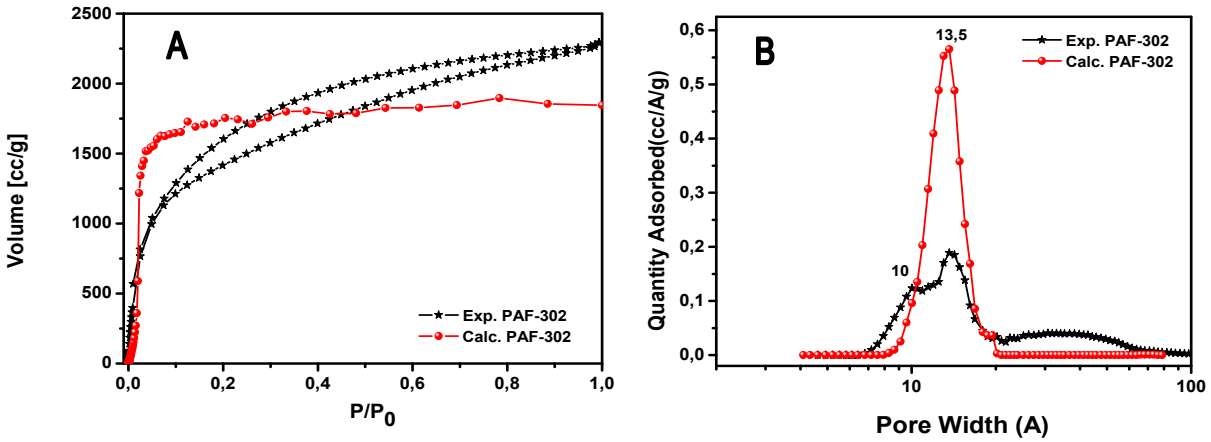

Figure 4.2. Experimental (black stars) and theoretical (red spheres) Ar physisorption at 87K on PAF-302: isotherms (A) and pore distributions (B) obtained applying NLDFT model on zeolites/silica surface with cylindrical pore geometry.

Applying the multipoint BET method in the range 0,049-0,2 P/P_0, the experimental specific surface area was 4563 m^2/g, a somehow lower value that that reported by Ben et al. [13]. The computational curve obtained on a perfectly crystalline system gives a value of 5500 m^2/g, and this suggests that the material synthesized in our lab has some defects in the framework, i.e. it is not perfectly crystallized.

The calculated isotherm has a Langmuir profile with only micropores, as expected from the simulated structure model. The experimental curve also shows a Langmuir-type profile, however the saturation is reached much more progressively and only at P/P_0 close to 1. This is a clear indication that both micropores and mesopores are present in our material: indeed, the mesoporosity leads to a hysteresis loop in the desorption branch which closes only at very low pressures. This type of hysteresis is also found in the nitrogen adsorption/desorption isotherms at 77K.

Table 4.1. Theoretical and experimental textural data obtained from Ar physisorption at 87K.

Sample	SSA BET (m^2/g)	Total Pore volume (cc/g)	Micropore volume		
			<10Å	10<Å<20	Total
Exp. PAF-302	4562.87	2.89	0.16	1.1	1.26
Calc. PAF-302	5500	2.48	0.044	2.41	2.45

The pore sizes were calculated using the non-local density function (NLDFT) applied on zeolite / silica surface with cylindrical pore geometry. Even in the case of argon adsorption, the model chosen is the one that gave the lower fitting error.

Looking at the pore size distribution (figure 4.2B), it can be seen that the theoretical curve (red spheres) presents mainly a single family of micropores at 13.5 Å, while the experimental curve (black stars) shows the main family of pores at 13.5 Å with a shoulder at 10 Å which represents 13% of the micropores (table 4.1). The small difference in the pore size between calculated and experimental results is due to the fact that at the theoretical level an ideal structure is considered, while the synthesized material is characterized by a defective structure with two families of micropores and a small part of mesopores. The experimental total pore volume (2.89 cc/g) is higher than the theoretical value (2.48 cc/g), due to the presence of mesopores in the synthesized material, whose fraction is ca. 66% of the total volume, whereas in the ideal structure practically all empty space is due to micropores.

Another interesting comparison is between the pore distribution obtained from nitrogen and argon adsorption isotherms at 77 and 87K respectively (figure 4.3).

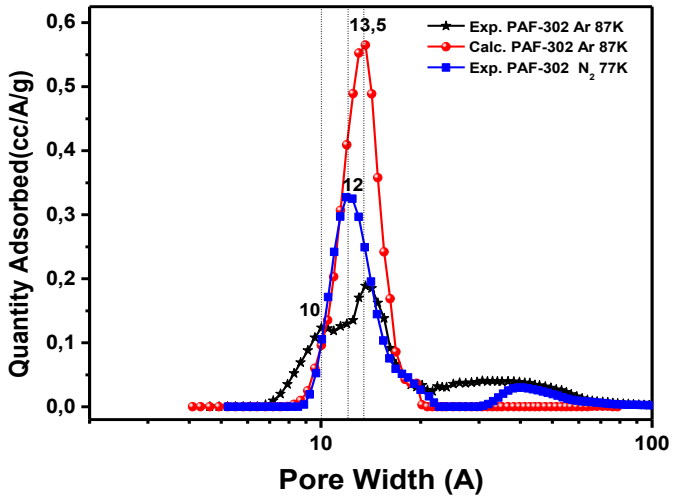

Figure 4.3. Pore distribution of PAF-302 from nitrogen (77K) and argon (87K) adsorption isotherms.

The pore distribution obtained from nitrogen adsorption has a single family of pores centered at 12 Å, which seems as an average value between 10 Å and 13.5 Å determined with argon isotherm.

The comparison between the nitrogen and argon measurements showed the reliability of results from nitrogen physisorption in this case. This was expected since nitrogen measures reliably the supermicropores, as reported in literature [17].

The exceptionally high surface area and pore volume combined with an excellent stability make PAF-302 a very attractive candidate for gas storage applications, particularly for H_2 and CH_4 storage for on-board mobile applications.

4.2.2 Experimental and theoretical high-pressure CH_4 and H_2 adsorption isotherms

To evaluate gas storage capacity of PAF-302, high-pressure excess adsorption of hydrogen at 77 K and methane at 298 K up to 200 bar were measured. The hydrogen adsorption on PAF-302 is an exothermic process due to weak van der Waals interactions, which lead to very low heat of adsorption in the range 3 to 10 kJ mol^{-1}. So, to obtain significant amounts of H_2 uptake, the measurement is usually performed at 77 K, the boiling temperature of liquid nitrogen [18].

The gas uptake capacity can be defined as excess, absolute, and effective adsorption [19, 20].

- ✓ The absolute adsorption is the total amount of gas introduced into the sample cell minus the amount outside the sample in the gas phase; thus, it accounts for the total amount of adsorbate molecules residing into the pores.
- ✓ The excess adsorption is the absolute amount of gas contained in the sample pores minus the amount of gas that would be present in the pores in the absence of gas-solid intermolecular forces (thus expressing the excess gas that is adsorbed due to the gas/adsorbent interactions).
- ✓ The effective adsorption is the amount of gas stored in a container with the adsorbent minus the amount of gas that can be stored in the same container without any adsorbent.

The evaluation of excess uptake in a volumetric or gravimetric gas adsorption is a common practice in the literature and it is normally used to compare adsorption properties of microporous materials.

While the absolute adsorption capacity for a type I isotherm reaches the saturation value at high pressures and then remains constant, the excess adsorption isotherm does not possess a plateau at high pressure but a maximum and with further increase of hydrogen pressure the excess uptake decreases. This is happening because the gas saturates the pores but at the same time the external gas density is further increasing. The excess adsorption is zero when the gas density and the adsorbed density are equal.

In figure 4.4, the simulated and experimental adsorption isotherms of CH_4 adsorbed on PAF-302 at 298 K and up to 200 bar are reported.

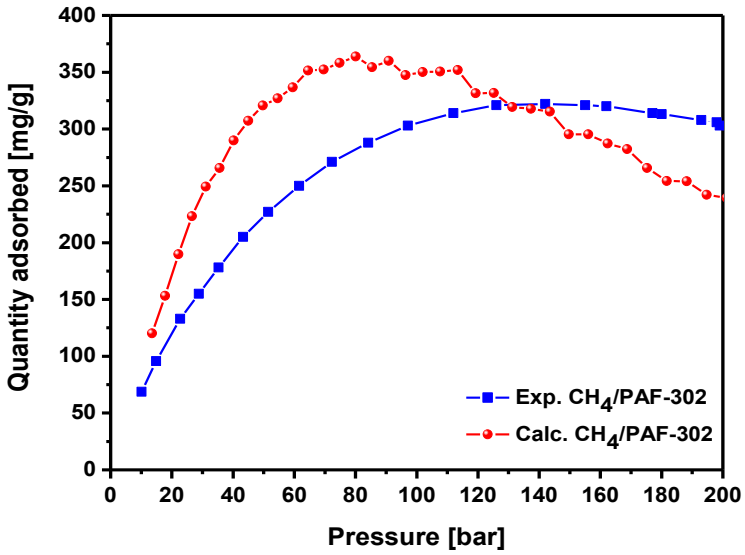

Figure 4.4. Experimental (blue squares) and theoretical (red spheres) excess storage capacity of CH_4 adsorbed on PAF-302 at 298 K and up to 200 bar.

The calculated results are referred to an ideal microporous crystalline material, while our PAF-302 synthesized material is defective (i.e. beside micropores, mesopores are also present). Then, lower adsorbed densities have to be expected in actual operative conditions. These idealized results show the upper limit that can be approached when improving the crystallinity of the samples, thanks to the combination of its high surface area and microporosity.

The presence of mesopores in the synthesized material causes the shift of the experimental adsorption maximum at high pressures (140 bar) in contrast to the calculated curve (80 bar), representative of an "ideal" material that contains only micropores.

For the hydrogen adsorption, the comparison of the experimental and theoretical curves, is shown in figure 4.5.

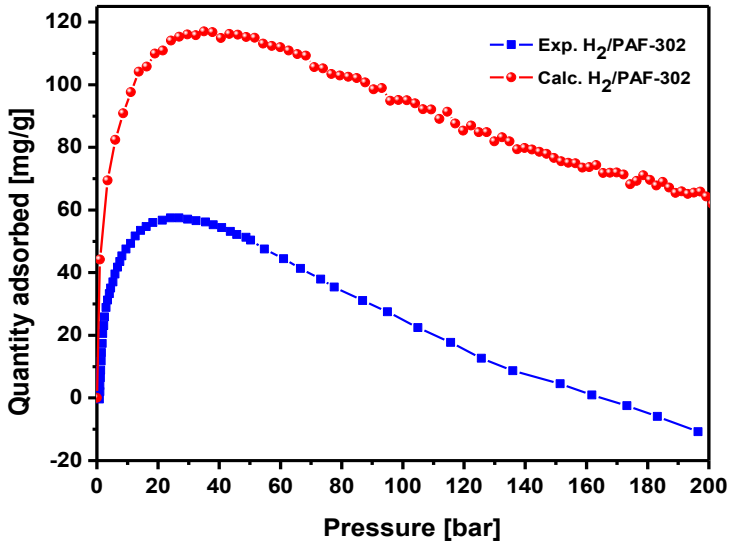

Figure 4.5. Experimental (blue squares) and theoretical (red spheres) excess storage capacity of H_2 adsorbed on PAF-302 at 77 K and up to 200 bar.

The experimental and calculated curves show the same trend but with different storage capacity: the synthesized material shows a maximum value of 57 mg/g at 25 bar, while the calculated curve reaches the maximum at 35 bar and 115 mg/g, a value double of the experimental one.

The behavior of the material in the experimental and theoretical hydrogen and methane storage is very different and mainly depends on the pore distribution.

Despite the difference in the total pore volume, the experimental and theoretical methane uptake lead to very similar storage capacity. This confirms the role of mesoporosity, which can contribute to improve the methane uptake, especially at high pressure. Regarding hydrogen, the capacity storage is strongly correlated to the amount of very small pores. The synthesized material stores half of the amount predicted, as the microporous total volume is half of the theoretical value as shown in the table 4.1.

An important consideration about the experimental and theoretical comparison is the poor crystallinity of the synthesized material which has a twofold negative effect: the smaller area reduces the interactions with gas, and the less porous structure increases the material bulk density, making the comparison with theoretical results even less favorable.

The comparison between the storage capacity of PAF-302 synthesized in our lab and those of selected materials reported in literature is now discussed. A large number of results can be found for methane and hydrogen adsorption in porous materials belonging to the class of activated carbons, metal organic

frameworks (MOF), and covalent organic frameworks (COF), which have been proposed for this kind of application much earlier than PAFs materials. In table 4.2, porosity data, CH_4 and H_2 gravimetric uptake of different microporous materials, are reported.

Table 4.2. Textural properties and H_2 and CH_4 uptake of selected porous materials.

Material	SSA_{BET} (m^2g^{-1}) [a]	V_{TOTAL} ($cm^3\ g^{-1}$)	Excess CH_4 uptake (298 K)		Excess H_2 uptake (77 K)		Ref
			P/bar	mg/g	P/bar	mg/g	
PAF-302	4293	2,38 (1,26)[c]	35	178	30	58	This work
			140	322	--	--	
PAF-1	5600	3.05	35	185	50	75.3	21
MOF-210	6240	3.60	80	264	55	86	22
PCN-14	1753	0.87	35	181[b]	30	46.2	23, 24
PCN-68	5109	2.13	100	390	28	73.2	25
PPN-4	6461	3.04	55	269	55	91	26
COF-102	3620	1.55	35	188	35	72	27
COF-103	3530	1.54	35	175	35	70	27
Maxorb-A	3100	1.38	40	211	--	--	4
KUA6	3808	1.27	--	--	30	57	9

(a) BET surface area from N_2 physisorption at 77K; (b) 290 K, (c) total microporous volume.

Some of the materials reported in table 4.2 have been described in Chapter 1, here we would like to focus our attention on the comparison of PAF-302 with the best adsorbing materials, belonging to the classes of porous aromatic framework (PAF-1), porous polymer networks (PPN-4), metal organic frameworks (MOF-210, PCN-68, PCN-14), covalent organic frameworks (COF-102 and COF-103) and porous carbons (Maxsorb-A and KUA6).

Regarding the storage of methane on the material PAF-302, the maximum adsorption is reached only at very high pressure, 140 bar with an uptake of 322 mg/g. Table 4.2 clearly shows that the gas storage capacity of a material is strongly dependent by both SSA and pore volumes, notwithstanding the nature of the porosity. However, a more reliable comparison can only be made if the pore size distribution for all materials is known. The material PAF-302 synthesized in our lab and that reported in literature by Ben et al [28], for instance, show similar storage capacity of hydrogen and methane, which can be easily ascribed to their similar textural properties.

In the case of gas storage at high pressure, the specific surface area is important because it reveals how much porosity a material has. A higher surface area means that a larger volume of gas can be stored.

However, for high storage capacity other parameters such as the presence of pores comparable to the size of the adsorbed gas and the presence of heteroatoms and / or metals, which contributes to increase the interaction forces between gas and framework, are relevant. From the comparison between PAFs and other materials, it can be seen how the presence of metals (MOF, PCN, PPN) and hetero atoms (COF and carbon) combined with the presence of pores with suitable size greatly affects gas uptake.

4.3 Gas adsorption on mPAF-1/n polymers

In section 3.3.1 the series of mPAF-1/n polymers were characterized with a wealth of experimental and computational methods. Thermogravimetry, infrared spectroscopy and solid-state-NMR were used to study the materials structure; the pore distribution was measured by applying the NLDFT (non-local density functional theory) analysis to the adsorption isotherms of N_2 at 77 K. The suitable pore size, large surface area and stability against moisture make these porous materials good candidates for gas storage and separation. In the following section, Ar, CH_4 and CO_2 adsorption will be discussed.

The porosity was carefully investigated by Ar adsorption at 87 K since it describes with greater accuracy the ultramicropores (<7 Å). Carbon dioxide and methane were adsorbed at 273, 298 and 195 K to evaluate the performance of these systems in terms of gas capture, separation and storage. A theoretical model of the porous network was defined to describe the ordered fraction of the material, with particular attention to ultramicropores; Ar, CO_2 and CH_4 adsorption in this model material was simulated by Monte Carlo technique with a purposely optimized force field.

4.3.1 mPAF-1/16 polymer: Experimental and theoretical Argon physisorption

The pore size distribution of mPAF-1/16, the material with the largest surface area in the mPAF-1/n series as determined by N_2 adsorption, was carefully studied through Ar physisorption. In figure 4.6 the Ar and N_2 adsorption/desorption isotherms in mPAF-1/16 (panel a and c) are presented along with the results of NLDFT analysis (panel b and d): as expected, the isotherms for Ar and N_2 are qualitatively very similar whereas the pore distribution analysis mainly differs in the micropore region.

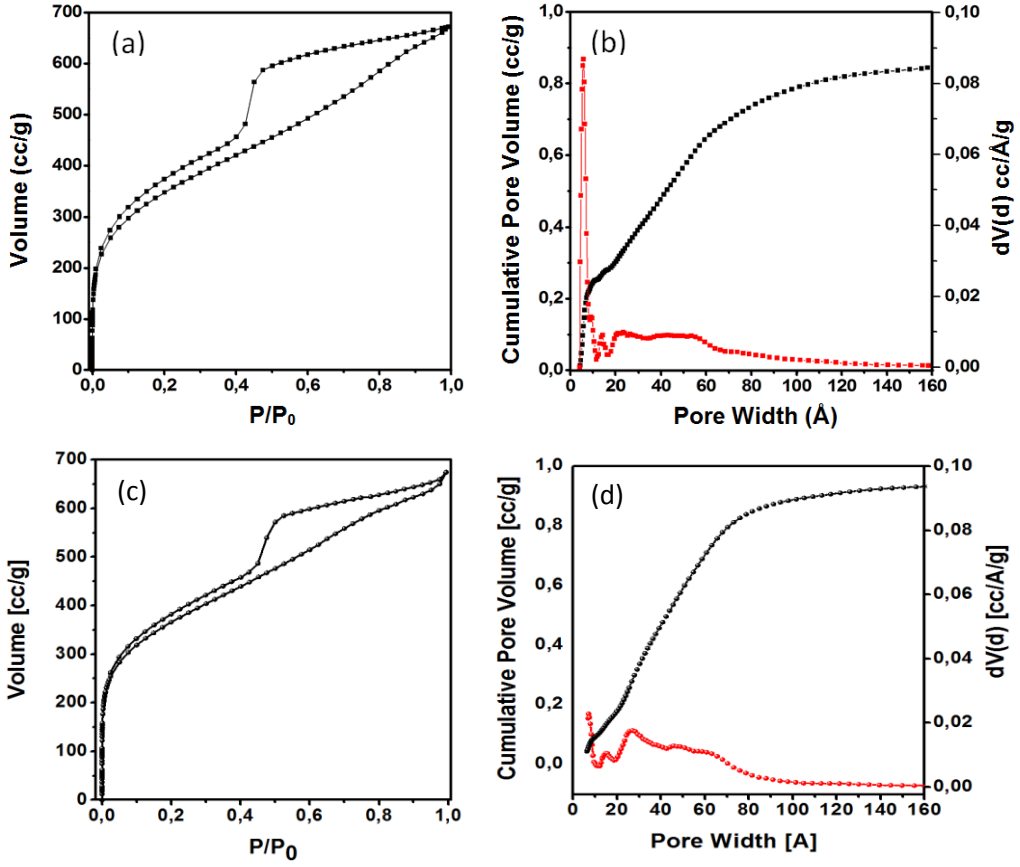

Figure 4.6. Ar physisorption isotherm at 87 K (a) and the pore size distribution with the cumulative pore (b); N_2 physisorption isotherm at 77 K (c) and the pore size distribution with the cumulative pore volume (d) of the sample mPAF-1/16. The pore size distributions are calculated using NLDFT method for silica cylindrical pores in the adsorption branch.

A narrow peak is observed in the pore distribution curve (Figure 4.6b), corresponding to ultramicropores of 5.82 Å wide, with a much smaller peak around 15 Å: the total microporous volume due to these pore families is 0.30 cm^3/g. A very broad signal is observed above 20 Å, attributed to several types of mesopores: the total pore volume results 0.89 cm^3/g. These findings compare well with NLDFT data on N_2 adsorption isotherms, except that the ultramicropores are found at a smaller width. As discussed above, the analysis of Ar isotherms provides more reliable results for such small pores. The narrow distribution of ultramicropores suggests that a part of the material is regularly polymerized, indicating the presence of ordered islands surrounded by less regular and amorphous regions. This picture is strongly supported by the comparison with the theoretical models presented below.

4.3.2 mPAF-1-/16 crystal structure from modeling

An ideal crystal structure for mPAF was optimized as described in detail in the ref. 13: the unit cell is reported in figure 4.7, along with a 2x2x1 supercell where van der Waals atomic spheres are used to sketch the porous

free volume. In this model the unit cell formula is $C_{108}H_{80}$ and the cell volume 3100 $Å^3$, with a resulting density of 0.738 g/cm^3.

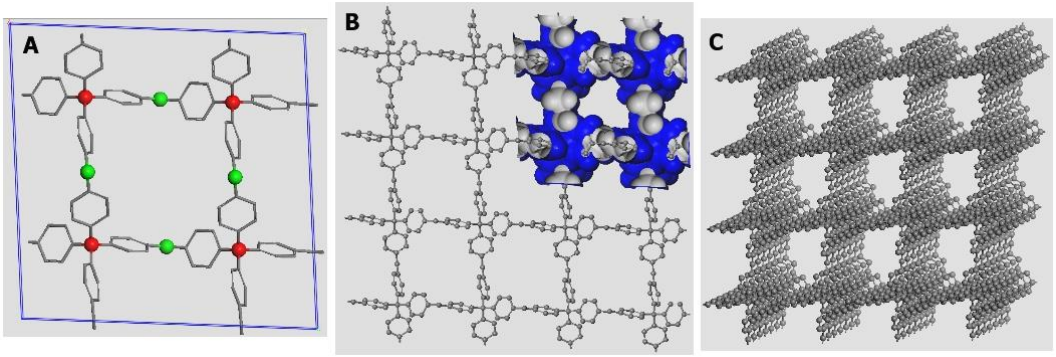

Figure 4.7. Optimized periodic structure of model mPAF-1/16; (a) unit cell, showing the sp3 carbon atoms belonging to TPM (red) and FDA (green); (b) 2x2x1 supercell, showing the van der Waals surface obtained with radii: 1.7 Å for C, 1.2 Å for H; (c) 2x2x6 supercell to highlight the 3D channel structure. Hydrogen atoms are not represented in the structures.

In figure 4.8a the Ar adsorption isotherm at 87 K, simulated with Monte Carlo technique, is compared to the adsorption isotherm of mPAF-1/16. The two curves are in reasonable agreement, considering that the model is an idealized picture of the mPAF crystal, with no defects and perfectly regular crosslinking in para position: as a result, only one family of micropores is expected in the model.

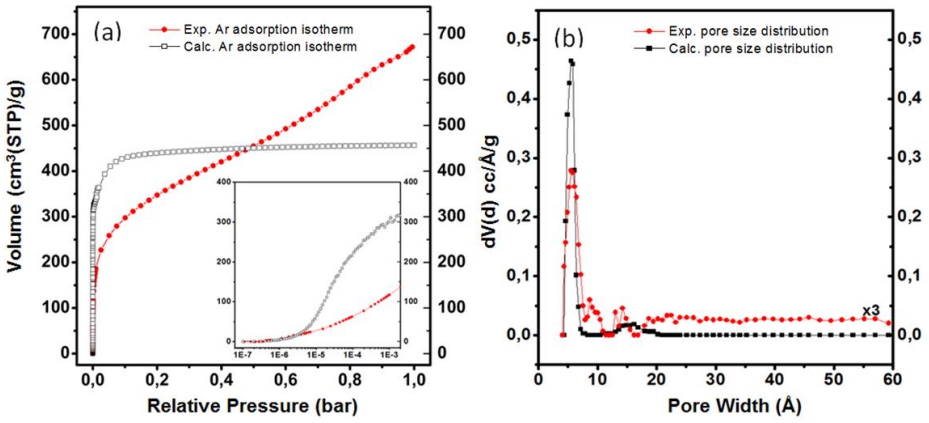

Figure 4.8. (a) Simulated and experimental Ar adsorption isotherms at 87 K. Inset: logarithmic plot of the low pressure region. (b) Pore size distribution calculated with NLDFT method for silica cylindrical pores on simulated and experimental (magnified x3) adsorption isotherms. Black squares: theoretical model; red circles: mPAF-1/16 sample.

Noteworthy, at very low pressure the two curves are in very good agreement (Figure 8a, inset), indicating a similar intensity of the host-guest interactions when the gas is preferentially adsorbed in the smallest micropores. At slightly higher pressures (10^{-5} to 10^{-3} bar), the simulated adsorption is larger than in the experiment, since all the specific volume in the model material is microporous (unlike in the experimental samples). On the other hand, at pressures around 1 mbar the model pores are saturated, while the experimental isotherm keeps growing as the gas fills larger and larger pores. We recall that the model is an idealized picture of the mPAF crystal, with no defects and perfectly regular crosslinking in para position: as a result, only one family of micropores is expected.

The NLDFT procedure was applied to the simulated isotherm, in the same conditions as for the experimental curve: the results are reported in figure 4.8b. The agreement between the simulated and experimental pore distributions is very good in the ultramicropores region: in fact, a narrow micropore distribution around 5.52 Å width is found, in very good agreement with the smallest pores found for the experimental sample (that is 5.82 Å). The second, much lower peak at 15 Å, visible for the simulated distribution in figure 4.8b, is likely due to an artifact of NLDFT, related to the noisy trend of Monte Carlo simulations around 0.1 bar (figure 4.8a). In the mesoporous region, between 20 and 60 Å, the experimental pore distribution lies above the simulated curve, as expected.

Note that the total pore volume in the model is 0.80 cm^3/g (entirely microporous, as remarked above), while for mPAF-1/16 the NLDFT analysis indicated 0.89 and 0.30 cm^3/g for total and microporous volume, respectively.

The plausibility of this pore size estimate can be qualitatively appreciated by considering a sphere embedded in the van der Waals surface reported in figure 4.7b: as shown in figure 4.9 a sphere with 5.8 Å diameter fits in the model pore quite well, whereas a 8 Å sphere, as indicated by the less reliable N_2 isotherm, would clearly be too wide for this model.

In conclusion, on the basis of the above discussion, we believe that the most regular and ordered fraction of mPAF materials is well described by this model structure, which can be used to predict the gas uptake in the ultramicroporous volume.

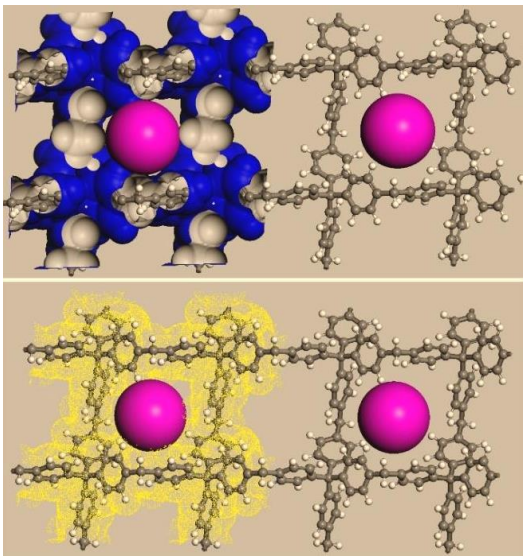

Figure 4.9. Spheres of 5.8 Å diameter embedded in the mPAF model structure, with and without van der Waals surface. VdW radii: C 1.7 Å, H 1.2 Å.

4.3.3 mPAF-1/n polymers: Experimental N_2, CO_2 and CH_4 adsorption

The suitable pore size, large surface area and stability against moisture make these porous materials good candidates for gas storage and separation. CH_4 and CO_2 sorption isotherms were measured volumetrically up to 10 bar at 273 K (Figure 4.10a) and 298 K (Figure 4.10b) for all samples.

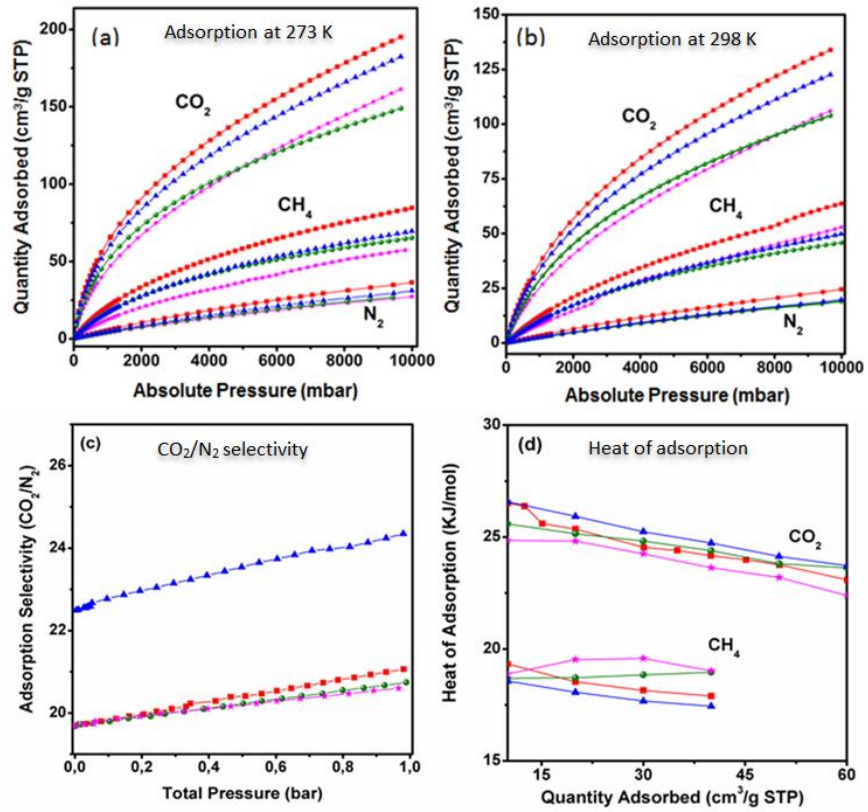

Figure 4.10. CH_4 adsorption isotherms up to 10 bar at 273K (a) and 298K (b), CO_2/N_2 selectivity (c) and heat of adsorption of CO_2 and CH_4 (d) of the mPAF polymers: mPAF-1/3 (green spheres), mPAF-1/9 (magenta stars), mPAF-1/16 (red squares) and mPAF-1/30 (blue triangles**).**

The CH_4 and CO_2 isotherms show a Langmuir profile, although at both temperatures and at 10 bar the saturation values have not yet been reached. The adsorption isotherms at 195 K and 1 bar were also collected (figures 4.11), to evaluate the maximum uptake for CO_2 and to calculate the isosteric heat of adsorption for methane.

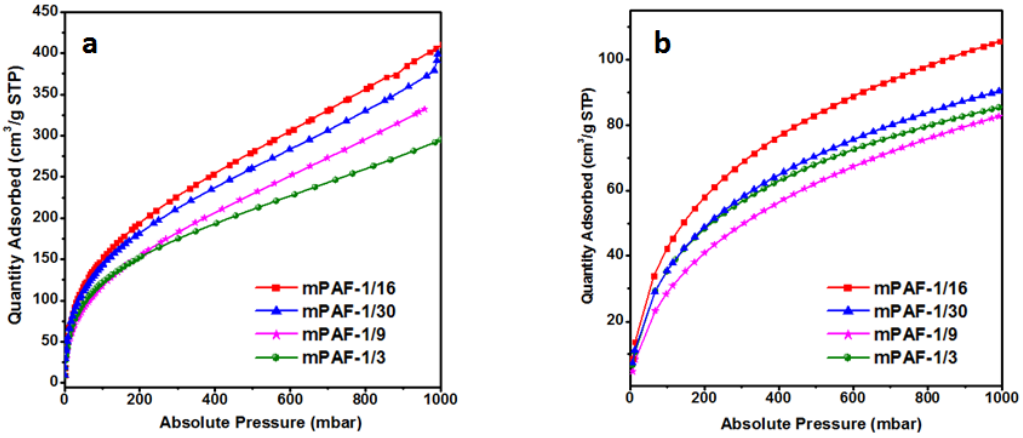

Figure 4.11. Experimental CO_2 (a) and CH_4 (b) adsorption isotherms at 195K and up to 1 bar of the polymers: mPAF-1/3 (green spheres), mPAF-1/9 (magenta stars), mPAF-1/16 (red squares) and mPAF-1/30 (blue triangles).

In table 4.3 the excess gas uptake capacity of the four materials at different temperatures and pressures are reported: mPAF-1/16 shows the highest adsorption for both CH_4 and CO_2 gas, in good agreement with the highest apparent BET surface and microporous volume with respect to the other mPAF samples.

Table 4.3. Experimental excess uptake of methane and carbon dioxide and nitrogen at 298, 273 K up to 10 bar and methane and carbon dioxide at 195 K up to 1 bar into mPAF networks.

Sample	CH_4 (cm^3/g)			CO_2 (cm^3/g)			N_2 (cm^3/g)	
	195 K 1 bar	273 K 10 bar	298 K 10 bar	195 K 1 bar	273 K 10 bar	298 K 10 bar	273 K 10 bar	298 K 10 bar
mPAF-1/3	86	65	46	298	149	104	28,3	19,0
mPAF-1/9	84	57	52	332	161	106	27,3	18,9
mPAF-1/16	106	84	64	410	195	134	36,4	24,5
mPAF-1/30	91	70	50	387	182	123	31.0	19.8

The series of mPAF materials is particularly efficient under mild conditions (1 bar), where mPAF-1/16 adsorbs 64 cm^3(STP)/g (2.82 mmol/g) of CO_2 at 273 K (figure 4.10a). In the same conditions, mPAF-1/3, mPAF-1/9 and mPAF-1/30 CO_2 uptakes are about 46, 51 and 60 cm^3(STP)/g (2.03, 2.25 and 2.64 mmol/g), respectively. These uptake values are comparable to PAFs (2.05 – 3.48 mmol/g) [29], COFs (1.21 – 3.84 mmol/g) [27], and other HCPs polymers (1.11 – 3.96 mmol/g) [30-32]. In particular the CO_2 uptake is very close to the value (2.95 mmol/g) reported in ref. 31 for an analogous material with a slightly higher BET surface area. High CO_2

uptakes have also been measured in activated porous carbons, ranging from 2 to 7.4 mmol/g for materials with BET SSA up to 3400 m^2/g [33, 34].

The good performance of mPAF materials can be attributed to the abundance of ultramicropores (centered around 0.58 nm): in fact, very high CO_2 uptakes at low pressure are expected in porous materials with a high fraction of pores below 1 nm, as observed for instance in the case of KOH carbonization of PAF [21]. This behaviour has also been related to the presence of pores commensurate with the kinetic diameter of carbon dioxide [35].

The isosteric heat of adsorption (Q_{st}) computed from the excess isotherms at 273 and 298 K is reported in Figure 4.10d for all samples: at low coverage (< 10 cm^3/g) Q_{st} varies between 24.5 and 26 kJ/mol, demonstrating the occurrence of favorable interactions of CO_2 with the aromatic network; these values agree with the isosteric heats measured in refs. 31 and 36, tending to 26 kJ/mol at very low CO_2 uptakes. Remarkably, Q_{st} for CO_2 in mPAF materials exceeds that measured in PAF-302 (15 kJ/mol, ref. 28, where it is referred to as PAF-1), which contains the same chemical moieties but has markedly wider pores, confirming the role of ultramicroporosity in the adsorption process.

Nitrogen uptake (figure 4.10a,b) is quite low even at pressures as high as 10 bar, indicating a low affinity for the absorbent. This result can be exploited favorably for selective adsorption of CO_2/N_2 mixtures in actual industrial applications. At low pressure and 273 K, the mPAF hyper-crosslinked networks show high CO_2/N_2 selectivity between 20 and 23 (figure 4.10c), which is comparable to most microporous organic polymers [31].

The uptake capacities of all samples for methane were also studied; mPAF-1/16 showed a CH_4 uptake of 84 and 64 cm^3(STP)/g at 10 bar and 273 and 298 K, respectively (figure 4.10a,b), while the maximum uptake measured at 195 K, amounts to 106 cm^3(STP)/g (figure 4.11b). On the other hand, mPAF-1/3, mPAF-1/9 and mPAF-1/30 samples exhibited lower CH_4 uptakes, according to their lower surface areas. Isosteric heats of adsorption were measured from the excess isotherms at 195, 273 and 298 K, with the results shown in figure 4.10d at low coverage methane Q_{st} is in the range 17.5-19.5 kJ/mol. As already observed for CO_2, methane isosteric heats in mPAF are significantly higher than that measured for PAF-302 (slightly below 15 kJ/mol in ref. 28); a similar value of 15 kJ/mol was estimated theoretically for a methane molecule interacting with a single ditolyl-methane molecule, resembling the local environment in porous aromatic frameworks [37]. Also in this case, the higher interactions experienced in mPAF can be attributed to the ultramicroporosity, which enhances the adsorption capacity at low pressures.

4.3.4 mPAF-1/16 polymer : simulated uptake of CH_4 and CO_2

Monte Carlo simulations were performed to study methane and carbon dioxide adsorption in the mPAF model structure described above: in figure 4.12 the theoretical excess isotherms at 298 K are compared to the corresponding experimental curves (referred to the mPAF-1/16 sample). As expected, the simulated excess adsorptions are systematically larger than the measured ones: at 1 bar the CH_4 adsorptions in the model and in mPAF-1/16 are 27 and 8 cm^3(STP)/g, respectively, while at 10 bar the two values are 98 and 64 cm^3(STP)/g. The CO_2 adsorptions in the model and in the real sample are 125 and 38 cm^3(STP)/g at 1 bar, and 210 and 136 cm^3(STP)/g at 10 bar.

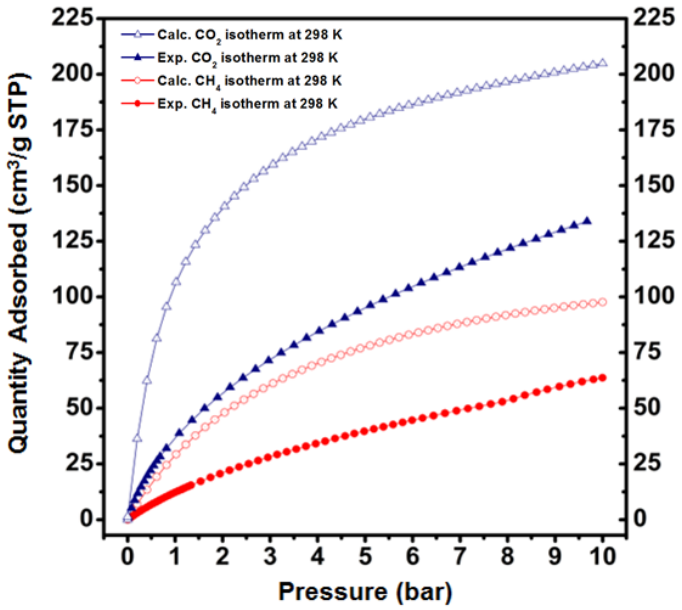

Figure 4.12. Simulated (empty symbols) and experimental (filled symbols, mPAF-1/16 sample) excess adsorption isotherms at 298 K. Blue triangles: carbon dioxide adsorption; red circles: methane adsorption.

At the pressure of 1 bar the ratio of the adsorbed amounts is quite close to the ratio of microporous volume in the model and in mPAF-1/16 (0.83 and 0.21 cm^3/g, respectively, as seen above). This indicates that, in these conditions, the adsorption occurs mainly in the microporous fraction of the material. At higher pressure, however, also the mesoporous volume of the real sample makes an important contribution to the total adsorption, and the simulated and experimental curves get closer, also because the model isotherms are approaching the saturation plateau. The isosteric heats of adsorption were computed from the simulated excess isotherms as well, and the results at low coverage are in very good agreement with the measured values: 24 kJ/mol for CO_2 and 18 kJ/mol for CH_4.

The simulations confirm the very good performance of this material in gas uptake, especially at low pressures. In particular, the model highlights the central role of microporous and ultramicroporous volume to achieve such results, thus indicating the way to improve the uptake even further.

4.3.5 PAF-302 Vs. mPAF-1/16: CH_4 volumetric adsorption

Independently on the gas used (H_2, CH_4 or CO_2), the gas storage performances, when expressed on a gravimetric basis, are completely different from those expressed on a volumetric basis.

It is interesting to observe that at 10 bar and 298K the volumetric CH_4 uptake in mPAF-1/16 exceeds that of PAF-302: as shown in table 4.4, despite the lower specific surface area, the volumetric adsorption in mPAF-1/16 is higher than in PAF-302, due to mPAF higher density. In general, these results demonstrate that for adsorption on a gravimetric basis, the textural properties are very important, since the adsorbents with increased porosity reach higher values. However, on a volumetric basis, the density of the adsorbent material plays a key role, and the volumetric capacity is more relevant from the application point of view.

Table 4.4. Comparison of gravimetric and volumetric CH_4 uptake in mPAF-1/16 and PAF-302 at 10 bar and 298K.

Polymer	SSA (m^2/g)	PV[(a)] (cc/g)	MPV[(b)] (cc/g)	Density[(c)] (g/cc)	T (K)	P (bar)	Gravimetric uptake	Volumetric uptake
mPAF-1/16	1321	0,83	0,21	**0.6**	298	10	64 cc/g	27,13 g/L
PAF-302	4563	2,89	1,26	**0.29**	298	10	89 cc/g	18,44 g/L

(a) Total pore volume calculated at $P/P_0 = 0.99$, (b) Total micropore volume up to 20 A, (c) The density values are obtained from helium pycnometry measurements at room temperature.

The high density of the material however implies even increased amount of sample to be put in the cylinders, for on-board storage application. This leads to increase the costs required. In our case, also from the point of view of costs the material mPAF-/16, is more advantageous than PAF-302: just to give an idea, on a laboratory scale mPAF-1/16 costs 5 €/g while PAF-302 costs 340 €/g. Therefore, from an industrial application, materials obtained with Friedel-crafts synthesis are cheaper and more efficient. In fact, this method has led to the deposition of a European patent [38] and the material was called UPO-1 (UPO stands for Università Piemonte Orientale).

4.4 Zero Length Column method (ZLC) for CO_2 uptake measurements

The CO_2 uptake measurements were performed at the University of Edinburgh by Dr. Giorgio Gatti. All the samples were tested using the Zero Length Column (ZLC) method, at 0.1 bar and 35 ºC which are the real conditions of a typical flue gas stream from post-combustion applications.

The technique was first introduced by Eic and Ruthven for the measurements of intra-crystalline diffusion in zeolites [39] and was then extended to measurements under equilibrium conditions [40, 41]. The ZLC consists of a thin layer of adsorbent material placed between two porous sinter discs. Because of the small size of the adsorption column, which consists in a 1/8" Swagelok union (the sample is housed in monolayers between two sinter discs) as shown in figure 4.13, the heat and mass transfer resistances and also the axial dispersion can be neglected. If compared to other techniques, ZLC presents the advantage of requiring a very small amount of sample (<15 mg) allowing to rapidly obtain kinetic and equilibrium properties of the analyzed materials. Furthermore, it allows for the rapid screening of materials since the analysis time of each sample is short.

Figure 4.13. Adsorption column of ZLC instrument

To make sure that the sample's adsorption sites are free of any solvent, the column temperature was gradually increased from room temperature to its own regeneration temperature for 8-12 hour under He atmosphere. The experiment consists in: i) equilibration of the sample with a mixture of 10% of CO_2 (adsorbate) in He (carrier) at a constant flow rate; ii) when equilibrium between the gas phase and the adsorbed phase is reached, the desorption starts by switching the inlet flow to pure He (purge) and the outlet gas phase concentration from the column is monitored. An on-line quadrupole mass spectrometer (Ametek Benchtop) is connected to the ZLC to monitor the outlet gas concentration. The CO_2 capacities is evaluated from the integration of the desorption curves [41, 42].

The results of the most promising PAF and HCP materials for carbon capture synthesized in this thesis work are presented in figure 4.14. They were tested and compared using the same experimental conditions. This allows for a direct comparison between the samples. Table 4.5 show the comparison of the CO_2 capacity measured using ZLC method and the total micropore volume (pores smaller than or equal to 10 Å) determined by NLDFT method.

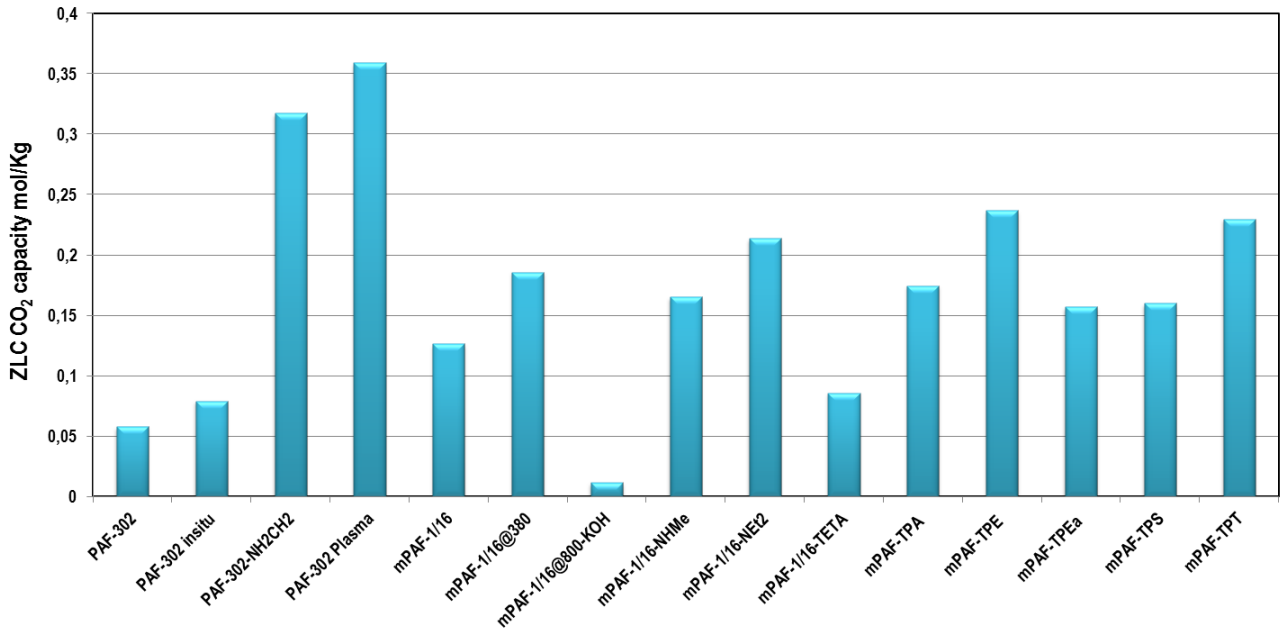

Figure 4.14. CO_2 capacity measurements for PAF polymers, found by zero length column (ZLC) procedure

PAF-302 in situ polymer performed well if compared to parent PAF-302. The larger micropore volume in the case of PAF-302 in situ explains well this result , since micropores are more suitable for CO_2 adsorption.

It is clear from the above results that PAF-302 functionalized with amino groups (PAF-302- NH_2CH_2 and PAF-302-plasma) have the highest adsorption capacity for CO_2 out of those tested: the main explanation is that the presence of amino groups in the structure of the polymer enhances affinity towards carbon dioxide. Obviously also the presence of very small micropores contributes to this increase.

mPAF-1/16 polymer belongs to the class of HCPs, characterized by lower surface areas and pore volume compared with PAF materials. However, this polymer is characterized by a heterogeneous pore distribution of small and large micropores (8 and 14 Å), and a small quantity of mesopores. mPAF-1/16 has a good storage capacity, twice that of PAF-302, possibly explained by its larger micropore volume.

The thermally treated mPAF-1/16 polymers lead to different results: the heating at 380 °C, leads to a material with better CO_2 uptake capacity, while the carbonization (m-PAF-1/16@800-KOH) leads to the worst uptake capacity in the series. These results are in perfect agreement with the extension of the micropore volume, which affects the CO_2 adsorption: in the first case, the treatment leads to an increase of the microporosity, while the second case leads to a larger surface area but disappearance of pores lower than 10 Å.

The CO_2 adsorption capacity of the amino functionalized mPAF-1/16 polymers was also studied using the ZLC method. An increase in the CO_2 uptake of the polymers was observed after functionalization, especially for the

mPAF-1/16-NHMe and mPAF-1/16-NEt_2 samples, because the presence of amino groups in the polymer enhances the interaction between CO_2 molecules and the polymer. The behavior of the mPAF-1/16-TETA sample, which contains a higher nitrogen content and substantially similar microporosity as the parent mPAF-1/16, is different: it exhibits smaller CO_2 gas adsorption. One possible explanation is that the mPAF-1/16-TETA polymer has a slower adsorption kinetics and the maximum uptake cannot be reached during the rapid ZLC analysis.

ZLC CO_2 uptakes for mPAF materials with different tetrahedral precursors were also measured: these samples are characterized by high CO_2 adsorption capacity with respect to mPAF-1/16, although it is difficult to correlate these data with the microporous volume. mPAF-TPA, mPAF-TPEa and mPAF-TPS show a CO_2 capacity of ca. 0.16 mol/Kg, while the samples mPAF-TPE and mPAF-TPT show a higher capacity of 0.23 mol/Kg.

From table 4.5 it is very clear that the pore size greatly affects the CO_2 storage capacity: small pores give higher CO_2 uptake due to stronger interactions between molecules and framework. Also the presence of nitrogen atoms and metals may affect CO_2 uptake; however, the polymers do not seem to show their real CO_2 capacity (excess adsorption) because of the ZLC experiment conditions.

Table 4.5. The comparison of the CO_2 capacity measured using ZLC method and the total micropore volume (pores < 10 Å) determined by NLDFT method.

Polymer	CO_2 capacity [mol/Kg]	Micropore volume <10Å [cc/g]
PAF-302	0,058	0,029
PAF-302 in situ	0,079	0,36
PAF-302-NH_2CH_2	0,317	0,22
PAF-302 Plasma	0,359	0,022
mPAF-1/16	0,127	0,069
mPAF-1/16@380	0,186	0,12
mPAF-1/16@800-KOH	0,012	--
mPAF-1/16-NHMe	0,165	0,073
mPAF-1/16-NEt_2	0,214	--
mPAF-1/16-TETA	0,086	0,047

mPAF-TPA	0,175	0,14
mPAF-TPE	0,237	0,054
mPAF-TPEa	0,157	0,14
mPAF-TPS	0,16	0,11
mPAF-TPT	0,23	0,13

In the literature there are few measurements for porous materials in these conditions. However, E. Mangano et al. [43] have published a work where they used TLC method with the same experimental conditions used in our measurements to evaluate the CO_2 uptake capacity for various materials including MOFs, Zeolites, Activated Carbon and PIMs. Here we will consider for comparison only the last two classes, for their surface chemistry similar to PAFs and HCPs. Table 4.6 shows some CO_2 uptake from ZLC method reported in the literature for carbons and PIMs.

Table 4.6. CO_2 uptake measured by ZLC method for activated carbons and PIM polymers from ref .43.

Polymer	**CO_2 uptake [mol/Kg]**
PIM 1 unmodified	0,14
PIM 1 sample3	0,306
PIM 1 sample2	0,275
PIM1 sample 1	0,34
BPL Carbon	0,35

E. Mangano et al. report the CO_2 uptake of several types of PIMs synthesized with different methods and modified in order to increase porosity and affinity to CO_2. Unmodified PIM-1 showed a very low uptake (0.14 mol/kg), while modified PIMs (PIM 1 samples 1-3) gives high capacity values, similar to those of BPL carbon, which gives a CO_2 capacity of 0.35 mol/kg. These data show that the our results are very similar to those reported in the literature.

4.5 Conclusions

The CH_4, H_2 and CO_2 adsorption capacities of PAF and HCP materials synthesized in this PhD work have been measured to evaluate their performance in gas capture and storage, at different temperatures and pressures. Some results were also compared with GCMC simulations made within our research group.

Initially, physisorption measurements of Ar were made on representative materials of the two classes to have more information on the families of small micropores. The results were also confirmed by the simulated data.

For the PAF-302 sample, being characterized by a very high surface area, methane and hydrogen measurements at pressures up to 200 bar were made: for CH_4 adsorption, the importance of a high total micropore volume (PAF-302 shows pores of about 12 Å) and the presence of small mesopores was confirmed. All these factors have contributed to get a material with high methane uptakes. With regard to the hydrogen uptake, the experimental and computational measurements have confirmed the importance of microporosity: being the volume of the synthesized material half of that calculated, also the experimental hydrogen storage is about half of the predicted value.

The series of mPAF-1/n materials have been extensively characterized, and the capacity of CH_4 and CO_2 were measured in different conditions of temperature and pressure. The sample with larger surface area, mPAF-1/16, was also studied by Ar physisorption at 87K, which shows that these materials have ultramicropores of 5.8 Å particularly suitable for gas storage at low pressures. The gas storage capacity, the heat of adsorption, and the selectivity have been widely studied and the results are comparable with similar materials reported in the literature.

The comparison of the volumetric and gravimetric measurements of CH_4 at 298 K and 10 bar for mPAF-1/16 and PAF-302 confirms the importance of the density of porous materials: PAF-302, despite its high surface area and high pore volume shows a volumetric storage capacity smaller than mPAF-16. Indeed, the measured density of mPAF-1/16 is about twice that measured for PAF-302.

Finally, the CO_2 storage capacity for almost all materials synthesized in this thesis was evaluated using the ZLC method. This is a fast technique that requires little amount of sample and allowed a rapid screening and a direct comparison of the synthesized materials. As a main result, the measurements have confirmed the importance of the pores smaller than 7Å and the need to functionalize the materials with heteroatoms to increase the CO_2 capacity. The comparison with similar data reported in the literature for carbons and PIMs has confirmed the potential of our materials in gas storage applications.

References:

[1] Lennard-Jones, J. E. *Trans. Faraday Soc*. **1932**, 28, 333.

[2] Düren, T.; Bae, Y.-S.; Snurr, R. *Q.* Using molecular simulation to characterise metal-organic frameworks for adsorption applications. *Chem. Soc. Rev* **2009**, 38, 1237-47.

[3] Yeon, S.H.; Knoke, I.; Gogotsi, Y.; Fischer, J. E. Enhanced volumetric hydrogen and methane storage capacity of monolithic carbide-derived carbon. *Microporous Mesoporous Mater* **2010,**131, 423-428.

[4] Lozano-Castelló, D.; Alcañiz-Monge, J.; de La Casa-Lillo, M. A.; Cazorla-Amorós, D.; Linares-Solano, A. Advances in the study of methane storage in porous carbonaceous materials. *Fuel* **2002**, 81, 1777-1803.

[5] Alcañiz-Monge, J.; De la Casa-Lillo, M.A.; Cazorla-Amorós, D.; Linares-Solano, A. Methane storage in activated carbon fibres. *Carbon* **1997**, 35, 91.

[6] Menon, V. C.; Komarneni, S. Porous Adsorbents for Vehicular Natural Gas Storage: A Review

J. Porous Mater. **1998**, 5, 43-58.

[7] Yang, S. J.; Im, J. H.; Nishihara, H.; Jung, H.; Lee, K.; Kyotani, T.; Park, C. R. General Relationship between Hydrogen Adsorption Capacities at 77 and 298 K and Pore Characteristics of the Porous Adsorbents *J. Phys. Chem. C* **2012**, 116, 10529–10540.

[8] Presser, V.; McDonough, J.; Yeon, S.-H.; Gogotsi, Y. Effect of pore size on carbon dioxide sorption by carbide derived carbon. *Energy Environ. Sci.* **2011**, 4, 3059–3066.

[9] Jorda-Beneyto, M.; Suarez-Garcia, F.; Lozano-Castello, D.; Cazorla- Amoros, D.; Linares-Solano, A. Hydrogen storage on chemically activated carbons and carbon nanomaterial s at high pressures. *Carbon* **2007**, 45, 293–303.

[10] M. Jorda-Beneyto, D. Lozano-Castello, F. Suarez-Garcia, D. Cazorla-Amoros and A. Linares-Solano, *Microporous Mesoporous Mater.* **2008**, 112, 235–242.

[11] Zacharia, R.; Cossement, D.; Lafi, L.; Chahine, R. Volumetric hydrogen sorption capacity of monoliths prepared by mechanical densification of MOF-177. *J. Mater. Chem.* **2010**, 20, 2145–2151.

[12] Errahali, M.; Gatti, G.; Tei, L.; Paul, G.; Rolla, G. A.; Canti, L.; Fraccarollo, A.; Cossi, M.; Comotti, A.; Sozzani, P.; Marchese, L. Microporous Hyper-Cross-Linked Aromatic Polymers Designed for Methane and Carbon Dioxide Adsorption. *J. Phys. Chem. C* **2014**, 118, 28699–28710.

[13] Lan, J.; Cao, D.; Wang, W.; Ben, T.; Zhu, G. High-Capacity Hydrogen Storage in Porous Aromatic Frameworks with Diamon d-like Structure. *J. Phys. Chem. Lett.* **2010**, 1, 978–981.

[14] Cossi, M.; Gatti, G.; Canti, L.; Tei, L.; Errahali, M.; Marchese, L. Theoretical Prediction of High Pressure Methane Adsorption in Porous Aromatic Frameworks (PAFs). *Langmuir* **2012**, 28, 14405-14414.

[15] Sun, H.; Mumby, S. J.; Maple, J. R.; Hagler, A. T. An Ab Initio CFF93 All-Atom Force Field for Polycarbonates. *J. Am. Chem. Soc.* **1994**, 116, 2978-2987.

[16] Lemmon, E. W.; McLinden, M. O.; Friend, D. G. NIST Chemistry WebBook: Nist Standard Reference Database Number 69; National Institute of Standards and Technology: Washington DC, US, 2011.

[17] Lowell, S.; Shields, J.; Thomas, M.A.; Thommes, M. *Characterization of porous solids and powders: surface area, pore size and density.* 2004,The Netherlands: Springer.

[18] Züttel, A. B. A.; Schlapbach, L. Hydrogen as a future energy carrier. *Wiley-VCH*: Weinheim, **2008**.
[19] Tedds, S.; Walton, A.; Broom, D. P.; Book, D. Characterisation of porous hydrogen storage materials: carbons, zeolites, MOFs and PIMs. *Faraday Discuss.* **2011**, 151, 75–94.

[20] Sircar, S. Gibbsian surface excess for gas adsorption - Revisited. *Industrial & Engineering Chemistry Research* **1999**, 38, 3670-3682.

[21] Li, Y.; Ben, T.; Zhang, B.; Fu, Y.; Qiu, S. Ultrahigh Gas Storage both at Low and High Pressures in KOH-Activated Carbonized Porous Aromatic Frameworks. *Scientific Reports*, **2013**, *3*, 2420.

[22] Furukawa, H.; Ko, N.; Go, Y. B.; Aratani, N.; Choi, S. B.; Choi, E.; Yazaydin, A. O.; Snurr, R. Q.; O'Keeffe, M.; Kim, J.; Yaghi, O. M. Ultrahigh porosity in metal-organic frameworks. *Science* **2010**, 329, 424–428.

[23] Ma, S. Q.; Sun, D. F.; Simmons, J. M.; Collier, C. D.; Yuan, D. Q.; Zhou, H. C. Metal-organic framework from an anthracene derivative containing nanoscopic cages exhibiting high methane uptake. *J. Am. Chem. Soc.* **2008**, 130, 1012−1016.

[24] Ma, S.; Simmons, J. M.; Sun, D.; Yuan, D.; Zhou, H.-.C. Porous Metal-Organic Frameworks Based on an Anthracene Derivative: Syntheses, Structure Analysis, and Hydrogen Sorption Studies. *Inorg. Chem.* **2009**, 48, 5263–5268.

[25] Yuan, D.; Zhao, D.; Sun, D. F.; Zhou, H.-C. An Isoreticular Series of Metal–Organic Frameworks with Dendritic Hexacarboxylate Ligands and Exceptionally High Gas-Uptake Capacity. *Angew. Chem.* **2010**, 49, 5357-61.

[26] Yuan, D.; Lu, W.; Zhao, D.; Zhou, H. C. Highly Stable Porous Polymer Networks With Exceptionally High Gas-Uptake Capacities. *Adv. Mater*. **2011**, *23*, 3723-3725.

[27] Furukawa H.; Yaghi, O. M. Storage of Hydrogen, Methane and Carbon Dioxide in Highly Porous Covalent Organic Frameworks for Clean Energy Applications. *J. Am. Chem. Soc.* **2009**, *131*, 8875–8883.

[28] Ben, T.; Ren, H.; Ma, S.; Cao, D.; Lan, J.; Jing, X.; Wang, W.; Xu, J.; Deng, F.; Simmons, J. M.; et al. Targeted Synthesis of a Porous Aromatic Framework With High Stability and Exceptionally High Surface Area. *Angew. Chem., Int. Ed.* **2009**, *48*, 9457-9460.

[29] Ben, T.; Pei, C.; Zhang, D.; Xu, J.; Deng, F.; Jing, X.; Qiu, S. Gas Storage in Porous Aromatic frameworks (PAFs). *Energy Environ. Sci.* **2011**, *4*, 3991-3999.

[30] Luo, Y.; Li, B.; Wang, W.; Wu, K.; Tan, B. Hypercrosslinked Aromatic Heterocyclic Microporous Polymers: A New Class of Highly Selective CO_2 Capturing Materials. *Adv. Mater*. **2012**, *24*, 5703–5707.

[31] Dawson, R.; Stöckel, E.; Holst, J.R.; Adams, D. J.; Cooper, A. I. Microporous Organic Polymers for Carbon Dioxide Capture. *Energy Environ. Sci.* **2011**, *4*, 4239-4245.

[32] Martìn, C. F.; Stöckel, E.; Clowes, R.; Adams, D. J.; Cooper, A. I.; Pis, J. J.; Rubiera, F.; Pevida, C. Hypercrosslinked Organic Polymer Networks as Potential Adsorbents for Pre-Combustion CO_2 Capture. *J. Mater. Chem*. **2011**, *21*, 5475–5483.

[33] Lozano-Castellò, D.; Cazorla-Amorò, D.; Linares-Solano; A. Quinn, D. F. Micropore Size Distributions of Activated Carbons and Carbon Molecular Sieves Assessed By High-Pressure Methane and Carbon Dioxide Adsorption Isotherms. *J. Phys. Chem. B* **2002**, *106*, 9372-9379

[34] Lu, A-H.; Dai, S. *Porous Materials for Carbon Dioxide Capture*; Springer: Heidelberg, DE, 2014.

[35] Chen, Q.; Luo, M.; Hammershøj, P.; Zhou, D.; Han, Y.; Wegge Laursen, B.; Yan, C. G.; Han, B. H. Microporous Polycarbazole with High Specific Surface Area for Gas Storage and Separation. *J. Am. Chem. Soc*. **2012**, *134*, 6084-6087.

[36] Jing, X.; Zou, D.; Cui, P.; Ren, H.; Zhu. G. J. Facile Synthesis of Cost-Effective Porous Aromatic Materials With Enhanced Carbon Dioxide Uptake. J. Mater. Chem. A **2013**, 1, 13926 –13931

[37] Errahali, M.; Gatti, G.; Tei, L.; Canti, L.; Fraccarollo, A.; Cossi, M.; Marchese, L. Understanding Methane Adsorption in Porous Aromatic Frameworks: An FTIR, Raman, and Theoretical Combined Study. *J. Phys. Chem C,* **2014**, *118*, 10053-10060.

[38] Patent: "A porous organic polymer capable of adsorbing gas and the method of preparing thereof"; Applicant: SOL S.p.A., et al.; Inventors: Errahali M., Gatti G., Tei L., Cossi M., Marchese L. European application 13425105.7(**2013**); PCT International extension rif. E0094969 (**2014**).

[39] Eic, M.; Ruthven, D.M. A New Experimental Technique for Measurement of Intra-crystalline Diffusivity. *Zeolites* **1988**, 8, 40 - 45.

[40] Brandani, F.; Ruthven, D.M. Measurement of Adsorption Equilibria by the Zero Length Column (ZLC) Technique. Part 2:Binary Systems. Ind. *Eng. Chem. Res.* **2003**, 42, 1462-1469.

[41] Brandani, F.; Ruthven, D.M.; Coe, C.G. Measurement of Adsorption Equilibrium by the Zero Length Column (ZLC) Technique. Part 1: Single-Component Systems. *Ind. Eng. Chem. Res.* **2003**, 42, 1451-1461.

[42] Brandani, S.; Ruthven, D.M. Moments Analysis of the Zero Length Column Method.**1996**.

[43] Mangano, E.; Brandani, S.; Ferrari, M. C.; Ahn, H.; Friedrich, D.; Lozinsk, M. L.; Wright, P. A.; . Kahr, J.; Morris, R.; Croad, M.; McKeown, N.; Shamsipour, H.; Budd, P. Efficient and Rapid Screening of Novel Adsorbents for Carbon Capture in the UK IGSCC Project. *Energy Procedia* **2013**, 37, 40 – 47.

GENERAL CONCLUSIONS

In this PhD thesis, the synthesis and characterization of microporous polymeric materials and their gas (H_2, CH_4 and CO_2) uptake properties are reported, with particular attention given to the optimization of the textural properties (specific surface area and pore size distribution). Two classes of porous materials with different porosity were optimized to this purpose: i) porous aromatic frameworks (PAF) and ii) hyper-crosslinked polymers (HCP). The synthetic methods were optimized and the physico-chemical properties were studied using a multidisciplinary approach. The main objective of this study was the development of new materials suitable for gas storage. The hydrogen, methane and carbon dioxide uptakes at different conditions of temperature and pressure were evaluated.

The synthetic procedure reported in the literature for PAF-302 sample was modified in our laboratory. The material showed high stability and high porosity: a surface area of 4293 m^2/g and total pore volume of 2,38 cc/g were reached. The cost of this synthesis on a laboratory scale is estimated to be 341 €/g.

The optimization of the experimental conditions for the synthesis of PAF-302 was made not only to obtain reproducible materials with high surface area, but also with the aim to reduce the costs: the catalyst of the reaction is the very expensive and its formation directly in situ allowed the reduction of the cost of the synthesis to 125 €/g (13 €/g on a pilot scale). The sample called PAF-302 in situ is characterized by lower surface area (2200 m^2/g), however, if pores smaller than 10 Å are considered (the most relevant for the storage of CH_4, H_2 and CO_2), this material shows a micropore volume (0.36 cc/g) much higher than that (0.029 cc / g) measured for PAF-302 obtained with the traditional synthesis.

In order to improve CO_2 adsorption, PAF-302 was functionalized with amino groups using both wet synthesis starting from amine functionalized precursor (PAF-302-CH_2NH_2) and post-synthesis treatment in which amino groups were introduced using a plasma technique (PAF-302 plasma). These materials are characterized by lower surface area and lower pore volume in comparison to the parent PAF-302. However, PAF-302-CH_2NH_2 shows families of very small micropores of 8 Å and ultramicropores of 5 Å. Beside the very small pores, this sample is also characterized by micropore volume of 0.275 cc/g, which is ten times higher than that of PAF-302.

Hyper-Crosslinked Polymers (HCPs), a class of low cost porous organic networks easily prepared by Friedel–Crafts reaction, were also studied in this thesis. Several HCP polymers obtained from different aromatic tetrahedral monomers and crosslinked by means of formaldehyde dimetil acetal (FDA) were obtained for the first time in this thesis. If the tetraphenylmethane (TPM) is considered, the polymer synthesised with a

TPM:FDA ratio of 1:16 (mPAF-1/16) showed the highest surface area (1314 m^2/g) and pore volume (0,83 cc/g). mPAF-1/16 was also modified by post-synthesis treatments:

1) The thermal treatments enhanced both surface area and total micropore volume;
2) The amine functionalization caused a decrease in the porous properties, due to the inclusion of the new chemical groups, and an increase of the CO_2 storage capacity.

Using the optimized reaction conditions, several HCP polymers were formed starting from the tetrahedral aromatic precursors such as tetraphenylsilane, tetraphenyltin, tetraphenyladamantane, tetraphenylethane and tetraphenylethene. The resulting materials are characterized by high surface area and high micropore volume with predominance of pores size < 10 Å.

The work of synthesis and optimization of the materials was also supported by measures of gas storage on some selected materials. The adsorption capacities of CH_4, H_2 and CO_2 gases in PAF and HCP materials were measured at different temperatures and pressures to evaluate their performance in gas capture and storage. Some results were also compared with Grand Canonical Monte Carlo simulations performed within our research group.

- CH_4 adsorption at 298K and pressures up to 200 bar on PAF-302 demonstrated the importance of the high total pore volume with contribution of both pores of ca. 12 Å and small mesopores. On the other hand, for hydrogen uptake at 77K (up to 200 bar), the experimental and computational measurements confirmed that the microporosity is the most relevant property.
- mPAF-1/16, the HCP polymer with the highest surface area (1314 m^2/g) shows ultramicropores of about 5.82 Å (measured by Ar at 87K), a pore size peculiar to obtain high CO_2 uptake at low pressure, as observed for other materials reported in literature.

The comparison of the volumetric and gravimetric measurements of CH_4 at 298 K and 10 bar for mPAF-1/16 and PAF-302 confirms the importance of the materials density, especially for the industrial application: PAF-302, despite its high surface area and high pore volume, shows a volumetric storage capacity of 18,44 g/L, which is smaller than that measured for mPAF-16 (27,13 g/L). Indeed, the measured density of mPAF-1/16 (0.29 g/cc) is about twice that measured for PAF-302 (0.6 g/cc).

Another important advantage of HCP materials compared to PAFs regards the cost of the synthesis: on a laboratory scale PAF-302 costs 340 €/g while mPAF-1/16 costs 5 € /g, that may become 0,12 € /g on a pilot scale. Therefore, materials obtained with Friedel-Crafts synthesis are cheaper and more efficient for an industrial application. In fact, this method led to the deposition of an European patent in collaboration with OMB Saleri and SOL Group companies, and the material was called UPO-1 (UPO stands for Università del

Piemonte Orientale). A subsequent optimization concerning the concentration of precursor in the solvent and a post-synthesis heating treatment at 380 °C enabled us to write another patent which will be very early submitted in collaboration with SOL Group.

The CO_2 storage capacity for almost all materials synthesized in this thesis was evaluated using the zero length column (ZLC) method, at 0.1 bar and 35 ºC, which are the real conditions of a typical flue gas stream from post-combustion application. This technique, which requires a little amount of sample, allowed a rapid screening and a direct comparison of the synthesized materials. The measurements have confirmed the importance of the pores smaller than 7Å and the need of functionalization with heteroatoms to increase the CO_2 adsorption capacity of the porous materials.

Finally, synthetic procedures reported in this thesis can be exploited to prepare supports for the catalytic reduction of CO_2. In this context, within a PRIN project in collaboration with the University of Messina, we explored the feasibility of the electrocatalytic conversion of CO_2 to liquid fuels under gas-phase conditions, by using a conjugated microporous polymer as a component of the electrocatalyst. In particular, tetrakis-phenylethene conjugated microporous polymer (TPE-CMP) was synthesized using Yamamoto coupling and its surface was functionalized with Pt nanoparticles mixed to a small amount of CNTs to increase both the electronic conductivity and the quality of the ink before the impregnation on the C-based support. Results showed the better performances of the metal-doped TPE-CMP in terms of total productivity (C1-C8 oxygenates) with respect to other kinds of materials with limited CO_2 adsorption capacity.

Acknowledgements

Firstly I would like to sincerely thank my supervisor Prof. Leonardo Marchese, who patiently provided the vision, encouragement and advice necessary for me to proceed through this work.

I would like to thank my Co-supervisors, Dr. Lorenzo Tei and Dr. Giorgio Gatti, who have helped me with everything, from experimental problems to lab support and even took the time to revise my thesis, which was very much appreciated.

I would like to thank Prof. Maurizio Cossi, Dr. Alberto Fraccarollo and Dr. Lorenzo Canti for their helpful discussions and theoretical calculations.

I wish to thank Dr. Geo Paul for providing the SS-NMR spectra measurements and Dr. Gabriele Rolla who was always there to answer my synthetic questions.

Many thanks go to my friends, colleagues and staff in "Università del Piemonte Orientale", and particularly Vittoria, Sara, Chiara, Fabio, Daniele, Giusy and Fabiana for their friendship and always being willing to help.

Words cannot be express how grateful I am to my family for all their support, encouragement and prayers for me.

Lastly, a special thanks goes to companies SOL group S.p.A and OMB Saleri S.p.A for funding this research.

APPENDIX 1

Instrumental parameters

1. Fourier Transform Infrared Spectroscopy (FTIR)

The Infrared spectra of materials in KBr pellets were collected using a Bruker Equinox 55 spectrometer equipped with a pyroelectric detector (DTGS type) with a resolution of 4 cm^{-1}.

For the infrared adsorption measurements, gas CH_4 (Rivoira S.p.A., 99.995%) and CD_4 (Cambridge Isotope Laboratories, Inc. C.N. CDLM-1616-0 with deuterium pure grade 99.7%) were employed. In this experiment, Infrared spectra of materials in the form of self-supporting pellets were collected under vacuum conditions (residual pressure $<10^{-5}$ Torr; 1 Torr = 133.33 Pa) using a Bruker Equinox 55 spectrometer equipped with a pyroelectric detector (DTGS type) with a resolution of 2 cm^{-1}. Before CH4 and CD4 gas adsorption experiments, samples were outgassed at 473 K at a heating rate of 5 °C/min, for 12 h in the IR cell directly connected to the vacuum line. After the thermal treatment, the samples were then cooled down to 110 K for the collection of IR spectra at 100 mbar of CH_4 and progressively decreased gas pressures. The same experiment was performed using CD_4 gas.

2. Solid State Nuclear Magnetic Resonance (SSNMR)

All solid state NMR (SS-NMR) spectra were acquired on a Bruker Advance III 500 spectrometer and a wide bore 11.7 Tesla magnet with operational frequencies for ^{13}C of 125.77 MHz. A 4 mm triple resonance probe with MAS was employed in all the experiments. The samples were packed on a zirconia rotor and spun at a MAS rate of 15 kHz. For the $^{13}C\{^1H\}$ CPMAS experiments, the magnetic fields υ_{rf}^{H} of 55 and 28 kHz were used for initial excitation and decoupling, respectively. During the CP period the ^1H RF field υ_{rf}^{H} was ramped using 100 increments, whereas the ^{13}C RF field υ_{rf}^{C} was maintained at a constant level. During the acquisition, the protons are decoupled from the carbons by using a TPPM decoupling scheme. A moderate ramped RF field υ_{rf}^{H} of 62 kHz was used for spin locking, while the carbon RF field υ_{rf}^{C} was matched to obtain optimal signal and the CP contact time of 2 ms was used. The relaxation delay between accumulations was 1 s and all chemical shifts are reported using δ scale and are externally referenced to TMS at 0 ppm.

3. Elemental analysis (EA)

Elemental analysis were carried out with a EA3000 CHN Elemental Analyser (EuroVector, Milano, Italy). Acetanilide, purchased by EuroVector (Milano, Italy) was used as calibration standard (C % = 71.089, H % = 6.711, N % = 10.363).

4. X-Rays Diffraction (XRD) Analysis

X-ray diffractrograms (XRD) were collected on unoriented ground powders with a Thermo ARL 'XTRA-048' diffractometer with a Cu Ka (k = 1.54 Å) radiation. All samples were recorded at r.t. between 2° and 80° 2θ degrees with a step size of 0.02° and a rate of 1° 2θ/min.

5. Thermogravimetric Analysis (TGA)

The Thermogravimetric analyses were performed on a Setaram SETSYS Evolution instrument under argon (gas flow 20 mL/ min), heating the samples up to 1173 K with a rate of 5 or 2 K/min, depending on the analysed sample.

6. Scanning Electron Microscopy (SEM).

SEM images were recorded on a Quanta 200 FEI scanning electron microscope equipped with EDAX EDS attachment, using a tungsten filament as the electron source at 20 keV.

7. Physisorption Analyses

N_2 physisorption measurements were carried out at 77 K in the relative pressure range from 1 x 10^{-7} to 1 P/P_0 by using an Autosorb iQ/ASiQwin instrument (Quantachrome instrument). Prior to the analysis, the samples were outgassed between 150 and 250 °C for 18 h (residual pressure lower than 10^{-6} Torr) depending of the material analyzed. Specific surface areas were determined using the Brunauer–Emmett–Teller (BET) equation, in the relative pressure range from 0.05 to 0.15 P/P_0. Pore size distributions were obtained by applying the NLDFT (non-local density functional theory) method and using a silica model with cylindrical pore for HCP polymers and QSDFT method using a carbon model with combined slit and cylindrical pore for PAF materials. The true (skeletal) density of the samples was measured by Helium pycnometry at room temperature: the apparent density was computed by combining the true density and the porous volume provided by NLDFT.

Ar physisorption measurement at 87K of selected samples was performed in the relative pressure range from 1 x 10^{-7} to 1 P/P_0 by using an Autosorb iQ/ASiQwin instrument (Quantachrome instrument). Prior to the analysis, the samples were outgassed at 150/250 °C for 18 h (residual pressure lower than 10^{-6} Torr) depending of the material analyzed. Specific surface areas were determined using the Brunauer–Emmett–Teller (BET) equation, in the relative pressure range from 0.05 to 0.15 P/P_0. Pore size distributions were obtained by applying the NLDFT (non-local density functional theory) method and using a silica model with cylindrical pore.

8. Gas adsorption–desorption isotherms measurements

Methane, carbon dioxide and nitrogen adsorption–desorption measurements, carried out between 0 and 10 bar at 273K and 298 K and up to 1 bar at 195K, were measured on a Micromeritics instrument ASAP 2050. In order to evaluate the selectivity of CO_2/N_2, a binary mixtures of 15:85 was used from the single-component isotherms with the ideal adsorbed solution theory (IAST), which has been successfully used to calculate gas mixture separation by porous materials.

For high pressure (up to 200 bar) CH_4 and H_2 adsorption a fully automated volumetric Quantachrome device (iSorbHP1-BTRHYDM200) were used. In both experiments, about 400 mg of sample was used and degassed "in situ" at 250ºC under vacuum overnight. As results, excess adsorption isotherms at room temperature for methane and at 77K for hydrogen were obtained. Ultra-high-purity grade (99.99%) N_2, CH_4, H_2 and CO_2 gases were used for all adsorption measurements.

9. ZLC CO_2 measurments

For all samples the reversible capacity for CO_2 adsorption at 0.1 bar CO_2 and at 308 K was estimated by the ZLC method. Figure 1 shows a simplified schematic diagram of the experimental system. The ZLC cell consists of a small sample of adsorbent (1-5 mg) sandwiched between two sintered disks and contained within a 1/8-in. Swagelok fitting. The switch valve is a standard high temperature Valco valve, operable up to 532-573 K. A small electric heater with its own temperature control surrounds the ZLC cell, thus allowing the adsorbent to be regenerated in situ at temperatures up to 723 K without exposing the valve to these temperatures. The detector is an on-line quadrupole mass spectrometer (Ametek model MA200HDEF with a Balzers turbomolecular pump). The gas leaving the cell is sampled continuously through a silica capillary connected to the chamber of the mass spectrometer. The effluent concentration response curves are recorded in digital form for data processing. The flow rates of both the feed and purge streams are controlled by mass flow controllers.

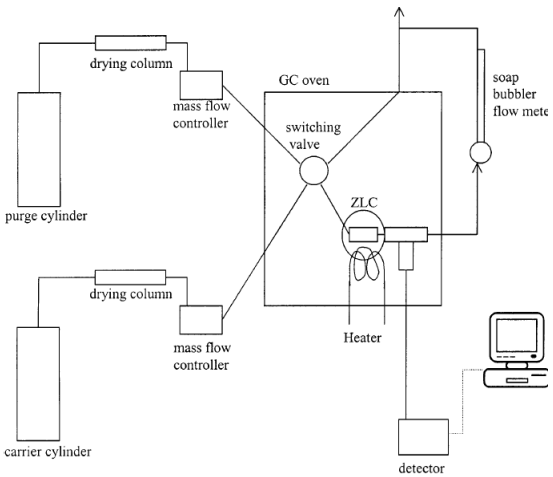

Figure 1. Zero length column (ZLC) experimental setup

The technique is based in following the desorption curve of a sample previously saturated with a mixture of 10% CO_2 (sorbate) in He (carrier). When equilibrium between the gas phase and the adsorbed phase is reached, the flow is switched to pure He (purge) and the outlet gas phase concentration from the column is monitored by the quadrupole mass spectrometer detector. The apparatus is provided with drying columns to ensure predried gases entering the system; high and low flow rate mass flow controllers (0 − 50 mL/min and 0 −3 mL/min, respectively) allowed experiments to be conducted under kinetic and equilibrium control.

Before each experiment the samples were dehydrated overnight under flow of pure He at 423 K and 523 K for mPAF and PAFs samples, respectively.

The calculations of the CO_2 capacities are based on the dry weight of the sample. To ensure that full saturation was reached, preliminary ZLC experiments were run increasing the exposure time to the sorbate: the sample was fully equilibrated when the CO_2 capacity obtained did not change with the exposure time. Depending on the sample, the time for saturation was ranging between 10 and 80 min.

10. Theoretical methods:

PAF-302 model: PAF-302 model was built starting from the diamond structure and optimized using COMPASS force field: the standard CIF file was modified by lowering the point symmetry to P1 and increasing the cubic cell edge. Then, the optimized polyphenyl fragments (without the methyl groups) were inserted between each couple of neighboring C −C, and the fragments were rigidly rotated to eliminate all the close contacts between hydrogen atoms. The structural properties of the PAF-302 model are listed in Table 1: the skeletal volume and the effective surface area were estimated by the GEPOL procedure implemented in G03, which is used in another context to define the solute −solvent boundary in polarizable continuum models.

Table 1. Structural and textural properties of crystalline PAF-302 model

	unit cell length, L (Å)	unit cell formula	unit cell molecular weigth (g mol^{-1})	density (g cm^{-3})	specific volume, V_{sp} (cm^3 g^{-1})	unit cell skeletal volume, V_{sk} (Å^3)	porous volume fraction[(a)]	specific porous volume (cm^3 g^{-1})[(b)]	specific surface area (m^2 g^{-1})
PAF-302	23.440	$C_{200}H_{128}$	2528	0.326	3.07	2483	0.81	2.48	5519

[a] $f_{pore} = (L^3 - V_{sk})/L^3$. [b] $V_{sp,pore} = f_{pore} \times V_{sp}$

mPAF-1/16 model. The mPAF model consists in a periodic molecular model defined as a network of tetraphenylmethane moieties connected by methylene bridges in para position. The model was actually built by starting from the polyaromatic network with a diamond structure where each C-C bond has been substituted by two aromatic rings with H in every second sp3 carbon. The resulting structure was optimized at the Density Functional Theory (DFT) level with the plane-wave code PWSCF, using the Perdew-Burke-

Ernzerhof (PBE) functional and 120 Ry energy cutoff: the periodic lattice is triclinic with P1 symmetry (i.e. no point group symmetry is imposed, to leave the largest flexibility to the atoms inside the unit cell).

Ar, CH_4, H_2 and CO_2 calculated isotherms. The adsorption isotherms of Ar, CH_4, H_2 and CO_2 were simulated using the sorption module included in Materials Studio package, in a series of Monte Carlo (GCMC) techniques. The simulations were performed with a purposely adapted force field; for the adsorption of methane and carbon dioxide were used previously optimized force fields, CVFF and DREIDING, respectively: these force fields were obtained for PAF networks, but they can be used safely for mPAF too, since the kind of atoms and the expected interactions are the same in the two classes of materials.

For hydrogen the simulations were performed with DREIDING force field, which was optimized to fit the correct behavior of the free gas in all the pressure range and to reproduce the hydrogen −phenyl interactions computed at high quantum mechanical level (post Hartree −Fock).

For Ar an adapted version of PCFF force field was used: Argon parameters were slightly modified to reproduce the free gas density at 87 K in the 0-1 bar pressure range. On the other hand, the standard PCFF parameters for carbon and hydrogen were employed, since we verified that they provide a good agreement with high level quantum mechanical calculations, at MP2 level with 6-311+G(2d,2p) basis set, for different energy scans of Ar-benzene and Ar-diphenylmethane complexes. Detailed information on the material models and methods used can be found in refs. 1-3.

References:

[1] Cossi, M.; Gatti, G.; Canti, L.; Tei, L.; Errahali, M.; Marchese, L. Theoretical Prediction of High Pressure Methane Adsorption in Porous Aromatic Frameworks (PAFs). *Langmuir* **2012**, 28, 14405-14414.

[2] Fraccarollo, A.; Canti, L.; Marchese, L. and Cossi, M. Monte Carlo Modeling of Carbon Dioxide Adsorption in Porous Aromatic Frameworks. *Langmuir* **2014**, 30, 4147−4156

[3] Errahali, M.; Gatti, G.; Tei, L.; Paul, G.; Rolla, G. A.; Canti, L.; Fraccarollo, A.; Cossi, M.; Comotti, A.; Sozzani, P.; Marchese, L. Microporous Hyper-Cross-Linked Aromatic Polymers Designed for Methane and Carbon Dioxide Adsorption. *J. Phys. Chem. C* **2014**, 118, 28699–28710.

APPENDIX 2

Papers and patents

Paper I:

Theoretical prediction of high pressure methane adsorption in porous aromatic frameworks (PAFs) - M. Cossi, G. Gatti, L. Canti, L. Tei, **M. Errahali** and L. Marchese, (**2012**) Langmuir 28(40),14405-14.

Paper II:

Understanding Methane Adsorption in Porous Aromatic Frameworks (PAF): A FTIR, Raman and Theoretical Combined Study. **M. Errahali**, G. Gatti, L. Tei, L. Canti, A. Fraccarollo, M. Cossi, L. Marchese; J. Phys. Chem. C, **2014**, 118(19), pp 10053–10060.

Paper III:

An electrochemical reactor for the CO_2 reduction in gas phase by using conductive polymer based electrocatalysts. C. Ampelli, C. Genovese, S. Perathoner, G. Centi, **M. Errahali**, G. Gatti, L. Marchese Chemical Engineering Transactions, Vol. 41 (**2014**), pp. 13-18

Paper IV:

Microporous Hyper-crosslinked Aromatic Polymers Designed for Methane and Carbon Dioxide Adsorption **Errahali, M**; Gatti, G; Tei, L; Paul, G; Rolla, G; Canti, L; Fraccarollo, A; Cossi, M; Comotti, A; Sozzani, P; Marchese, L. J. Phys. Chem. C **2014**, 118, 28699–28710.

Paper V:

CO_2 capture and reduction to liquid fuels in a novel electrochemical setup by using metal-doped conjugated microporous polymers. C. Ampelli, C. Genovese, **M. Errahali**, G. Gatti, L. Marchese, S. Perathoner, G. Centi, Journal of Applied Electrochemistry, **2015**. Submitted.

Patent I:

Patent: “A porous organic polymer capable of adsorbing gas and the method of preparing thereof”; Applicant: SOL S.p.A., et al.; Inventors: **Errahali M.**, Gatti G., Tei L., Cossi M., Marchese L. European application 13425105.7(**2013**); PCT International extension rif. E0094969 (**2014**).

Patent II Under submition:

Patent: “A porous aromatic hypercrosslinked polymer capable of adsorbing gas and the method of preparing thereof”; Applicant: SOL S.p.A.; Inventors: **Errahali M.**, Gatti G., Tei L., Cossi M., Marchese L.(**2015**).